2006

Statistical estimation of strain energy release rate of delaminated composites

Rajesh Vijayaraghavan
West Virginia University

Statistical Estimation of Strain Energy Release Rate of Delaminated Composites

Rajesh Vijayaraghavan

Thesis submitted to the
College of Engineering and Mineral Resources
at West Virginia University
in partial fulfillment of the requirements
for the degree of

Master of Science
in
Mechanical Engineering

Nithi T. Sivaneri, Ph.D., Chair
Bruce S. Kang, Ph.D.
Kenneth H. Means, Ph.D.

Department of Mechanical and Aerospace Engineering

Morgantown, West Virginia
2006

Keywords: Composite Materials, Delamination, Strain Energy Release Rate, Monte Carlo Simulation, Regression Analysis, Response Surface Method

ABSTRACT

Statistical Estimation of Strain Energy Release Rate of Delaminated Composites

Rajesh Vijayaraghavan

An improved two-sublaminate model based on first-order shear deformation theory is implemented in a general-purpose finite element software (ANSYS) to study delaminated composite plates. Double cantilever beam and end-notched flexure models of unidirectional and multidirectional composite plates with mid-plane and offset delaminations are analyzed. The total strain energy release rate and the mode-I, mode-II and mode-III components are evaluated using a plate-theory-based crack-closure technique.

The effects of variation of material properties, ply thickness, fiber orientation, coefficient of friction between the crack surfaces, finite element mesh density and virtual crack-closure length and applied load on the mixed-mode strain energy release rates are studied using Monte Carlo simulations. The statistics and trends are analyzed and quantified using sensitivity plots and scatter plots. Anderson-Darling goodness-of-fit tests are performed on the results to fit them to a two-parameter Weibull, normal or log-normal distribution and the statistically-based design values are calculated. Three-dimensional contour plots are also generated to study the overall variation in the strain energy release rate distribution along the delamination front.

In the case of double cantilever beam specimens, the ply thickness has a significant influence on the total and average strain energy release rate. Fiber misalignment controls the amount of mode-II and mode-III components observed. The maximum and minimum values are also highly dependent on the virtual crack-closure length. For unidirectional end-notched flexure models, sliding friction effects are found to be negligible and occur only adjacent to the supports. For the symmetric and unsymmetric end-notched flexure models studied, the energy loss due to sliding friction controls the total strain energy release rate for friction coefficients greater than 0.16 and 0.24, respectively.

ACKNOWLEDGEMENTS

I am greatly indebted to my research advisor Dr. Nithi T. Sivaneri, for accepting to guide me without any second thoughts, for giving me the freedom to experiment and for readily helping me out in all my times of need. I would like to thank Dr. Bruce Kang for his suggestions and also for his recommendation letters towards my Ph.D. aspirations. I appreciate Dr. Kenneth Means' suggestions, without which I wouldn't have looked up at the datasheets of composite panels to obtain industrial design values for my research work.

I have made it a practice; not to thank my friends. So, it would only be fit to dedicate my thesis to these people, for all the unthanked help and support: AO, Aravinth Anna, Ashok, Biles, Doctor, Gap, Kammi, Karthi, and Susai.

Last but not the least; I owe it all to my friends Gnanam, Kevin, Naresh, Sadha and Saji and my family in India for standing by me and encouraging me during all my endeavors.

TABLE OF CONTENTS

LIST OF SYMBOLS

a	- Delamination length (m)
$[a(z)]$, $[b(z)]$	- Partial membrane and bending-extension coupling stiffness
$[A]$	- In-plane stiffness matrix (N/m)
AD	- Anderson-Darling test statistic
B	- B-basis value of a distribution
$[B]$	- Bending-extension coupling matrix (N)
$CNFX$	- X-component of contact element force (N)
$CNFY$	- Y-component of contact element force (N)
$CNFZ$	- Z-component of contact element force (N)
$[D]$	- Bending stiffness matrix (Nm)
E_1	- Longitudinal modulus (N/m^2)
E_2	- Transverse modulus (N/m^2)
G, G_I, G_{II}, G_{III}	- Total strain energy release rate and mode-I, mode-II and mode-III components (J/m^2)
G_{12}	- In-plane shear modulus (N/m^2)
G_{13}, G_{23}	- Transverse shear moduli (N/m^2)
$[H]$	- Interlaminar stiffness matrices (N/m)
$[\overline{H}]$	- Improved transverse shear stiffness (N/m^2)
$\{M\}$	- Moment resultants (N)
N_{xc}, N_{xyc}, Q_{xc}	- Concentrated crack-tip forces (N/m)
$\{N\}$	- Force resultants (N/m)
OSL	- Observed Significance level
$pene$	- Penetration of each contact element (m)
$\{Q\}$	- Transverse shear forces (N/m)
$\left[\overline{Q}^*\right]$	- Transformed interlaminar stiffness matrix (N/m^2)
$[\overline{Q}]^{(k)}$	- Reduced stiffness matrix of the kth lamina (N/m^2)
t, t_1, t_2	- Thickness of laminate, upper and lower sublaminates (m)

$t^{(k)}$ - Thickness of the k^{th} lamina (m)

$tasx$ - Total accumulated sliding in the X-direction (m)

$tasy$ - Total accumulated sliding in the Y-direction (m)

u, v, w - Displacements along the x, y, and z-directions (m)

u_0, v_0, w_0 - Displacements of every point (x, y) of the middle surface of the plate (m)

U_0 - Complementary transverse shear energy (N/m^2)

W^f - Energy lost to friction (Nm)

W^p - Work done by contact elements in normal direction (Nm)

$\begin{bmatrix} \alpha & \beta \\ \beta & \delta \end{bmatrix}$, $[h]$ - Compliance matrices

$\hat{\beta}$, $\hat{\alpha}$ - Shape and scale parameter estimates of Weibull distribution

γ_{yz}, γ_{yz} - Transverse shear strains

δa - Virtual crack closure length (m)

$\delta_Q, \delta_{11}, \delta_{16}, \delta_{66}$ - Compliance coefficients (N^{-1} m^2)

ΔA - Change in crack area (m^2)

$\{\Delta N\}, \{\Delta M\}, \{\Delta Q\}$ - Change in force and moment resultants required for crack closure

ΔU - Change in elastic strain energy (Nm)

$\{\Delta\varepsilon^0\}, \{\Delta\kappa\}, \{\Delta\gamma\}$ - Change in mid-plane strains and curvatures required for crack closure

$\Delta\pi$ - Change in total potential energy (Nm)

$\varepsilon_x, \varepsilon_y, \gamma_{xy}$ - In-plane strains at any point in the plate

$\varepsilon_x^0, \varepsilon_y^0, \gamma_{xy}^0$ - Mid-plane strains

$\kappa_x, \kappa_y, \kappa_{xy}$ - Curvatures (m^{-1})

ν_{12}, ν_{21} - Poisson's ratios

$\{\tau\}$ - Transverse shear stresses (N/m^2)

ϕ_x, ϕ_y - Rotations of the normal to the middle surface at each point (x, y)

Variables and parameters used in ANSYS finite element software:

COD	- Crack-tip opening displacement
DELPE	- Change in potential energy
DELU	- Change in elastic strain energy
E11	- Longitudinal modulus
E22	- Transverse modulus
ERATIO	- Ratio of change in elastic strain energy to friction energy
FC	- Friction Coefficient
G	- Total SERR in the presence of friction
G12	- In-plane shear modulus
G13	- Transverse shear modulus
G23	- Transverse shear modulus
GAVG/GIAVG/ GIIAVG/GIIIAVG	- Average of the total, mode-I, mode-II and mode-III components across the delamination front
GMAX/GMIN/GMID	- Maximum, minimum and mid-point values
GSUM/GISUM/ GIISUM/GIIISUM	- Sum of the total, mode-I, mode-II and mode-III components across the delamination front
MRV	- Mesh refinement value
THETA	- Change in fiber orientation
TPLY	- Ply thickness
VCCL	- Virtual crack closure length
WFSUM	- Total energy lost due to friction

LIST OF TABLES

LIST OF FIGURES

1 INTRODUCTION

1.1 Problem Statement

The use of composite structures has seen a rapid growth in various industries due to their low weight-to-strength ratio and the scope for concurrent design. But the main drawback is that they have a comparatively low strength in the thickness direction and thus exhibit numerous failure modes, one of the most common being delamination between plies.

Numerous studies have been done to analyze delamination growth in laminated composites. The usual method is to evaluate the total strain energy release rate (SERR) G and it's mode-I, mode-II, and mode-III components G_I, G_{II} and G_{III} at various locations along the delamination front. "Failure is expected when, for a given mixed-mode ratio G_{II}/G, the calculated total SERR, G, exceeds the interlaminar fracture toughness, G_c", Krueger (2004). Some of the methods proposed in the literature for calculating the mixed-mode strain energy release rates are the Virtual Crack Closure Technique, J-Integral method, Crack-Tip Element method (CTE) and plate-theory-based crack-closure techniques. In most cases the crack surfaces are assumed to be smooth and only a few authors have considered sliding friction between the surfaces bound by the delamination and calculated the strain energy release rates which include the friction effects.

Even after incorporating sufficient refinements to the evaluation of the mixed-mode strain energy release rates, the common drawback in most of the works available in literature is that they are based on deterministic models, i.e. they do not account for the randomness or scatter in the data of the design parameters. The Composite Materials Handbook (2002), points out that "Variability in composite material property data may result from a number of sources including run-to-run variability in fabrication, batch-to-batch variability of raw materials, testing variability and variability intrinsic to the material". Similarly variability in dimension and fiber orientation is manifested from the type of process used for laying-up the laminate. Variability in testing environment is due to changes in temperature and moisture content. Testing methods, personnel performing the tests and applied loads are some of the other aspects in composites design that exhibit

uncertainties.

As far as finite element implementation of delamination problems is concerned, the mesh density, geometric uncertainties, material properties, loads, friction coefficient if sliding friction between crack surfaces is considered, delamination length, and virtual crack closure length are some of the random variables that can be controlled. The aim of the present study is to account for all these uncertainties by using appropriate probabilistic distributions for the design variables and calculate the statistically-based energy release rates along the delamination front. The results would assist in assessing the reliability of the structure when compared with statistical fracture toughness values. Also, the scatter in the strain energy release rate values obtained through a probabilistic analysis would aid in the non-conservative use of the resistance factor which determines the design values of the composite structure.

1.2 Literature Review

In this section, some of the techniques used for evaluating mixed-mode strain energy release rates from finite element models of delaminated composites are reviewed. Out of the techniques listed in section 1.1, the *J*-integral method is not considered. This is because, sliding friction effects are taken into account in this study and the *J*-integral loses its path independence in the presence of contact and friction. Emphasis is placed on the other three methods. The section is organized as follows:

- First, one of the most common data reduction methods, the virtual crack closure technique is reviewed.
- Next, plate theory-based crack closure techniques are studied. Among these, the two-sublaminate models are reviewed first followed by the multi-layer models.
- Two references, in which sliding friction effects between the delaminated surfaces are accounted for, are reviewed.
- Finally, references in which laminated composites are studied by taking into account the effects of various uncertainties are reviewed.

1.2.1 Virtual Crack Closure Technique

Virtual crack closure technique (VCCT) is based on Irwin's crack closure integral which assumes that the energy released when a crack is extended by a small distance Δa is equal to the energy required to close the crack by Δa. Further it is assumed that the crack extension does not alter the stress state at the crack tip. Krueger (2004) has given a detailed account on the history and approach used for the finite element implementation of the VCCT with emphasis on the application of the technique for damage analysis in composite structures. The VCCT formulae for use with two-dimensional quadrilateral elements and three dimensional solid and plate/shell finite elements with linear and quadratic shape functions are summarized. The various approaches required for geometrically nonlinear analyses, presence of arbitrarily shaped delamination contours, delaminations with sharp corners, elements with different lengths/widths at the crack tip and delaminations at bi-material interfaces are suggested.

Krueger (1994) has developed a classical laminate plate theory based three dimensional shell element and has used VCCT to determine the mixed mode strain energy release rate distributions along straight and curved crack fronts in double cantilever beam, end-notched flexure and single leg bending test specimens. The effects of mesh type and local refinement of mesh near the crack tip, which in-turn affects the virtual crack closure length, on the energy release rates and individual mode contributions are discussed.

Kruger, Rinderknecht and Konig (1997) have simulated delamination front growth in end-notched flexure specimens using adaptive meshing technique and compared them with experimentally observed results. They have also used surface-to-surface contact elements in conjunction with the penalty method to prevent interpenetration of the sublaminates in the cracked region.

Krueger and O'Brien (2001) have used a Shell/3D modeling technique to analyze delaminated composites. The global section is modeled using 4-node shell elements and the local section in the immediate vicinity of the delamination front extending to three specimen thicknesses on either side is modeled using 8-node solid elements. Multi-point constraint is used to enforce displacement compatibility along the shell-solid interface.

The total strain energy release rates and the individual components along the delamination front are found using the virtual crack closure technique for double cantilever beam, end-notched flexure and single leg bending test models.

1.2.2 Plate Theory-based Energy Release Rate Evaluation

Whitcomb, J.D. and Shivakumar, K.N. (1989) have developed a classical laminate plate theory based crack closure technique to calculate the distribution of total strain energy release rate around the boundary of the delamination in composite plates. The uncracked region is modeled as a single plate and the cracked region is modeled as two plates. The strain energy release rate is calculated as the work required for changing the mid-plane strains and curvatures at the crack front in the cracked region to be equal to those in the uncracked region. A transversely loaded square laminate and a post-buckled laminate with an embedded delamination surface under compressive loading are analyzed. Since classical laminate plate theory is used, the transverse shear deformations are neglected and also expressions for the components of strain energy release rate are not provided.

Sankar and Sonik (1995) have calculated the point-wise energy release rate along the delamination front in terms of force and moment resultant jumps across the front. They also provided a measure of error in the *J*-integral or *G* values computed using plate theories by comparing the *J*-integrals obtained using exact stress fields and the plate theory stresses.

Bruno and Greco (2001) have analyzed symmetric laminates with mid-plane delaminations using their interface model and found that the bending-shear interaction has a notable influence on the mode-I component of the energy release rate. Wang and Qiao (2004a) have extended the formulation to general two-dimensional cases by including the bending-shear interaction and have calculated the total energy release rate using the *J*-integral method. The expression for strain energy release rate contains terms that not only account for shear deformation in the cracked region but also terms that account for the in-plane force-shear and bending moment-shear interactions in the uncracked region. The stress intensity factors are evaluated by extending the formulation

of Suo and Hutchinson (1990) to include transverse shear forces. They have also provided expressions for the complex stress intensity factors using only two concentrated forces N_c and Q_c and a mode mix parameter, ω_1 which is identical to that defined by Davidson, Hu and Schapery (1995).

1.2.2.1 Crack-tip Element Method

Schapery and Davidson (1990) have used a global approach to predict the distribution of the total strain energy release rate using force and moment resultants applied to a plate model. It should be noted that the total strain energy release rate is not affected by the local stress fields around the tip but the individual energy release rates are influenced by it. So they have proposed a local approach, called the crack-tip element approach, where a separate continuum analysis is performed on a small portion of the specimen around the delamination front using a solid finite element model and a refined mesh to retrieve the mode components of the strain energy release rate.

Suo and Hutchinson (1990) have analyzed a semi-infinite interface crack between two infinite isotropic elastic layers using the superposition principle wherein the strain energy release rate is expressed in terms of only two independent loads P and M. They are the equivalent force and moment per unit thickness respectively which control the crack-tip singularity. The mixed-mode stress intensity factor is also solved analytically except for a single real scalar parameter ω which is similar to the mode-mix parameter of Schapery and Davidson (1990), Ω. The evaluation of this parameter ω, which is a function of the specimen geometry and material properties, requires a supplementary analysis for one particular loading combination and the value extracted through Gauss-Legendre integration.

Davidson and Krafchak (1993) have used the crack-tip element approach to predict mixed-mode energy release rates in one-dimensional delamination buckling problems. They have performed a closed-form, nonlinear cylindrical buckling analysis on a laminate with two symmetrically located delaminations near the free-surface. The forces and moment resultants thus obtained are input into a linear crack-tip element analysis to obtain the total energy release rate and the individual mode-I and mode-II

components. This method also requires one more linear finite element analysis of the crack-tip element geometry to determine the mode-mix parameter Ω.

Davidson (1995) has employed the crack-tip element approach to laminates containing free-edge delaminations. The total energy release rate and individual modes are defined by a concentrated crack-tip force and moment N_c and M_c and a mode-mix parameter Ω. The problems associated with oscillatory singularity in the near-crack stress field are eliminated by neglecting the effects of the bi-material constant ε by setting β, a generalization of one of Dundur's parameters for isotropic materials, to zero.

Davidson, Hu and Schapery (1995) have extended the crack-tip element approach to cover the case of non-zero biomaterial constant ε, which produces oscillatory singularity. Specific values for the mode-mix parameter Ω are also presented for a large number of cases.

Davidson (1998, 2001) has observed that mode decomposition of the energy release rate based on the singular-field based approach is valid only if the near-tip damage zone is smaller compared to the singular zone or the zone of K-dominance, which is of the order of a single-ply thickness in multidirectional composites and where the stress and strain fields correspond to the classical linear elastic fracture mechanics predictions. If a zone of K-dominance does not exist then different geometries predicted to be at the same mode mix would display different toughness. For such materials Davidson has proposed a non-singular field based approach which is insensitive to the details of the near-tip damage state. An explicit expression for the non-singular field based mode mix parameter is provided which is valid for all materials and lay-ups and depends only on the thicknesses of the two sublaminates above and below the delamination plane.

1.2.2.2 Multi-layer Models

Zou, Reid, Soden, and Li (2001) have modeled each ply or group of plies above and below the delamination plane as sublaminates based on first-order shear deformation theory. The rotations between the sublaminates are independent of each other. Displacement compatibility is enforced using constraint equations. They found that there

are no interfacial moments and only three concentrated forces exist, which represent the stress resultant jumps across the delamination front. These forces correspond to the three modes of fracture and the mode components are calculated by VCCT.

The above formulation suffers from a strong dependence on the mesh refinement around the delamination front for the stress resultant jumps to converge to the exact concentrated forces required for VCCT. Zou, Reid, Li and Soden (2002) have developed an alternative approach which eliminates the above drawback. The individual energy release rates are calculated in terms of the stress resultant jumps and the derivatives of the relative displacements between the upper and lower surfaces of the delamination at its tip.

Bruno, Greco, and Lonetti (2003) have proposed a multilayer model based on first-order shear deformation theory to analyze two dimensional delaminated structures. The laminate is divided in the thickness direction into a number of sublaminates. Interface displacement compatibility between the layers is enforced with interface elements that use the Lagrange multiplier method whereas in the previous case constraint equations are used. The uncracked region is simulated using interface elements in conjunction with the penalty method by treating interface stiffness as penalty parameters. The mode-I and mode-II strain energy release rates are computed using the penalty parameters and the relative displacements between the upper and lower sublaminates at the crack tip. Bruno, Greco, and Lonetti (2005) have extended the model to cover three dimensional delamination problems.

1.2.3 Sliding Friction between Delaminated Surfaces

Buchholz, Rikards, and Wang (1997) have analyzed delamination growth initiated from a transverse crack in a cross-ply laminate under three point bending. Contact and friction along the crack surfaces are taken into account in their two dimensional finite element model. The influence of the coefficient of friction on the energy release rates is studied and is found to be significant for short delaminations and insignificant for long cracks.

Sun and Qian (1998) have proposed a fracture criterion based on finite extension strain energy release rate which can be used as a measure of fracture toughness when

frictional sliding between crack faces is included. They have performed numerical simulations of a center crack in a plane strain infinite bi-material panel under remote shear loading and also fiber pull-out and push-out tests.

1.2.4 Improved Transverse Shear Stiffness

Rolfes and Rohwer (1997) have proposed a method to calculate accurate transverse shear stresses in laminated composite plates. The usage of shear correction factors is eliminated since the formulation itself provides an improved transverse shear stiffness matrix. The transverse shear stresses are calculated directly from the transverse shear forces by neglecting the influence of membrane forces on the transverse shear stresses and by assuming two cylindrical bending displacement modes. This method provides better results than those based on shear correction factors and the equilibrium method usually implemented in commercially available finite element software. Since it is based on first-order shear deformation theory and only first derivatives of the shape functions are necessary, it is easy to implement at the post-processor level. Rolfes, Noor, and Rohwer (2000) have later improved the formulation to account for thermal loadings and have also provided expressions for transverse normal stresses, which require only second derivatives of the shape functions.

1.2.5 Probabilistic Design

The Composite Materials Handbook (2002) has laid out detailed guidelines on the statistical characterization of polymer matrix composite structures for use in the aerospace industry. It examines the various methods used for finding the *A*-basis and *B*-basis values from composite material data, which are 95% lower confidence bound on the first and tenth percentile values of the population, respectively. It suggests the *k*-sample Anderson-Darling test for determining whether the data available is structured or unstructured. For unstructured data, a 5% significance level is used for testing the goodness-of-fit for Weibull, normal and log-normal distributions in that particular order and the next distribution is examined only if the previous one is rejected. If none of them

fit adequately, a nonparametric basis value is calculated depending on the sample size. For structured data, where grouping is based only on one random effect, say, batch-to-batch variability of data, the handbook suggests the use of a test for equality of variances and the application of the ANOVA procedure for finding the basis values.

Chamis, Singhal and Minnetyan (1994) have studied the initiation and propagation of damage for a polymer matrix composite panel fastened near one end by a bolted joint and under uniform edge load at the other end. They describe a method wherein the uncertainties are progressively defined at each scale of the composite structure viz. fiber-matrix constituents, ply, laminate, structure and fabrication process. The fiber longitudinal and transverse moduli, fiber and matrix coefficients of thermal expansion, matrix modulus, fiber volume fraction, ply thickness and the end load are considered as uncertainties. The sensitivities of the end displacement, ply longitudinal, transverse and shear stresses to the above mentioned uncertainties are assessed.

Dirikolu, Aktas and Birgoren (2002) have used the two-parameter Weibull distribution to statistically analyze the fracture strength values obtained from a series of tension tests performed on unidirectional carbon/epoxy composite panels. The scale and shape parameters of the Weibull distribution are obtained using the method of linear regression and the fracture strength is defined in terms of a reliability function.

Zureick, Bennett and Ellingwood (2006) have analyzed strength and stiffness properties of FRP composite materials in view of establishing a method, consistent with those used with other common materials, to statistically characterize the data. The Anderson-Darling test is used to evaluate the goodness-of-fit for normal, log-normal and Weibull distributions. They suggest that strength data be represented using the two-parameter Weibull distribution and nominal design value be calculated as the lower tolerance limit associated with 80% confidence level for the fifth percentile value of the Weibull distribution.

1.3 Need for Present Research

As composite materials are replacing conventional materials in various fields, it is imperative that a good insight on the characterization of one of its most frequent failure

modes, which is delamination between plies, be obtained. Traditionally two dimensional and three dimensional finite elements have been used in conjunction with the virtual crack closure technique to obtain the mixed-mode energy release rates along the crack front to predict the onset of delamination growth. But this method poses problems in dealing with oscillatory stress singularity at the vicinity of the crack tip and the dependence of the VCCT forces on the mesh refinement for convergence. The use of plate theory force and moment resultants to evaluate strain energy release rates eliminate the problems associated with stress singularity and meshing requirements, to an extent.

It has been shown that interlaminar stresses contribute significantly to the mode-I energy release rate. So use of first-order shear deformation theory or higher-order plate theory is required to adequately capture the stress state at the crack-tip. Since only FSDT-based plate/shell elements are commonly available in commercial finite element software, its use in the present work is justified. But FSDT uses a shear correction factor for interlaminar stresses, which is only an approximation. Few authors have proposed multi-layer models which improve the accuracy of the model by a small degree, but the number of elements increases linearly with increase in the number of sublaminates used and thus increase computational time and cost. The best alternative would be to use a two sub-laminate FSDT model instead of a multi-layer model and implement a suitable procedure in the pre-/post-processing phase to improve interlaminar stress evaluation.

But even after sufficient improvements and refinements to the testing and finite element implementation of delaminated composites, it suffers a setback in the form of variability of the design variables. So it is important to account for the uncertainties in the design of composite structures, which are encountered at every stage of fabrication, from the micromechanical scale to ply, laminate, structure and fabrication process. Extensive research is being conducted to standardize the procedure for obtaining statistically-based composite material property data. For example, the two-parameter Weibull distribution is suggested for fitting fracture toughness values of laminated plates. To predict the onset of delamination growth, the strain energy release rates are compared with the fracture toughness values, at a particular mixed-mode ratio. To aid in this comparison, it is required that statistically-based energy release rate values be evaluated. In this thesis an attempt is made to account for the various random design variables encountered in the

finite element implementation of delaminated composites by performing Monte Carlo simulations, evaluating the components of the strain energy release rates and fitting them to appropriate distributions.

1.4 Objectives

The objectives of this thesis are:

- To parametrically develop deterministic models of laminated composite plates with through-the-width delaminations using the two-sublaminate model and shell elements based on first-order shear deformation theory.
- To generate a MATLAB code, to calculate improved transverse shear stiffness values and the matrices used for evaluating improved transverse shear forces and strains, for a given laminate configuration and the corresponding material properties, and import the data into ANSYS at the pre-processor phase.
- To enforce displacement compatibility between nodes in the uncracked region using the internal multi-point constraint (MPC) algorithm of contact elements.
- To prevent layer interpenetration between the sub-laminate arms and to account for sliding friction along the delamination surfaces by using surface-to-surface contact elements that are based on the augmented Lagrange method.
- To implement an FSDT based improved plate closure technique in the post-processing phase for the calculation of total energy release rates and its mode components at various locations along the delamination front.
- To analyze double cantilever beam and end-notched flexure models of delaminated composite plates with various lay-ups, geometry and material properties.
- To perform Monte Carlo simulations by considering material properties, mesh density, friction coefficient, virtual crack closure length, ply thickness, fiber orientation and shear correction factors as uncertainties and defining those using appropriate probabilistic distributions.
- To obtain an insight on the effects of uncertainties on the mixed-mode strain energy release rates along the delamination front.

- To perform Anderson-Darling goodness-of-fit test to fit the maximum and average strain energy release rates for each of the mode components to a Weibull, normal or log-normal distribution and calculate statistically-based properties.
- To perform a regression analysis to build the response surface for a unidirectional double cantilever beam model and generate Monte Carlo simulations from the regression equation to study the effects of uncertainties on the maximum and average strain energy release rates for a particular configuration.

2 THEORETICAL FORMULATION

2.1 Introduction

In this chapter the formulations pertinent to this thesis work are summarized. First, the first-order shear deformation theory is reviewed. The subsequent sections are arranged in the following order:

1. The theoretical formulation for evaluating improved transverse shear stiffness, transverse shear stresses and strains, as proposed by Rolfes and Rohwer (1997), is reviewed.
2. The general form of total energy release rate in the presence of crack propagation is given.
3. The evaluation of the total strain energy release rate using a plate-theory-based crack-closure technique applied to a three-dimensional crack-tip element is presented. The transverse stresses and strains calculated in the first step are used in this formulation.
4. If contact elements are used in a finite element model to prevent layer interpenetration and account for sliding friction effects, then formulae for calculating change in total potential energy of the structure in terms of the contact element's output parameters are given.
5. The evaluation of the total strain energy release rate in terms of the values output from the fourth step is presented. Since only two-dimensional end-notched flexure test results are available in the literature, where friction has been taken into account, the procedure for reducing three dimensional analysis results to that of the two dimensional case is provided.
6. After the total strain energy release rate is evaluated, mode decomposition is done by evaluating the mode-I component as the difference between the total SERR and the sum of the mode-II and mode-III components calculated using the formulation given by Wang and Qiao (2004b). Thus the complex analysis that is required in their work for finding the concentrated transverse shear force at the crack-tip is eliminated.

7. Finally the procedures for performing Anderson-Darling goodness-of-fit tests for the two-parameter Weibull, normal and log-normal distributions and for evaluating the nominal values for the SERR values to be obtained from Monte Carlo simulations are provided.

2.2 First-order Shear Deformation Theory

Figure 2.1 shows the stacking sequence of an *N*-layer laminate of thickness *t*. The thickness of each ply is t_k. The mid-surface of the laminate is the reference plane from where the lateral coordinates are measured. z_k and $\bar{z}_k$ are the *z*-coordinates of the top and middle of the k^{th} layer from the reference plane.

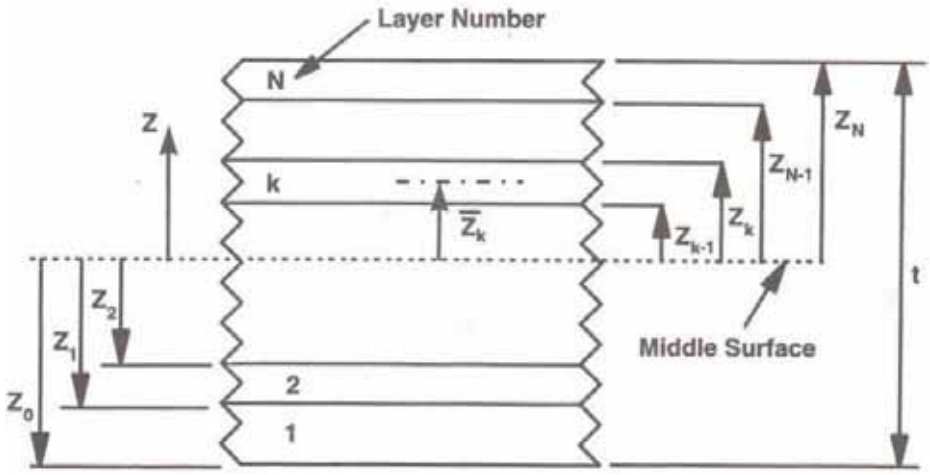

Figure 2.1 Geometry of an *N*-layer laminate [Barbero (1999)]

First-order shear deformation theory can be used to analyze thin to moderately-thick composite structures. It is based on the following assumptions (Barbero 1999):

- A line originally straight and perpendicular to the middle surface remains straight after the plate is deformed (line A-D in Figure 2.2). This implies that the shear strains γ_{xz} and γ_{yz} are constant through the thickness.
- The length of the line A-D in Figure 2.2 is constant. This implies that the normal strain, $\varepsilon_{zz} \cong 0$.

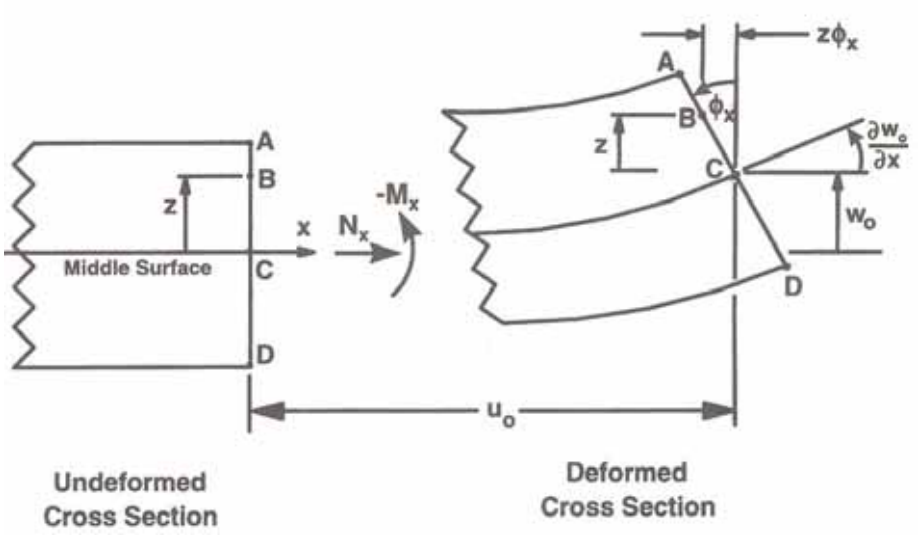

Figure 2.2 Geometry of deformation in the *x*-*z* plane [Barbero (1999)]

Under these assumptions, the displacements at every point through the thickness are,

$$u(x,y,z) = u_0(x,y) - z\phi_x(x,y)$$
$$v(x,y,z) = v_0(x,y) - z\phi_y(x,y)$$
$$w(x,y,z) = w_0(x,y) \tag{2.1}$$

Where, $u(x,y,z)$, $v(x,y,z)$, and $w(x,y,z)$ are the displacements along the x, y and z-directions at each point (x, y, z). The independent variables $u_0(x,y)$, $v_0(x,y)$, and $w_0(x,y)$ represent the displacements of every point (x, y) of the middle surface of the plate. $\phi_x(x,y)$ and $\phi_y(x,y)$ are the rotations of the normal to the middle surface at each point (x, y).

The mid-plane strains $\varepsilon_x^0(x,y)$, $\varepsilon_y^0(x,y)$, and $\gamma_{xy}^0(x,y)$ and the curvatures κ_x , κ_y and κ_{xy} are defined as,

$$\varepsilon_x^0(x,y) = \frac{\partial u_0}{\partial x}$$

$$\varepsilon_y^0(x,y) = \frac{\partial v_0}{\partial y}$$

$$\gamma_{xy}^0(x,y) = \frac{\partial u_0}{\partial y} + \frac{\partial v_0}{\partial x}$$

$$\kappa_x(x,y) = -\frac{\partial \phi_x}{\partial x}$$

$$\kappa_y(x,y) = -\frac{\partial \phi_y}{\partial y}$$

$$\kappa_{xy}(x,y) = -\left(\frac{\partial \phi_x}{\partial y} + \frac{\partial \phi_y}{\partial x}\right) \tag{2.2}$$

The in-plane strains $\varepsilon_x, \varepsilon_y$, and γ_{xy} at any point in the plate are given by,

$$\begin{Bmatrix} \varepsilon_x \\ \varepsilon_y \\ \gamma_{xy} \end{Bmatrix} = \begin{Bmatrix} \varepsilon_x^0 \\ \varepsilon_y^0 \\ \gamma_{xy}^0 \end{Bmatrix} + z \begin{Bmatrix} \kappa_x \\ \kappa_y \\ \kappa_{xy} \end{Bmatrix} \tag{2.3}$$

The interlaminar shear strains γ_{yz} and γ_{yz} are defined as,

$$\gamma_{yz}(x,y,z) = -\phi_y + \frac{\partial w_0}{\partial y}$$

$$\gamma_{xz}(x,y,z) = -\phi_x + \frac{\partial w_0}{\partial x} \tag{2.4}$$

The stress-strain relation in material coordinates are given by

$$\begin{Bmatrix} \sigma_1 \\ \sigma_2 \\ \sigma_6 \end{Bmatrix}^k = \begin{bmatrix} Q_{11} & Q_{12} & 0 \\ Q_{12} & Q_{22} & 0 \\ 0 & 0 & Q_{66} \end{bmatrix}^k \begin{Bmatrix} \varepsilon_1 \\ \varepsilon_2 \\ \gamma_6 \end{Bmatrix}^k$$

$$\begin{Bmatrix} \sigma_4 \\ \sigma_5 \end{Bmatrix}^k = \begin{bmatrix} Q_{44}^* & 0 \\ 0 & Q_{55}^* \end{bmatrix}^k \begin{Bmatrix} \gamma_4 \\ \gamma_5 \end{Bmatrix}^k \tag{2.5}$$

Where, the superscript *k* indicates the layer number. The coefficients are defined as,

$$Q_{11} = \frac{E_1}{\Delta}$$

$$Q_{22} = \frac{E_2}{\Delta}$$

$$Q_{12} = \frac{\nu_{12} E_2}{\Delta}$$

$$Q_{66} = G_{12}$$

$$Q_{44}^{*} = G_{23}$$

$$Q_{55}^{*} = G_{13}$$

$$\Delta = 1 - \nu_{12}\nu_{21}$$

With,

E_1 - Longitudinal modulus

E_2 - Transverse modulus

ν_{12}, ν_{21} - Poisson's ratios

G_{12} - In-plane shear modulus

G_{13}, G_{23} - Transverse shear modulus

The stress-strain relation in global coordinates is given by,

$$\begin{Bmatrix} \sigma_x \\ \sigma_y \\ \sigma_{xy} \end{Bmatrix}^k = \begin{bmatrix} \overline{Q}_{11} & \overline{Q}_{12} & \overline{Q}_{16} \\ \overline{Q}_{12} & \overline{Q}_{22} & \overline{Q}_{26} \\ \overline{Q}_{16} & \overline{Q}_{26} & \overline{Q}_{66} \end{bmatrix}^k \begin{Bmatrix} \varepsilon_x \\ \varepsilon_y \\ \gamma_{xy} \end{Bmatrix}^k$$

$$\begin{Bmatrix} \sigma_{yz} \\ \sigma_{xz} \end{Bmatrix}^k = \begin{bmatrix} \overline{Q}_{44}^{*} & \overline{Q}_{45}^{*} \\ \overline{Q}_{45}^{*} & \overline{Q}_{55}^{*} \end{bmatrix}^k \begin{Bmatrix} \gamma_{yz} \\ \gamma_{xz} \end{Bmatrix}^k \qquad (2.6)$$

For the k^{th} layer with ply orientation θ, the coefficients are defined as,

$$\overline{Q}_{11} = Q_{11}\cos^4\theta + 2(Q_{12} + 2Q_{66})\sin^2\theta\cos^2\theta + Q_{22}\sin^4\theta$$

$$\overline{Q}_{12} = (Q_{11} + Q_{22} - 4Q_{66})\sin^2\theta\cos^2\theta + Q_{12}(\sin^4\theta + \cos^4\theta)$$

$$\overline{Q}_{22} = Q_{11}\sin^4\theta + 2(Q_{12} + 2Q_{66})\sin^2\theta\cos^2\theta + Q_{22}\cos^4\theta$$

$$\overline{Q}_{16} = (Q_{11} - Q_{12} - 2Q_{66})\sin\theta\cos^3\theta + (Q_{12} - Q_{22} + 2Q_{66})\sin^3\theta\cos\theta$$

$$\overline{Q}_{26} = (Q_{11} - Q_{12} - 2Q_{66})\cos\theta\sin^3\theta + (Q_{12} - Q_{22} + 2Q_{66})\cos^3\theta\sin\theta$$

$$\overline{Q}_{66} = (Q_{11} + Q_{22} - 2Q_{12} - 2Q_{66})\sin^2\theta\cos^2\theta + Q_{66}(\sin^4\theta + \cos^4\theta)$$

$$\overline{Q}^*_{44} = Q^*_{44}\cos^2\theta + Q^*_{55}\sin^2\theta$$

$$\overline{Q}^*_{55} = Q^*_{55}\cos^2\theta + Q^*_{44}\sin^2\theta$$

$$\overline{Q}^*_{45} = (Q^*_{55} - Q^*_{44})\sin\theta\cos\theta$$

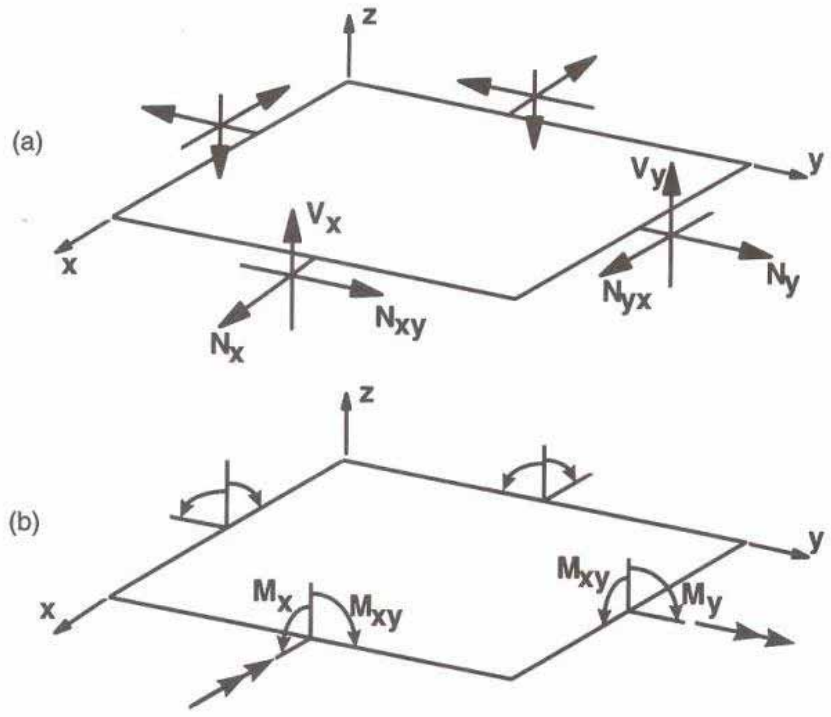

Figure 2.3 Force and moment resultants on a flat plate [Barbero (1999)]

The resultant forces and moments shown in Figure 2.3 are given by,

$$\begin{Bmatrix} N_x \\ N_y \\ N_{xy} \end{Bmatrix} = \int_{-t/2}^{t/2} \begin{Bmatrix} \sigma_x \\ \sigma_y \\ \sigma_{xy} \end{Bmatrix} dz$$

$$\begin{Bmatrix} M_x \\ M_y \\ M_{xy} \end{Bmatrix} = \int_{-t/2}^{t/2} \begin{Bmatrix} \sigma_x \\ \sigma_y \\ \sigma_{xy} \end{Bmatrix} z\,dz$$

$$\begin{Bmatrix} Q_{yz} \\ Q_{xz} \end{Bmatrix} = \int_{-t/2}^{t/2} \begin{Bmatrix} \sigma_{yz} \\ \sigma_{xz} \end{Bmatrix} dz \tag{2.7}$$

$\{N\}$, $\{M\}$ and $\{Q\}$ are the in-plane force resultants, bending moment resultants and transverse shear forces respectively. The notations for the transverse shear forces have been changed from V_x and V_y in Figure 2.3 to Q_{xz} and Q_{yz} to be consistent with the other formulations used in this thesis work.

The plate stiffness equations are,

$$\begin{Bmatrix} N_x \\ N_y \\ N_{xy} \\ M_x \\ M_y \\ M_{xy} \end{Bmatrix} = \begin{bmatrix} A_{11} & A_{12} & A_{16} & B_{11} & B_{12} & B_{16} \\ A_{12} & A_{22} & A_{26} & B_{12} & B_{22} & B_{26} \\ A_{16} & A_{26} & A_{66} & B_{16} & B_{26} & B_{66} \\ B_{11} & B_{12} & B_{16} & D_{11} & D_{12} & D_{16} \\ B_{12} & B_{22} & B_{26} & D_{12} & D_{22} & D_{26} \\ B_{16} & B_{26} & B_{66} & D_{16} & D_{26} & D_{66} \end{bmatrix} \begin{Bmatrix} \varepsilon_x^0 \\ \varepsilon_y^0 \\ \gamma_{xy}^0 \\ \kappa_x \\ \kappa_y \\ \kappa_{xy} \end{Bmatrix}$$

$$\begin{Bmatrix} Q_{yz} \\ Q_{xz} \end{Bmatrix} = \begin{bmatrix} H_{44} & H_{45} \\ H_{45} & H_{55} \end{bmatrix} \begin{Bmatrix} \gamma_{yz} \\ \gamma_{xz} \end{Bmatrix} \tag{2.8}$$

The coefficients are defined as,

$$A_{ij} = \sum_{k=1}^{N} (\overline{Q}_{ij})_k \, t_k \qquad \text{i, j = 1, 2, 6}$$

$$B_{ij} = \sum_{k=1}^{N} (\overline{Q}_{ij})_k \, t_k \, \bar{z}_k \qquad \text{i, j = 1, 2, 6}$$

$$D_{ij} = \sum_{k=1}^{N} (\overline{Q}_{ij})_k \left(t_k \bar{z}_k^2 + \frac{t_k^3}{12} \right) \qquad \text{i, j = 1, 2, 6}$$

$$H_{ij} = \sum_{k=1}^{N} (\overline{Q}^{*}_{ij})_k \, t_k \qquad \text{i, j = 4, 5} \tag{2.9}$$

Where, [*A*], [*D*], [*B*] are the in-plane, bending and bending-extension coupling stiffness respectively.

The plate compliance equations are given by,

$$\begin{Bmatrix} \varepsilon_x^0 \\ \varepsilon_y^0 \\ \gamma_{xy}^0 \\ \kappa_x \\ \kappa_y \\ \kappa_{xy} \end{Bmatrix} = \begin{bmatrix} \alpha_{11} & \alpha_{12} & \alpha_{16} & \beta_{11} & \beta_{12} & \beta_{16} \\ \alpha_{12} & \alpha_{22} & \alpha_{26} & \beta_{12} & \beta_{22} & \beta_{26} \\ \alpha_{16} & \alpha_{26} & \alpha_{66} & \beta_{16} & \beta_{26} & \beta_{66} \\ \beta_{11} & \beta_{12} & \beta_{16} & \delta_{11} & \delta_{12} & \delta_{16} \\ \beta_{12} & \beta_{22} & \beta_{26} & \delta_{12} & \delta_{22} & \delta_{26} \\ \beta_{16} & \beta_{26} & \beta_{66} & \delta_{16} & \delta_{26} & \delta_{66} \end{bmatrix} \begin{Bmatrix} N_x \\ N_y \\ N_{xy} \\ M_x \\ M_y \\ M_{xy} \end{Bmatrix}$$

$$\begin{Bmatrix} \gamma_{yz} \\ \gamma_{xz} \end{Bmatrix} = \begin{bmatrix} h_{44} & h_{45} \\ h_{45} & h_{55} \end{bmatrix} \begin{Bmatrix} Q_{yz} \\ Q_{xz} \end{Bmatrix} \tag{2.10}$$

Where, $\begin{bmatrix} \alpha & \beta \\ \beta & \delta \end{bmatrix}$ and [*h*] are the compliance coefficients.

2.3 Improved Transverse Shear Stress Evaluation

This section reviews the formulation given in Rolfes and Rohwer (1997) for finding the improved transverse shear stiffness and the matrices required for evaluating

accurate transverse shear stresses and strains.

The transverse shear stress distribution for a laminated composite is,

$$\begin{Bmatrix} \tau_{xz} \\ \tau_{yz} \end{Bmatrix}^{(k)} = \begin{bmatrix} \overline{Q}^{*}_{55} & \overline{Q}^{*}_{45} \\ \overline{Q}^{*}_{45} & \overline{Q}^{*}_{44} \end{bmatrix}^{(k)} \begin{Bmatrix} \gamma_{xz} \\ \gamma_{yz} \end{Bmatrix} \tag{2.11}$$

Where,

$\{\tau\}$ - Transverse shear stresses

$\{\gamma\}$ - Transverse shear strains

$\left[\overline{Q}^{*}\right]$ - Transformed interlaminar stiffness matrix

The transverse shear forces are given by,

$$\begin{Bmatrix} Q_{xz} \\ Q_{yz} \end{Bmatrix} = \begin{bmatrix} H_{55} & H_{45} \\ H_{45} & H_{44} \end{bmatrix} \begin{Bmatrix} \gamma_{xz} \\ \gamma_{yz} \end{Bmatrix} \tag{2.12}$$

Where,

$\{Q\}$ – Transverse shear forces

With transverse shear stiffness

$$[H] = \sum_{k=1}^{n} \left[\overline{Q}^{*}\right]^{(k)} t^{(k)} \tag{2.13}$$

Where, $t^{(k)}$ is the thickness of the k^{th} ply.

A shear correction factor of 5/6 is usually used to account for a parabolic distribution of shear stress that vanishes on the surfaces of the laminate. But this

assumption is valid only for a single layer isotropic plate. Rolfes and Rohwer (1997) used the equilibrium approach and assumed two cylindrical bending displacement modes to provide accurate shear stiffness and transverse shear stresses. The procedure is as follows.

The equilibrium equations of a plate, neglecting body forces are

$$\begin{Bmatrix} \sigma_{x,x} + \tau_{xy,y} + \tau_{xz,z} = 0 \\ \sigma_{y,y} + \tau_{yz,z} + \tau_{xy,x} = 0 \\ \sigma_{z,z} + \tau_{xz,x} + \tau_{yz,y} = 0 \end{Bmatrix} \tag{2.14}$$

Equation (2.14) solved with respect to the transverse shear stresses in the k^{th} lamina at any point $\zeta = z$ along the transverse direction gives

$$\begin{bmatrix} \tau_{xz}^{(k)} \\ \tau_{yz}^{(k)} \end{bmatrix} = -\int_{\zeta=0}^{\zeta=z} \begin{pmatrix} \sigma_{x,x}^{(k)} + \tau_{xy,y}^{(k)} \\ \sigma_{y,y}^{(k)} + \tau_{xy,x}^{(k)} \end{pmatrix} d\zeta \tag{2.15}$$

Where, the coordinate ζ starts at the bottom surface of the laminate.

The in-plane stresses at the k^{th} lamina are given by

$$\{\sigma\}^{(k)} = \begin{bmatrix} \sigma_x \\ \sigma_y \\ \tau_{xy} \end{bmatrix}^{(k)} = [\overline{Q}]^{(k)} (\{\varepsilon^0\} + z\{k\}) \tag{2.16}$$

Where $[\overline{Q}]^{(k)}$ is the reduced stiffness matrix of the k^{th} lamina and $\{\varepsilon^0\}$ and $\{k\}$ denote the mid-plane strains and curvatures of the laminate respectively.

Using equation (2.16) in equation (2.15) yields

$$\{\tau\} = -\int_{\zeta=0}^{\zeta=z} ([B_1][\overline{Q}]^{(k)} (\{\varepsilon^0\}_{,x} + z\{k\}_{,x}) + [B_2][\overline{Q}]^{(k)} (\{\varepsilon^0\}_{,y} + z\{k\}_{,y})) d\zeta \tag{2.17}$$

$[B_1]$ and $[B_2]$ are Boolean matrices of the form

$$[B_1] = \begin{bmatrix} 1 & 0 & 0 \\ 0 & 0 & 1 \end{bmatrix} \tag{2.18}$$

$$[B_2] = \begin{bmatrix} 0 & 0 & 1 \\ 0 & 1 & 0 \end{bmatrix} \tag{2.19}$$

The constitutive equation for a laminate is

$$\begin{bmatrix} N \\ M \end{bmatrix} = \begin{bmatrix} A & B \\ B & D \end{bmatrix} \begin{bmatrix} \varepsilon^0 \\ k \end{bmatrix} \tag{2.20}$$

$$[N] = \begin{bmatrix} N_x \\ N_y \\ N_{xy} \end{bmatrix} \tag{2.21}$$

$$[M] = \begin{bmatrix} M_x \\ M_y \\ M_{xy} \end{bmatrix} \tag{2.22}$$

Since the influence of membrane forces on the transverse shear stresses is very small, the laminate strains can be expressed only in terms of the moments as,

$$\{\varepsilon^0\} = -[A]^{-1}[B]\{k\} \tag{2.23}$$

And

$$\{k\} = [D^*]^{-1}[M] \tag{2.24}$$

Where,

$$[D^*] = ([D] - [B]^T [A]^{-1} [B]) \tag{2.25}$$

Substituting equations (2.23)-(2.25) into equation (2.17) provides transverse shear stresses only depending on the moment derivatives w.r.t. x and y,

$$\{\tau\} = -[B_1][F(z)][M]_{,x} - [B_2][F(z)][M]_{,y} \tag{2.26}$$

With $[F(z)]$ defined as,

$$[F(z)] = ([a(z)]\,[A]^{-1}\,[B] - [b(z)])\,[D^*]^{-1} \tag{2.27}$$

Where $[a(z)]$ and $[b(z)]$ are the partial membrane and bending-extension coupling stiffness matrices of the laminate, respectively, which are the $[A]$ and $[B]$ matrices calculated from the bottom surface of the laminate to the z-coordinate where transverse stresses are to be calculated.

$$[a(z)] = \int_{\varsigma=0}^{\varsigma=z} [\overline{Q}]\, d\varsigma \tag{2.28}$$

$$[b(z)] = \int_{\varsigma=0}^{\varsigma=z} [\overline{Q}]\varsigma\, d\varsigma \tag{2.29}$$

Assuming cylindrical bending around the x-axis yields,

$$[M]_{,x} = \begin{bmatrix} M_{x,x} \\ 0 \\ 0 \end{bmatrix} \tag{2.30}$$

And around the y-axis yields,

$$[M]_{,y} = \begin{bmatrix} 0 \\ M_{y,y} \\ 0 \end{bmatrix} \tag{2.31}$$

Then, according to Rolfes and Rohwer (1997), from the equilibrium conditions of a plate, the derivatives of the moments can be related to the shear forces via,

$$\{Q_{xz}\} = -M_{x,x} \tag{2.32}$$

And

$$\{Q_{yz}\} = -M_{y,y} \tag{2.33}$$

Which, finally results in

$$\{\tau\} = \begin{bmatrix} F_{11} & F_{32} \\ F_{31} & F_{22} \end{bmatrix} \begin{Bmatrix} Q_{xz} \\ Q_{yz} \end{Bmatrix} \tag{2.34}$$

or

$$\{\tau\} = [f(z)]\{Q\} \tag{2.35}$$

Where, $[f(z)]$ is the reduced $[F(z)]$ matrix.

The complementary transverse shear energy in terms of shear stresses is

$$U_0 = \frac{1}{2} \int_{z=-t/2}^{z=t/2} \{\tau\}^T [\overline{Q}^*]^{-1} \{\tau\} dz \tag{2.36}$$

Where, t is the laminate thickness.

And in terms of shear forces is

$$U_0 = \frac{1}{2}\{R\}^T \overline{[H]}^{-1}\{R\} \tag{2.37}$$

Introducing equation (2.35) into equation (2.36) and comparing with equation (2.37) provides the expression for the improved transverse shear stiffness based on the equilibrium approach,

$$[\overline{H}] = \left[\int_{z=-t/2}^{z=t/2} [f(z)]^T [\overline{Q}^*]^{-1} [f(z)]\, dz\right]^{-1} \tag{2.38}$$

2.4 Total Strain Energy Release Rate

When a delamination of length 'a' propagates by a small distance 'δa' the total strain energy release rate is given by,

$$G = \frac{\Delta\Pi}{\Delta A} \tag{2.39}$$

Where,

$\Delta\Pi$ = Change in total potential energy

ΔA = Increase in crack area

When kinetic energy, work done by external forces and contact friction are zero and if there are no plasticity effects and stress stiffening effects,

$$G = \frac{\Delta U}{\Delta A} \tag{2.40}$$

Where,

ΔU = Change in elastic strain energy

2.5 Three Dimensional Crack-tip Element

Whitcomb and Shivakumar (1989) have proposed a plate theory-based crack closure procedure where the total strain energy release rate during crack growth is calculated as the work required for changing the mid-plane strains and curvatures at the crack front in the cracked region to be equal to those in the uncracked region.

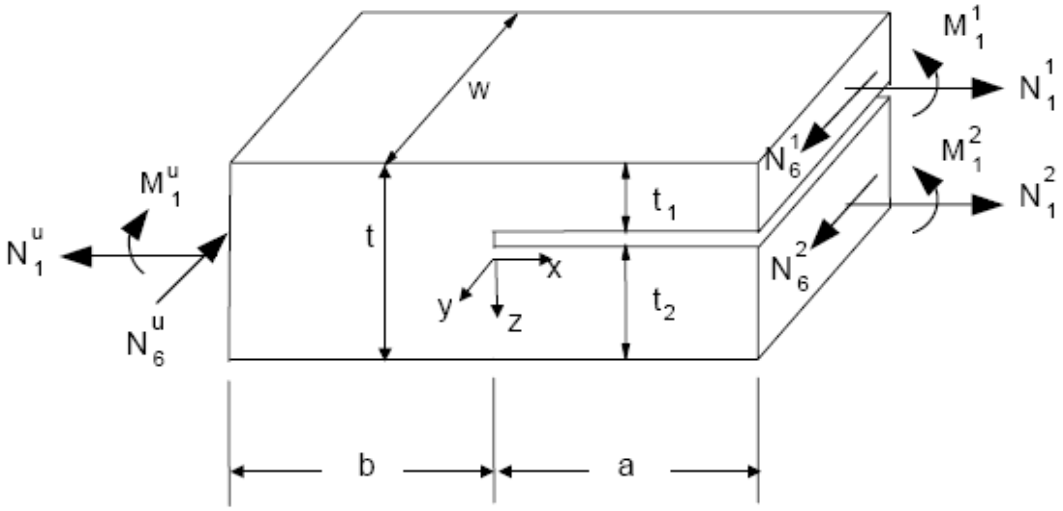

Figure 2.4 Three dimensional crack-tip element [Davidson (2001)]

A Crack-tip element is a portion of the laminate near the delamination front as shown in Figure 2.4. Davidson (2001) has used a procedure similar to that of Whitcomb and Shivakumar (1989) to calculate the total energy release rate using the force and moment resultants acting on the crack-tip element. Loads are applied away from the crack-tip and the loading on the crack-tip element is determined analytically or using numerical methods. Their formulation is based on CLPT and so the transverse shear forces are not shown in the figure. The total energy release rate is calculated as,

$$G = \frac{1}{2}\sum_{p=1}^{2}\left(\{\Delta N\} * \{\Delta \varepsilon^0\} + \{\Delta M\} * \{\Delta \kappa\}\right)_p \tag{2.41}$$

The notations have been changed to be consistent with the ones previously used in this work. Here, p = 1, 2 refers to the portions of the laminate above and below the delamination plane respectively. $\{\Delta \varepsilon^0\}$, $\{\Delta \kappa\}$ represent the change in mid-plane strains

and curvatures required for crack closure and $\{\Delta N\}$, $\{\Delta M\}$ are the corresponding change in force and moment resultants respectively.

In this section, an attempt is made to extend the formulation to account for transverse shear deformations.

Strains, and curvatures in the cracked region:

$$\begin{Bmatrix} \varepsilon^0 \\ k \end{Bmatrix}_c^p = \begin{bmatrix} \alpha & \beta \\ \beta & \delta \end{bmatrix}^p \begin{Bmatrix} N \\ M \end{Bmatrix}_c^p \tag{2.42}$$

Transverse shear strains in the cracked region:

$$\begin{Bmatrix} \gamma_{xz} \\ \gamma_{yz} \end{Bmatrix}_c^p = \begin{bmatrix} \bar{h}_{55} & \bar{h}_{45} \\ \bar{h}_{45} & \bar{h}_{44} \end{bmatrix}^p \begin{Bmatrix} Q_{xz} \\ Q_{yz} \end{Bmatrix}_c^p \tag{2.43}$$

Where,

$$\begin{bmatrix} \bar{h}_{55} & \bar{h}_{45} \\ \bar{h}_{45} & \bar{h}_{44} \end{bmatrix}^p = \left[\bar{\mathrm{H}}^{-1}\right]^p$$

With p = 1, 2 for upper and lower sub-laminates and the subscript 'c' indicates that these values are from the cracked region of the laminate.

Total resultant forces, moments and transverse shear forces at mid-plane of the uncracked region are,

$$\begin{aligned} \{N\}_u &= \{N\}_u^1 + \{N\}_u^2 \\ \{M\}_u &= \{M\}_u^1 + \{M\}_u^2 + \frac{t_1}{2}\{N\}_u^2 - \frac{t_2}{2}\{N\}_u^1 \\ \{Q\}_u &= \{Q\}_u^1 + \{Q\}_u^2 \end{aligned} \tag{2.44}$$

Where, the subscript '*u*' indicates that these values are from the uncracked region of the laminate and t_1 and t_2 are the thickness of plates 1 and 2 respectively.

Strains and curvatures at mid-plane of the uncracked region:

$$\begin{Bmatrix} \varepsilon^0 \\ k \end{Bmatrix}_u = \begin{bmatrix} \alpha & \beta \\ \beta & \delta \end{bmatrix}_u \begin{Bmatrix} N \\ M \end{Bmatrix}_u \tag{2.45}$$

Strains and curvatures at the mid-plane of plates 1 & 2 in the uncracked region:

$$\begin{aligned} \{\varepsilon^0\}_u^1 &= \{\varepsilon^0\}_u - \frac{t_2}{2}\{k\}_u \\ \{\varepsilon^0\}_u^2 &= \{\varepsilon^0\}_u + \frac{t_1}{2}\{k\}_u \\ \{k\}_u^1 &= \{k\}_u^2 = \{k\}_u \end{aligned} \tag{2.46}$$

Transverse shear stresses at midplanes of plates 1 & 2 in the uncracked region:

$$\begin{Bmatrix} \tau_{xz} \\ \tau_{yz} \end{Bmatrix}_u^1 = \begin{bmatrix} F_{11} & F_{32} \\ F_{31} & F_{22} \end{bmatrix}_{z=t_1/2} \begin{Bmatrix} Q_{xz} \\ Q_{yz} \end{Bmatrix}_u \tag{2.47}$$

$$\begin{Bmatrix} \tau_{xz} \\ \tau_{yz} \end{Bmatrix}_u^2 = \begin{bmatrix} F_{11} & F_{32} \\ F_{31} & F_{22} \end{bmatrix}_{z=t_1+\frac{t_2}{2}} \begin{Bmatrix} Q_{xz} \\ Q_{yz} \end{Bmatrix}_u \tag{2.48}$$

Transverse shear strains at midplanes of plates 1 & 2 in the uncracked region:

$$\begin{Bmatrix} \gamma_{xz} \\ \gamma_{yz} \end{Bmatrix}_u^p = \begin{bmatrix} \overline{S*}_{55} & \overline{S*}_{45} \\ \overline{S*}_{45} & \overline{S*}_{44} \end{bmatrix}^p \begin{Bmatrix} \tau_{xz} \\ \tau_{yz} \end{Bmatrix}_u^p \tag{2.49}$$

Where,

$\begin{bmatrix} \overline{S^*}_{55} & \overline{S^*}_{45} \\ \overline{S^*}_{45} & \overline{S^*}_{44} \end{bmatrix}^p$ is the transverse shear compliance of the mid-layers of plates 1 & 2.

Changes in force and moment resultants, transverse shear forces, strains, curvatures and transverse shear strains due to a change in the crack surface area, ΔA, can be represented as,

$$\begin{Bmatrix} \Delta\varepsilon^0 \\ \Delta k \end{Bmatrix}^p = \begin{Bmatrix} \varepsilon^0 \\ k \end{Bmatrix}_u^p - \begin{Bmatrix} \varepsilon^0 \\ k \end{Bmatrix}_c^p \tag{2.50}$$

$$\begin{Bmatrix} \Delta\gamma_{xz} \\ \Delta\gamma_{yz} \end{Bmatrix}^p = \begin{Bmatrix} \gamma_{xz} \\ \gamma_{yz} \end{Bmatrix}_u^p - \begin{Bmatrix} \gamma_{xz} \\ \gamma_{yz} \end{Bmatrix}_c^p \tag{2.51}$$

$$\begin{Bmatrix} \Delta N \\ \Delta M \end{Bmatrix}^p = \begin{bmatrix} A & B \\ B & D \end{bmatrix}^p \begin{Bmatrix} \Delta\varepsilon^0 \\ \Delta k \end{Bmatrix}^p \tag{2.52}$$

$$\begin{Bmatrix} \Delta Q_{xz} \\ \Delta Q_{yz} \end{Bmatrix}^p = \begin{bmatrix} \overline{H}_{55} & \overline{H}_{45} \\ \overline{H}_{45} & \overline{H}_{44} \end{bmatrix}^p \begin{Bmatrix} \Delta\gamma_{xz} \\ \Delta\gamma_{yz} \end{Bmatrix}^p \tag{2.53}$$

Finally the total strain energy release rate is given by,

$$G = \frac{1}{2}\sum_{p=1}^{2} (\Delta N_x * \Delta\varepsilon_x^0 + \Delta N_y * \Delta\varepsilon_y^0 + \Delta N_{xy} * \Delta\gamma_{xy}^0 + \Delta M_x * \kappa_x + \Delta M_y * \kappa_y + \Delta M_{xy} * \kappa_{xy} + \Delta Q_{xz} * \Delta\gamma_{xz} + \Delta Q_{yz} * \Delta\gamma_{yz})_p \tag{2.54}$$

2.6 Prevention of Layer Interpenetration

When surface-to-surface contact elements are used in the cracked region to prevent interpenetration of the two sublaminates, even if the penetration tolerance is kept small and the contact stiffness kept at a reasonable value so as to avoid convergence problems, there will be an infinitesimal amount of penetration. So a small fraction of strain energy gets locked up in the contact elements. During frictionless contact, this

energy can be evaluated by selecting all the contact elements that have undergone penetration and calculating the sum of their strain energies. It is given by,

$$W^p = \frac{1}{2}\sum_{i=1}^{n}(CNFZ * pene)_i \tag{2.55}$$

Where,

$CNFZ$ = Contact force of each contact element in the normal direction

$pene$ = Penetration of each contact element

n = Number of contact elements in the cracked region with $pene > 0$

When the influence of friction between the crack surfaces is neglected, the change in potential energy is given by

$$\Delta\Pi = \Delta U - W^p \tag{2.56}$$

And the total strain energy release rate is

$$G = \frac{\Delta U}{\Delta A} - \frac{W^p}{\Delta A} \tag{2.57}$$

2.7 Influence of Friction

When the influence of friction between the crack surfaces is considered, the energy lost to friction forces is given by

$$W^f = \sum_{i=1}^{n}(CNFX * tasx)_i + (CNFY * tasy)_i \tag{2.58}$$

Where,

$CNFX$ = X-component of contact element force

CNFY = *Y*-component of contact element force

tasx = Total accumulated sliding in the *X*-direction

tasy = Total accumulated sliding in the *Y*-direction

The change in total potential energy is given by

$$\Delta\Pi = \Delta U - W^{p} + W^{f} \tag{2.59}$$

And the total strain energy release rate is

$$G = \frac{\Delta U}{\Delta A} - \frac{W^{p}}{\Delta A} + \frac{W^{f}}{\Delta A} \tag{2.60}$$

2.8 Total Energy Release Rate for comparison with Two Dimensional End-notched Flexure Tests

An end-notched flexure specimen is shown in Figure 4.11. Let Γ_a be the crack surface for a crack length of '*a*'. The length of the crack-tip elements must be '2*δa' so that the distance between the centroid of the element in the cracked region (or the uncracked region) and the delamination front is 'δa' which is the incremental crack length.

Strain energy of crack-tip element in the cracked region,

$$U_c = U_c^1 + U_c^2 \tag{2.61}$$

Where,

U_c^1 = Strain energy of the crack-tip element in the cracked region of upper plate

U_c^2 = Strain energy of the crack-tip element in the cracked region of lower plate

Strain energy of crack-tip element in the uncracked region,

$$U_u = U_u^1 + U_u^2 \tag{2.62}$$

Where,

U_u^1 = Strain energy of the crack-tip element in the uncracked region of upper plate

U_u^2 = Strain energy of the crack-tip element in the uncracked region of lower plate

Change in elastic strain energy (for virtual crack closure),

$$\Delta U = \sum_{i=1}^{k} (U_c - U_u)_i \tag{2.63}$$

Where, 'k' is the number of crack-tip elements along the delamination front

Change in total potential energy,

$$\Delta\Pi = \Delta U - W^p\Big|_{\Gamma_a} + W^f\Big|_{\Gamma_a} \tag{2.64}$$

Total strain energy release rate,

$$\mathrm{G} = \frac{\Delta\Pi}{k\,\Delta A} \tag{2.65}$$

There will be a small difference between the strain energy release rate values obtained by a two-step approach and this one-step approach. This is due to the fact that, the presence of friction makes the problem path-dependent and also because $W^p\Big|_{\Gamma_{\delta a}}$ and $W^f\Big|_{\Gamma_{\delta a}}$ cannot be accounted for in the one-step approach since,

$$W^f\Big|_{\Gamma_{a+\delta a}} \neq W^f\Big|_{\Gamma_a} + W^f\Big|_{\Gamma_{\delta a}} \tag{2.66}$$

$$W^p\Big|_{\Gamma_{a+\delta a}} \neq W^p\Big|_{\Gamma_a} + W^p\Big|_{\Gamma_{\delta a}} \tag{2.67}$$

So, the energy dissipation due to finite crack extension cannot be taken into account in the one-step approach. The difference can be minimized by decreasing the virtual crack

closure length.

2.9 Mode Decomposition of Total Strain Energy Release Rate

Wang and Qiao (2004b) computed the total strain energy release rate and its components in terms of three concentrated crack tip forces N_{xc}, N_{xyc} and Q_{xc} shown in the Figure (2.5) as follows:

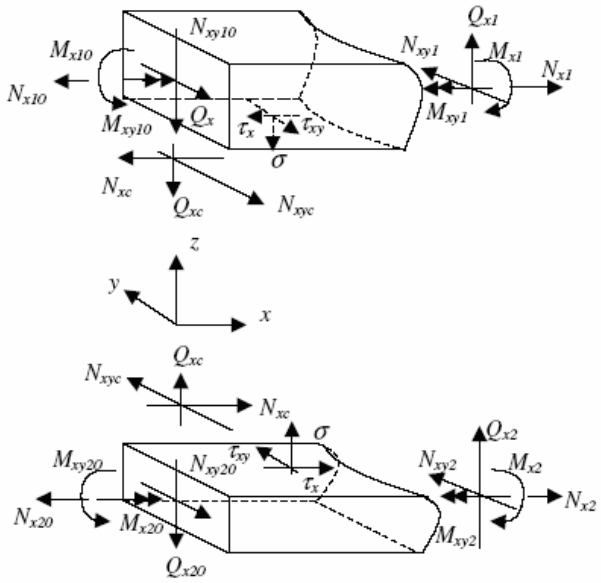

Figure 2.5 Stress resultants at the crack tip [Wang and Qiao (2004b)]

The mode-I, mode-II, and mode-III strain energy release rates are given by,

$$G_I = \frac{1}{2}\delta_Q Q_{xc}^2 \tag{2.68}$$

$$G_{II} = \frac{1}{2}(\delta_{11c} N_{xc}^2 + \delta_{16c} N_{xc} N_{xyc}) \tag{2.69}$$

$$G_{III} = \frac{1}{2}(\delta_{16c} N_{xc} N_{xyc} + \delta_{66c} N_{xyc}^2) \tag{2.70}$$

Total strain energy release rate is the sum of the individual components and is given by,

$$G = \frac{1}{2}(\delta_{11c} N_{xc}^2 + 2\delta_{16c} N_{xc} N_{xyc} + \delta_{66c} N_{xyc}^2 + \delta_Q Q_{xc}^2) \tag{2.71}$$

Where,

$$\delta_{11c} = \alpha_{11}^{(1)} + \alpha_{11}^{(2)} - \beta_{11}^{(1)} t_1 + \beta_{11}^{(2)} t_2 + \frac{t_1^2}{4}\delta_{11}^{(1)} + \frac{t_2^2}{4}\delta_{11}^{(2)} \tag{2.72}$$

$$\delta_{16c} = \alpha_{16}^{(1)} + \alpha_{16}^{(2)} - \beta_{16}^{(1)} t_1 + \beta_{16}^{(2)} t_2 + \frac{t_1^2}{4}\delta_{16}^{(1)} + \frac{t_2^2}{4}\delta_{16}^{(2)} \tag{2.73}$$

$$\delta_{66c} = \alpha_{66}^{(1)} + \alpha_{66}^{(2)} - \beta_{66}^{(1)} t_1 + \beta_{66}^{(2)} t_2 + \frac{t_1^2}{4}\delta_{66}^{(1)} + \frac{t_2^2}{4}\delta_{66}^{(2)} \tag{2.74}$$

$$\delta_Q = (\alpha_{55}^{(1)} + \alpha_{55}^{(2)}) \tag{2.75}$$

Where, $\begin{bmatrix} \alpha & \beta \\ \beta & \delta \end{bmatrix}^{(i)}$ i = 1, 2 are the compliance matrices of plates 1 and 2

The in-plane concentrated forces are computed as,

$$\begin{pmatrix} N_{xc} \\ N_{xyc} \end{pmatrix} = \begin{pmatrix} R_{11} - \frac{t_1}{2}Q_{11} & R_{16} - \frac{t_1}{2}Q_{16} \\ R_{16} - \frac{t_1}{2}Q_{16} & R_{66} - \frac{t_1}{2}Q_{66} \end{pmatrix}^{-1} X \begin{pmatrix} R_{11}N_x^{c1} + R_{12}N_y^{c1} + R_{16}N_{xy}^{c1} + Q_{11}M_x^{c1} + Q_{12}M_y^{c1} + Q_{16}M_{xy}^{c1} \\ R_{16}N_x^{c1} + R_{26}N_y^{c1} + R_{66}N_{xy}^{c1} + Q_{16}M_x^{c1} + Q_{26}M_y^{c1} + Q_{66}M_{xy}^{c1} \end{pmatrix} \tag{2.76}$$

With the coefficients defined as,

$$R_{11} = \alpha_{11}^{(1)} + \alpha_{11}^{(2)} - \beta_{11}^{(1)}\frac{t_1}{2} + \beta_{11}^{(2)}\frac{t_2}{2} + \frac{t_1 + t_2}{2}\beta_{11}^{(2)} + \frac{t_2(t_1 + t_2)}{4}\delta_{11}^{(2)} \tag{2.77}$$

$$R_{12} = \alpha_{12}^{(1)} + \alpha_{12}^{(2)} - \beta_{12}^{(1)}\frac{t_1}{2} + \beta_{12}^{(2)}\frac{t_2}{2} + \frac{t_1 + t_2}{2}\beta_{12}^{(2)} + \frac{t_2(t_1 + t_2)}{4}\delta_{12}^{(2)} \tag{2.78}$$

$$R_{16} = \alpha_{16}^{(1)} + \alpha_{16}^{(2)} - \beta_{16}^{(1)}\frac{t_1}{2} + \beta_{16}^{(2)}\frac{t_2}{2} + \frac{t_1 + t_2}{2}\beta_{16}^{(2)} + \frac{t_2(t_1 + t_2)}{4}\delta_{16}^{(2)} \tag{2.79}$$

$$R_{26} = \alpha_{26}^{(1)} + \alpha_{26}^{(2)} - \beta_{26}^{(1)}\frac{t_1}{2} + \beta_{26}^{(2)}\frac{t_2}{2} + \frac{t_1 + t_2}{2}\beta_{26}^{(2)} + \frac{t_2(t_1 + t_2)}{4}\delta_{26}^{(2)} \tag{2.80}$$

$$R_{66} = \alpha_{66}^{(1)} + \alpha_{66}^{(2)} - \beta_{66}^{(1)}\frac{t_1}{2} + \beta_{66}^{(2)}\frac{t_2}{2} + \frac{t_1 + t_2}{2}\beta_{66}^{(2)} + \frac{t_2(t_1 + t_2)}{4}\delta_{66}^{(2)} \tag{2.81}$$

$$Q_{11} = \beta_{11}^{(1)} - \frac{t_1}{2}\delta_{11}^{(1)} + \beta_{11}^{(2)} + \frac{t_2}{2}\delta_{11}^{(2)} \tag{2.82}$$

$$Q_{12} = \beta_{12}^{(1)} - \frac{t_1}{2}\delta_{12}^{(1)} + \beta_{12}^{(2)} + \frac{t_2}{2}\delta_{12}^{(2)} \tag{2.83}$$

$$Q_{16} = \beta_{16}^{(1)} - \frac{t_1}{2}\delta_{16}^{(1)} + \beta_{16}^{(2)} + \frac{t_2}{2}\delta_{16}^{(2)} \tag{2.84}$$

$$Q_{26} = \beta_{26}^{(1)} - \frac{t_1}{2}\delta_{26}^{(1)} + \beta_{26}^{(2)} + \frac{t_2}{2}\delta_{26}^{(2)} \tag{2.85}$$

$$Q_{66} = \beta_{66}^{(1)} - \frac{t_1}{2}\delta_{66}^{(1)} + \beta_{66}^{(2)} + \frac{t_2}{2}\delta_{66}^{(2)} \tag{2.86}$$

To determine the concentrated transverse shear force Q_{xc} a supplementary analysis needs to be solved and analytical solution is presented only for a two-dimensional problem in the reference.

Since in the present study the total SERR has already been found, the problem of finding Q_{xc} is avoided and the mode-I SERR is evaluated as,

$$G_I = G - G_{II} - G_{III} \tag{2.87}$$

2.10 Statistical Characterization of Material Property Data

To account for the effects of uncertainties on the calculated total strain energy release rate and its components, Monte Carlo simulations are to be performed. If a Monte Carlo simulation is performed and the SERR values are found for various double cantilever beam and end-notched flexure models, it is necessary to fit the results to an appropriate distribution and calculate the statistically-based values. The *A*-basis value or *B*-basis value for a statistical distribution is defined as the lower tolerance limit associated with the 95% confidence for the 1st-percentile value or the 10th-percentile value of a specified population. This basis value is calculated for the maximum strain energy release rate and compared with the fracture toughness of the laminate to predict the onset of delamination growth. Section 2.9.1 describes the step-by-step procedure for

performing the Anderson-Darling goodness-of-fit test to fit the strain energy release rate values to a Weibull, normal or log-normal distribution and calculate the corresponding B-basis value for the distribution that best fits the results.

2.10.1 Anderson-Darling Goodness-of-fit Test

Anderson-Darling test can be used to evaluate how well a particular distribution fits the data at hand. It compares the cumulative distribution function of interest with the cumulative distribution function of the data and provides a measure of the fit. The distribution is accepted or rejected based on a 5% significance level. The Composite Materials Handbook (2002) details the step-by-step procedure for performing goodness-of-fit tests for the two-parameter Weibull, normal or log-normal distribution.

2.10.1.1 Goodness-of-fit Test for the Two-parameter Weibull Distribution

First, the maximum likelihood estimates of the shape and scale parameters, $\hat{\beta}$ and $\hat{\alpha}$ of the Weibull distribution are calculated from the equations below.

$$G(\hat{\beta}) = \frac{\sum_{i=1}^{n} x_i^{\hat{\beta}} \ln(x_i)}{\sum_{i=1}^{n} x_i^{\hat{\beta}}} - \frac{1}{\hat{\beta}} - \frac{1}{n}\sum_{i=1}^{n} \ln(x_i) = 0 \tag{2.88}$$

$$\hat{\alpha} = \left(\frac{\sum_{i=1}^{n} x_i^{\hat{\beta}}}{n} \right)^{1/\hat{\beta}} \tag{2.89}$$

Where, x_i is the sample data of size n sorted from the smallest to largest values.

$G(\hat{\beta})$, is solved iteratively for $\hat{\beta}$ assuming an initial estimate of ($1.28/S_y$) and a tolerance for convergence of ($0.000002*S_y$) where S_y is the geometric standard deviation of the sample data. The final $\hat{\beta}$ is substituted in equation (2.89) to obtain the scale parameter estimate $\hat{\alpha}$.

The general form of the Anderson-Darling test statistic is given by,

$$AD = \sum_{i=1}^{n}\left[\frac{1-2i}{n}\left\{\ln[F_0(x_i)] + \ln[1 - F_0(x_{n+1-i})]\right\}\right] - n \tag{2.90}$$

Where, $F_0(x_i)$ is the cumulative distribution function of the distribution considered.

For a two-parameter Weibull distribution,

$$F_0(x_i) = 1 - \exp\left(-\left[\frac{x_i}{\hat{\alpha}}\right]^{\hat{\beta}}\right) \tag{2.91}$$

Let,

$$z_i = [x_i / \hat{\alpha}]^{\hat{\beta}} \tag{2.92}$$

Substituting in equation (2.90) gives

$$AD = \sum_{i=1}^{n}\left[\frac{1-2i}{n}\left\{\ln[1 - \exp(-z_i)] + z_{n+1-i}\right\}\right] - n \tag{2.93}$$

The Observed Significance Level is given by

$$OSL = 1/\left\{1 + \exp[-0.10 + 1.24\ln(AD^*) + 4.48AD^*]\right\} \tag{2.94}$$

With,

$$AD^* = \left(1 + \frac{0.2}{\sqrt{n}}\right)AD \tag{2.95}$$

If $OSL \geq 0.05$ the Weibull distribution is accepted and the *B*-basis value is calculated as

$$B = \hat{q}\exp\left\{\frac{-V_B}{\hat{\beta}\sqrt{n}}\right\} \tag{2.96}$$

Where,

$$\hat{q} = \hat{\alpha}(0.10536)^{1/\hat{\beta}} \tag{2.97}$$

And the numerical approximation of V_B is given by,

$$V_B \approx 3.803 + \exp\left\{1.79 - 0.516\ln(n) + \frac{5.1}{n-1}\right\} \tag{2.98}$$

2.10.1.2 Goodness-of-fit Test for the Normal Distribution

For the normal distribution, the cumulative distribution function is given by

$$F_0(x_i) = \frac{1}{2}\left(1 + erf\left[\frac{x_i - \bar{x}}{s\sqrt{2}}\right]\right) \tag{2.99}$$

Where, $erf(x)$ is the error function defined as

$$erf(x) = \frac{2}{\sqrt{\pi}}\int_0^x e^{-t^2}\,dt \tag{2.100}$$

Let,

$$z_i = \frac{x_i - \bar{x}}{s} \tag{2.101}$$

Where, $\bar{x}$ and s are the mean and standard deviation respectively.

$$AD = \sum_{i=1}^{n}\left[\frac{1-2i}{n}\left\{\ln[F_0(z_i)] + \ln[1 - F_0(z_{n+1-i})]\right\}\right] - n \tag{2.102}$$

The Observed Significance Level is given by

$$OSL = 1/\left\{1 + \exp[-0.48 + 0.78\ln(AD^*) + 4.58AD^*]\right\} \tag{2.103}$$

With,

$$AD^* = \left[1 + \frac{4}{n} - \frac{25}{n^2}\right]AD \tag{2.104}$$

If $OSL \geq 0.05$ the normal distribution is accepted and the *B*-basis value is calculated as

$$B = \bar{x} - k_B s \tag{2.105}$$

And the numerical approximation of k_B is given by

$$k_B \approx 1.282 + \exp(0.958 - 0.520\ln(n) + \frac{3.19}{n}) \tag{2.106}$$

2.10.1.3 Goodness-of-fit Test for the Log-normal Distribution

For the log-normal distribution, the cumulative distribution function is given by

$$F_0(x_i) = \frac{1}{2} + \frac{1}{2}erf\left[\frac{\ln(x_i) - \bar{x}_L}{s_L\sqrt{2}}\right] \tag{2.107}$$

Let,

$$z_i = \frac{\ln(x_i) - \bar{x}_L}{s_L} \tag{2.108}$$

Where, $\bar{x}_L$ and s_L are the mean and standard deviation of $\ln(x_i)$ values.

The calculation of Anderson-Darling test statistic, Observed Significance Level and *B*-basis value are similar to that of the normal distribution case. Finally the basis value is transformed to the original units as the exponent of *B*.

2.10.1.4 Non-parametric B-basis Values

If the number of samples (n>29), the rank for determining the non-parametric basis value is given by

$$r_B = \frac{n}{10} - 1.645\sqrt{\frac{9n}{100}} + 0.23 \tag{2.109}$$

The calculated value is rounded off to the nearest integer towards -∞. The *B*-basis value is the r_B^{th} lowest observation in the data set.

3 FINITE ELEMENT MODELING

3.1 Introduction

One of the methods used for the finite element modeling of delaminated composites is called the two-sublaminate method. This method can be implemented using two approaches.

- The regions above and below the plane of delamination are modeled using separate volumes and meshed with solid elements. Further, this model can have a number of solid or layered solid elements in the thickness direction for improved interlaminar stresses.
- The mid-planes of the two regions are modeled using separate areas and meshed with shell elements.

ANSYS v10.0 finite element software is used for the current work. The following sections review the various options available in ANSYS for implementing the two-sublaminate model. They are arranged in the following order:

- Elements available for modeling the sublaminates.
- Specifying the improved transverse shear stiffness matrix for the chosen element.
- Enforcing displacement compatibility on the elements in the uncracked part, so that they are constrained to rigid body motion.
- Preventing interpenetration of the two sublaminates and accounting for sliding friction effects using surface-to-surface contact elements.

After the deterministic model is created parametrically, probabilistic analysis is performed on the deterministic model by varying the parameters and samples of strain energy release rates are obtained. The ANSYS Probabilistic Design System that is used for performing these operations is introduced in Section 3.2.5. Finally the step-by-step procedure for creating the deterministic model and executing the probabilistic analysis are listed in Section 3.3.

3.2 Modeling Considerations for ANSYS Finite Element Software

3.2.1 Element Type

ANSYS offers two solid and three shell elements to model layered composite structures.

Solid46 – Layered structural solid – It is an 8-noded element that can be used to model layered solids or thick shells with up to 250 uniform thickness layers.

Solid191 – Layered structural solid – It is a 20-noded element that can be used to model layered solids or thick shells with up to 100 uniform thickness layers.

Shell99 – Linear layered structural shell – It can be used to model laminated composites with linear material properties. Up to 250 layers with orthotropic material properties can be specified.

Shell91 – Non-linear layered structural shell – It can be used to model composites with non-linear material properties. It allows only a maximum of 100 layers. But the element formulation time is small compared with Shell99 elements if the number of layers is three or less. It can be used if there are convergence problems with Shell99 elements in a non-linear analysis.

Shell181- Finite strain shell element – It can be used to model laminated composites by defining the lay-up and material properties through the section commands. It can account for thickness variations in large-strain analyses.

As mentioned in section 1.4, Monte Carlo simulations are to be performed, by declaring as many as eight random input variables. To get sufficiently accurate statistical results, 120 to 150 simulation loops may be required. So, a two-sublaminate model using shell elements is the best option, as they are more efficient and can drastically reduce the formulation time. Out of the shell elements available, *Shell181* is very stable, with the least convergence problems of the three. It is well suited for the current analysis since

improved transverse shear stiffness values can be specified by the user using section control commands.

3.2.2 Transverse Shear Stiffness

In most of the literature available, a shear correction factor of 5/6 is assumed. This assumption is not valid for laminated composites and it varies within a large range. The user can implement the exact formulation required to find the shear correction factor for the specific problem at hand (for e.g. the energy equivalence principle) as follows:

ANSYS calculated transverse shear stiffness = kGh
Where,
k – Shear correction factor (5/6)
G – Shear modulus
h – Thickness of the element

Once the transverse shear stiffness values are known, the exact values can be input by the user as,

Exact stiffness value = (user calculated shear correction factor*6/5) * ANSYS calculated Stiffness

This approach is useful only when *Shell91* or *Shell99* elements are used because they include a factor of 1.2 to the stiffness values to avoid shear locking. Since *Shell181* is used for the current analysis, a valid methodology is used to find improved transverse shear stiffness values and input directly using section control commands.

The basic idea behind the methodology is to calculate the transverse shear stresses directly from the transverse shear forces by neglecting the influence of the membrane forces and assuming two cylindrical bending modes (Rolfes and Rohwer 1997). This method has shown good correlation with three dimensional models that used a number of

solid elements in the thickness direction. Shear correction factors are no longer required, since the formulation itself provides improved transverse shear stiffness values. These values are input as real constants R7, R8 and R9 of the *Shell181* element.

3.2.3 Defining the Uncracked Region

After modeling the sublaminates, the uncracked regions of the sublaminates have to be declared to be rigid. Four options are available to define the uncracked region, if the nodes of the upper plate are offset to the bottom face and the nodes of the lower plate are offset to the top face of the element.

Merging coincident nodes – The plates are modeled as areas with an infinitesimal offset above and below the plane of delamination. The areas are then meshed identically with the nodes of the upper plate offset to the bottom of the shell element and nodes of the lower plate offset to the top of the shell element. The nodes in the uncracked region of the two plates are selected. All the nodes within the tolerance limit for coincidence are simply merged together by issuing the *NUMMRG* command. Only the lower numbered or the higher numbered nodes are retained. For example, if the areas are modeled with an offset of say 0.001, then the appropriate command in ANSYS would be "*NUMMRG,NODE,0.0011"*.

Coupling coincident nodes – In this method, the degrees of freedom (DOF) of all the nodes within the tolerance limit for coincidence are coupled. Only the DOF of the lower numbered or higher numbered nodes are calculated and are assigned to the DOF of the coupled node. The same modeling considerations as for *NUMMRG* apply here and coupled nodes are automatically generated by issuing the command *"CPINTF,ALL,0.0011"*.

Constraint equations – Constraint equations are linear equations which relate the DOF of one node to the DOF of another node. According to the plate theory implemented in the shell elements, constraint equations are formulated which enforce displacement

compatibility along the plane of delamination in the uncracked region. Constraint equations can also be automatically generated by selecting the elements in the upper plate and the nodes in the lower plate, both from the uncracked regions, and tying them together by issuing the command *"CEINTF, ,ALL"*.

The main drawback of the above three methods is that they are valid only for small-displacement static analyses.

MPC184 element – *MPC184* element internally generates multi-point constraint equations which define various kinematics between two nodes. The shell elements in the uncracked region can be declared to move rigidly by just overlaying *MPC184* elements along the boundaries of the two plates and there is no need to create *MPC184* elements along the internal boundaries of each element that make up the two plates. This can be done by selecting all the nodes along the boundary of the uncracked region and issuing the command "*EINTF,0.0011, ,LOW"*

Internal MPC algorithm of contact elements – The surface-to-surface contact elements *CONTA173*, *CONTA174* and their target element *TARGE170* incorporate an internal multi-point constraint algorithm to define 'Bonded Initial' or 'Bonded Always' contact condition between the contact and target surfaces. Using the *ESURF* command, the contact elements are created overlaying the shell elements along the boundaries of the two plates in the uncracked region. If the type of contact is defined to be 'Bonded Always' using the contact element's key option, the two plates are constrained throughout the solution phase.

The calculation of strain energy release rate in the near crack tip region requires that mid-plane strains, curvatures and stress resultants be output for each element along the delamination front. Also the evaluation of stresses and strains are better when curved structures are modeled with nodes along the mid-plane of the shell element. So, it would be better if the shell elements are defined with their nodes lying on the mid-plane instead of being offset to the top or bottom surfaces. The main advantage of using the internal multi-point constraint approach of contact elements is that they account for the thickness

of the underlying shell elements and so the nodes can be placed on the mid-surface of the elements. Unlike the use of *MPC184* elements, this modeling method is valid for buckling analyses too. So, out of the latter two methods, the use of the internal multi-point constraint algorithm is better in terms of future work that can be performed along the lines of the current thesis work, like modeling curved structures and also studying buckling behavior of delaminated composites.

3.2.4 Sliding Friction and Prevention of Layer Interpenetration

Friction effects between the two sublaminates in the cracked region cannot be neglected for mode-II and mode-III loadings since the friction coefficient can range from 0.4-0.8 for some laminated composites depending on the material properties and the nature of damage. Layer interpenetration must also be prevented in the cracked region to accurately predict the strain energy release rates. Both these issues are overcome by using surface-to-surface contact elements in the delaminated region which prevent layer interpenetration as well as account for sliding friction effects. Figure 3.1 shows contact and target elements which use the internal multi-point constraint approach in the uncracked region and those that use the augmented Lagrange algorithm in the delaminated region.

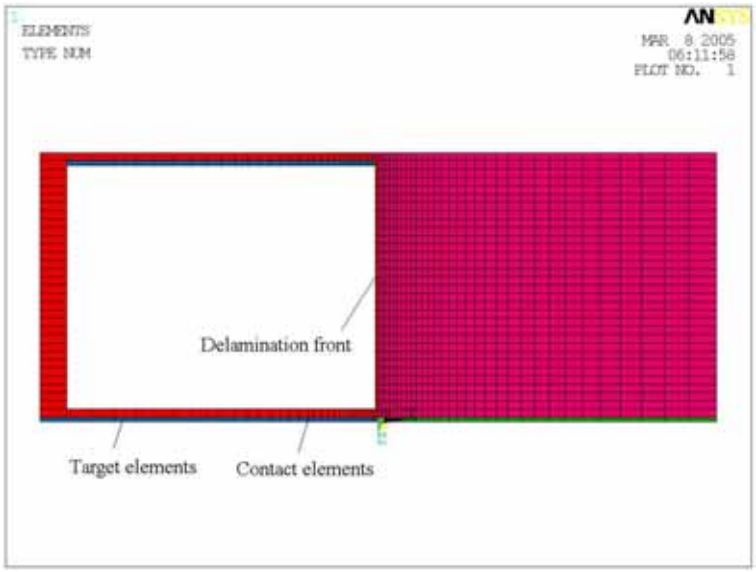

Figure 3.1 Element plot showing the contact and target elements

3.2.5 Probabilistic Design

Even after incorporating all the above mentioned improvements, it can be seen that there are a few input parameters like friction coefficient between crack faces, which do not have definite values and that they vary within a large range. Since first-order shear deformation theory inherently has several simplifying assumptions, making further assumptions on these variables would make the results less meaningful. So the best option would be to use the ANSYS Probabilistic Design System (PDS) for assessing the effect of uncertain input parameters and assumptions on the current model.

3.2.5.1 Terminology

Random Input Variables (RVs) – The parameters in the computer model that exhibit uncertainty and are subjected to scatter in reality cannot be assigned deterministic values. This would make the validity of the results depend totally on the accuracy of these parameters for the component under real life conditions. In probabilistic design such variables are specified by the type of statistical distribution that they follow and the parameter values of their distribution functions. These are called the RVs.

Random Output Parameters (RPs) – The results of the finite element analysis which change with changes in the values of the RVs are called the RPs and are typically functions of the RVs.

Sample – A unique set of values selected from within the distribution functions of the RVs and the values of the resulting RPs that represents a particular model configuration is called a sample.

Simulation Loop – A single pass through the analysis file in which the probabilistic analysis uses the RVs from one sample and collects the values of the RPs after the run.

Simulation – The collection of all the samples at the end of the required number of simulation loops.

3.2.5.2 ANSYS Probabilistic Design System

ANSYS Probabilistic Design System offers two primary techniques to employ probabilistic analysis. They are the Monte Carlo simulation and the Response Surface method.

With Monte Carlo simulation, a large number of individual simulation loops are performed which do not depend on the results of any other simulation loop. The number of loops is determined by whether the samples are statistically representative of the real-life conditions and whether sufficient correlation between the RVs and the RPs has been reached. Direct sampling and Latin hypercube sampling are the two methods by which RVs can be chosen for each simulation loop. The drawback of the direct sampling method is the possibility that same or almost same samples may be repeated since the process has no memory. Latin hypercube sampling differs from direct sampling in that it has memory and so avoids repeating samples that have been evaluated earlier. It also gives more weightage to the tail regions of the distributions of the RVs which is important for accurately assessing the reliability of delaminated composites.

Response Surface method can be used if the influence of the RVs on the RPs can be approximated by mathematical functions, usually a quadratic polynomial. First, simulation loops are run to calculate the RPs corresponding to the sample points in the space of the RVs. Then a regression analysis is performed to derive the terms and coefficients of the approximation function in terms of the sampling point results. This method requires that the RPs be smooth functions of the RVs.

Since contact and friction are taken into account in the present study, sudden jumps in the output parameters are possible. So, Monte Carlo simulation technique is used which is valid irrespective of the physical effects being modeled. The random input variables (RVs) chosen are:

1. Longitudinal modulus, E11
2. Transverse modulus, E22
3. In-plane shear modulus, G12
4. Transverse shear modulus, G13 and G23

5. Coefficient of friction between the delaminated faces, FC
6. Mesh refinement, MRV
7. Virtual crack extension length, VCCL
8. Ply thickness, TPLY
9. Fiber misalignment, THETA

The significant parameters that are varied are

1. Laminate width, LAMWID
2. Delamination length, DELAMLEN
3. Loading, FZPDS

3.3 Modeling Procedure

3.3.1 Deterministic Model

Before executing the probabilistic run, an ANSYS input file is created containing the necessary commands for developing a deterministic model parametrically, applying loads, solving the problem, processing the results and storing them in parameters. The input file also contains commands to import all the laminate stiffness matrices, shear correction factors and the matrices required for calculating the improved transverse shear stresses and strains, which are output to a text file by MATLAB software. This eliminates the need for calculating the matrices during each run.

Step 1:

Four areas are created at the mid-planes of the upper and lower plates. In the figure below, areas *A1* and *A3* represent the uncracked region of upper plate while *A2* and *A4* represent the cracked region of upper plate.

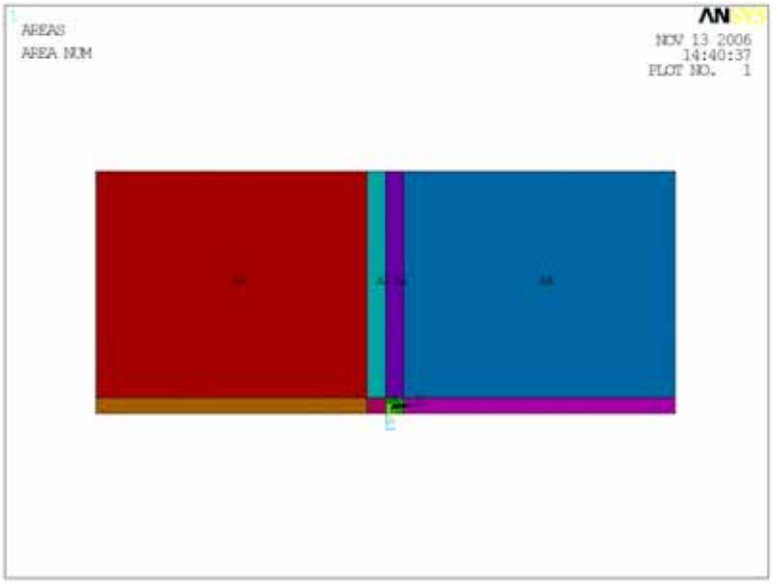

Figure 3.2 (a) Front view of the areas

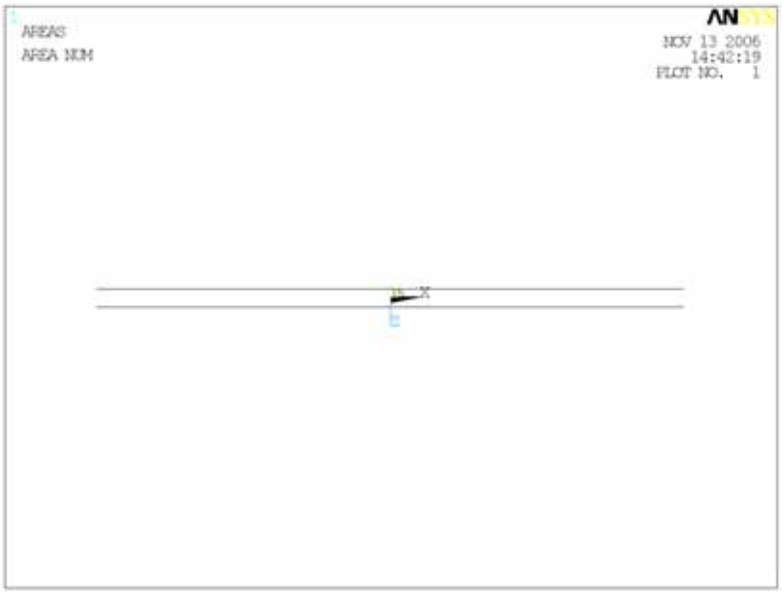

Figure 3.2 (b) Top view of the areas

Figure 3.2 Areas generated at mid-planes of the upper and lower plates

Step 2:

The number of element divisions and spacing ratio for the lines are specified using the *LESIZE* command. A spacing ratio of 1.0 (uniform spacing) for the lines parallel to the y-axis, a spacing ratio less than 1.0 (size decreases) for the uncracked region and a spacing ratio greater than 1.0 (size increases) for the cracked region are specified to obtain a

refined mesh around the delamination front. The number of element divisions for the lines constituting areas around the crack is the mesh refinement value which is declared as a random input variable for the probabilistic run.

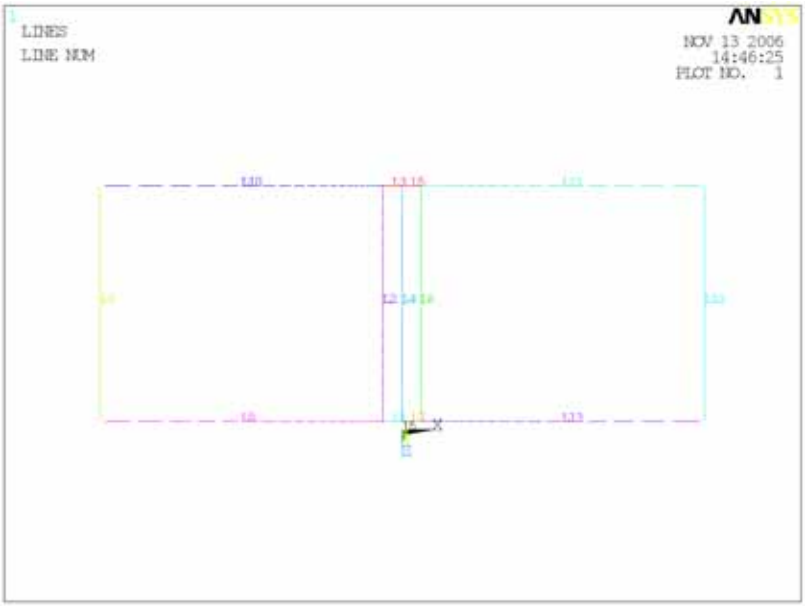

Figure 3.3 Line plot showing the mesh size

Step 3:

The areas are meshed with quadrilateral *SHELL181* elements using the mapped meshing technique.

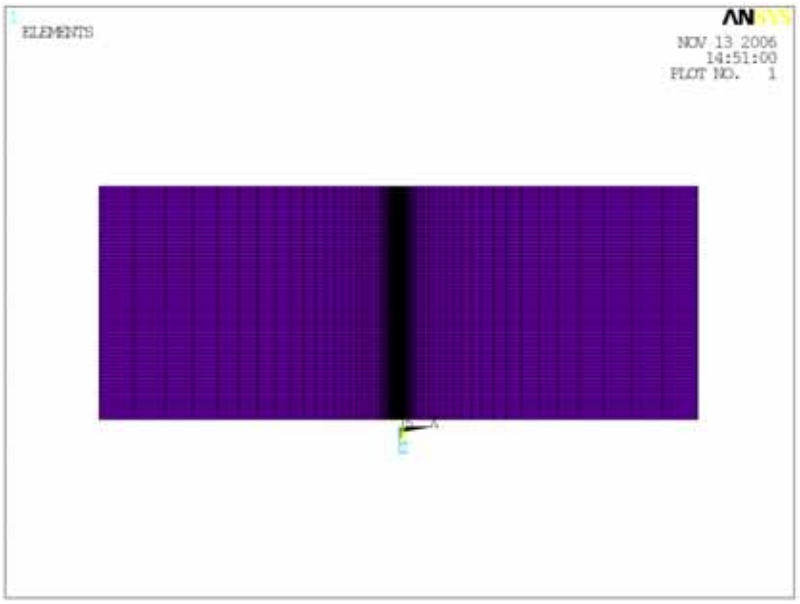

Figure 3.4 Element plot of the upper plate

Step 4:

The elements along the boundaries of the uncracked region and then the nodes attached to these elements are selected.

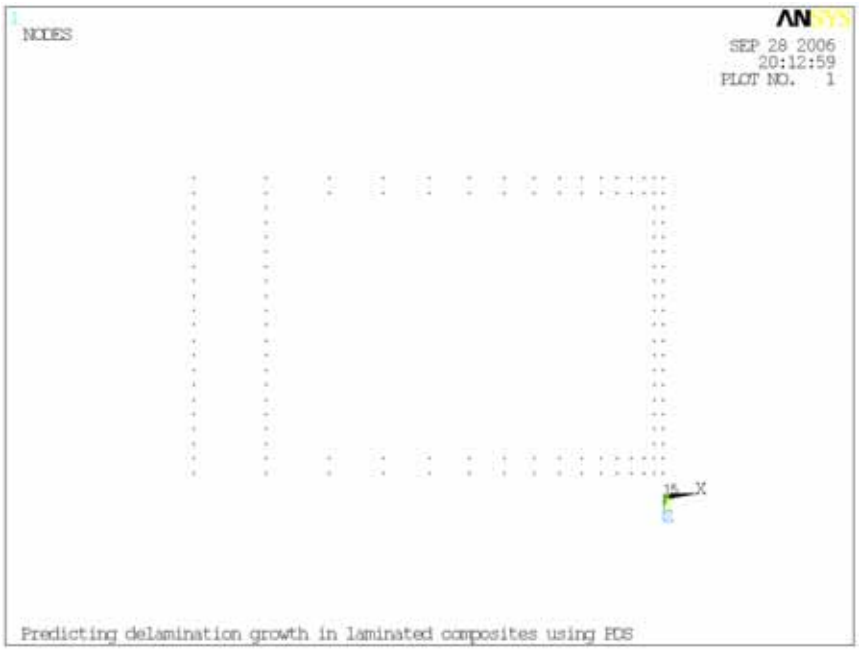

Figure 3.5 Nodes selected along the boundary of the uncracked region

Step 5:

The shell elements which lie along the boundary of the uncracked region in the upper plate are overlaid with contact elements and those in the lower plate with target elements by meshing the nodes selected in the previous step using the *ESURF* command.

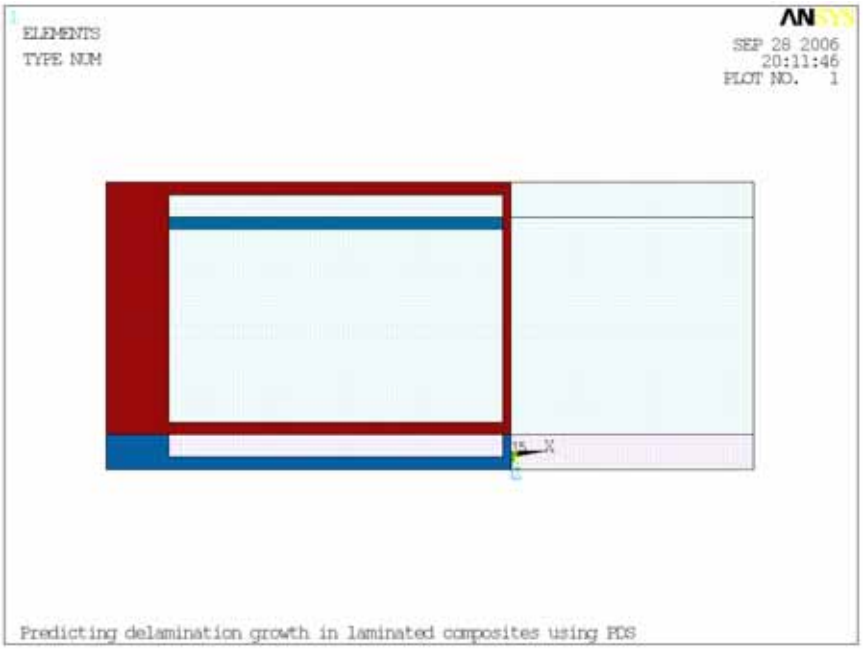

Figure 3.6 Translucent model showing contact and target elements

Similarly, all nodes are selected from the cracked region and meshed with contact and target elements.

Step 6:

After applying loads, solving the problem and reading in the results, the required post-processing is done to calculate the mixed-mode strain energy release rates and all random output variables are stored in parameters.

Step 7:

The strain energy release rate distributions along the delamination front which have to be post-processed using MATLAB are appended to a text file at the end of every simulation loop.

Step 8:

The commands that perform the above operations are saved to a text file.

3.3.2 Probabilistic Analysis

The step-by-step procedure for executing the probabilistic analysis in the ANSYS Probabilistic Design System, discussed in 3.2.5.2, is listed below.

Step 1:

In the ANSYS PDS pre-processor, the input file containing the deterministic model is declared as the PDS analysis file.

Step 2:

The random input variables are declared and their statistical distributions defined.

Step 3:

Any correlations between the random variables are defined.

Step 4:

The random output parameters are specified.

Step 6:

After choosing the probabilistic design method and the sampling method, settings corresponding to the chosen method like location of samples within intervals, number of simulation loops, repetition cycles, auto-stop criteria and random number generation method are set. The required number of simulation loops is executed.

Step 8:

The statistics and trends of the random variables are plotted using the commands available in the PDS post-processor. An HTML report containing all the statistics is also generated.

4 VERIFICATION

4.1 Total Strain Energy Release Rate Verification

Double cantilever beam models of delaminated composite plates are analyzed to verify the total energy release rates calculated using the present plate closure technique based on first-order shear deformation theory. For this preliminary investigation, the specimens chosen from the literature are unidirectional and multidirectional laminated composite plates with isotropic and orthotropic material properties with a single mid-plane delamination.

4.1.1 Isotropic and Orthotropic Double Cantilever Beam Models with Unidirectional Lay-up

Figure 4.1 shows the geometry and the boundary conditions of a double cantilever beam specimen.

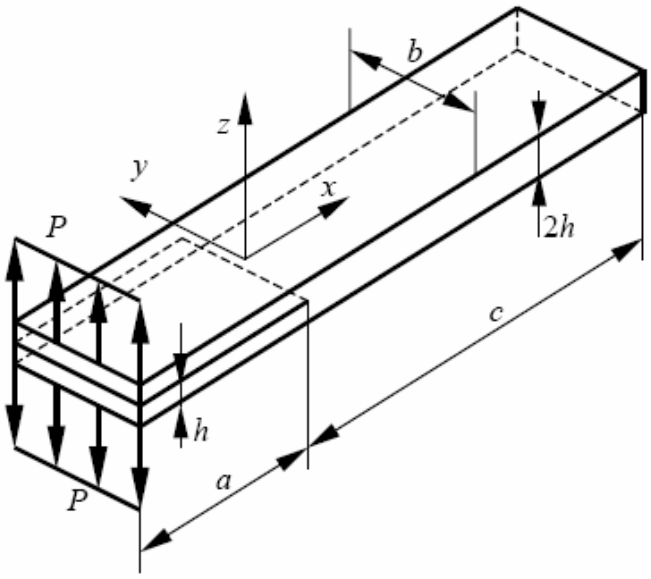

Figure 4.1 Double cantilever beam test [Szekrényes (2005)]

The size and material properties for the isotropic double cantilever beam model,

given in Table 4.1, are taken from Zou, Reid, Li and Soden (2002). Since a two-sublaminate model is used in the reference, a direct quantitative comparison is possible.

Table 4.1 Properties of isotropic double cantilever beam model

a = 50.8 mm	c = 50.8 mm	b = 25.4 mm	h = 1.65 mm
E = 3.4 GPa	G = 1.3 GPa	v = 0.3	P = 1.0 N m^{-1}

The finite element model consists of 50 elements along the delamination front and 50 elements each in the cracked and uncracked regions along the length direction. A spacing ratio of 0.05 is used to obtain a refined mesh around the delamination front. When surface-to-surface contact elements based on the internal multi-point constraint algorithm are used to enforce displacement compatibility in the uncracked region, degrees of freedom have to be constrained only for the target nodes to specify necessary boundary conditions. If the degrees of freedom for the contact nodes are specified, then it would result in over-constraining of the system. So, to specify that the end of the uncracked region is fixed, all degrees of freedom for the target elements' nodes that lie on the mid-plane of the lower plate at the uncracked end are constrained. There are 51 nodes at the ends of the sublaminate arms in the cracked region. A force of 4.98×10^{-4} N is applied in the positive z-direction on all nodes at the delaminated end of the upper plate and in the negative z-direction for the lower plate. Thus the total load is equal to P = 1.0 N m^{-1}.

The average energy release rate along the delamination front is 20.16×10^{-4} J m^{-2} for the present method as against the 20.15×10^{-4} J m^{-2} obtained by Zou, Reid, Li and Soden (2002) and the 20.2×10^{-4} J m^{-2} obtained by Crews, Shivakumar, and Raju (1989) using a three dimensional finite element model and virtual crack closure technique. Figure 4.2 shows the total strain energy release rate, G, plotted against the normalized width of the plate. Each data point in the graph corresponds to the SERR evaluated at the centroidal y-location of the crack-tip elements along the front.

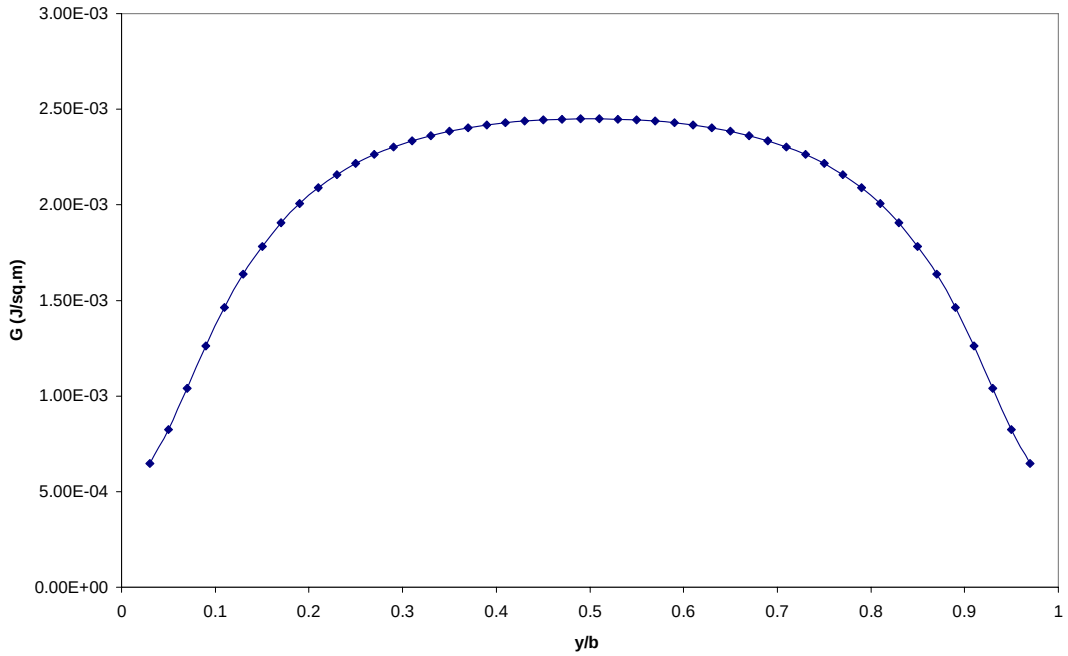

Figure 4.2 Total SERR distribution for the isotropic double cantilever beam model under opening load

The next model analyzed is an orthotropic double cantilever beam model with unidirectional lay-up. The geometry and material properties are shown in Table 4.2. These values are taken from Krueger (1994).

Table 4.2 Properties of orthotropic double cantilever beam model

a = 111.5 mm c = 138.5 mm b = 25 mm h = 1.5 mm
E_1 = 139400 N/mm^2 G_{12} = 4600 N/mm^2 ν_{21} = 0.3
E_2 = 10160 N/mm^2 G_{13} = 4600 N/mm^2 ν_{23} = 0.436
E_3 = 10160 N/mm^2
Ply thickness t = 0.125 mm Lay-up: $[0]_{24}$ P = 12.66 N/mm

The finite element model consists of only one shell element along the thickness direction to model the twelve plies in the upper and lower plates. The mesh density is

32x40 for each of the cracked and uncracked regions. The boundary conditions are applied in the same manner as for the isotropic double cantilever beam model and the load on each node at the ends of the two arms is 9.59 N.

Krueger (1994), has normalized the SERR values using the reference opening mode component $G_{I,b}$ obtained using beam theory as follows

$$\tilde{G}_I = \frac{G_I}{G_{I,b}} \quad with \quad G_{I,b} = \frac{12\, a^2\, P^2}{b^2\, h^3\, E_1} \tag{4.1}$$

Figure 4.3 shows the normalized G values plotted against the normalized width of the plate. It can be seen that there is an excellent correlation between values obtained using the present method and three dimensional nonlinear finite element analysis (Krueger 1994) in all the regions except for 5% of the plate width near the free edges. This is due to the inadequacy of the shell elements to accurately capture the three-dimensional nature of the stress state at the edges. Also in the reference (Krueger 1994), the mesh is highly refined near the free edges compared to the constant element length used in the present model.

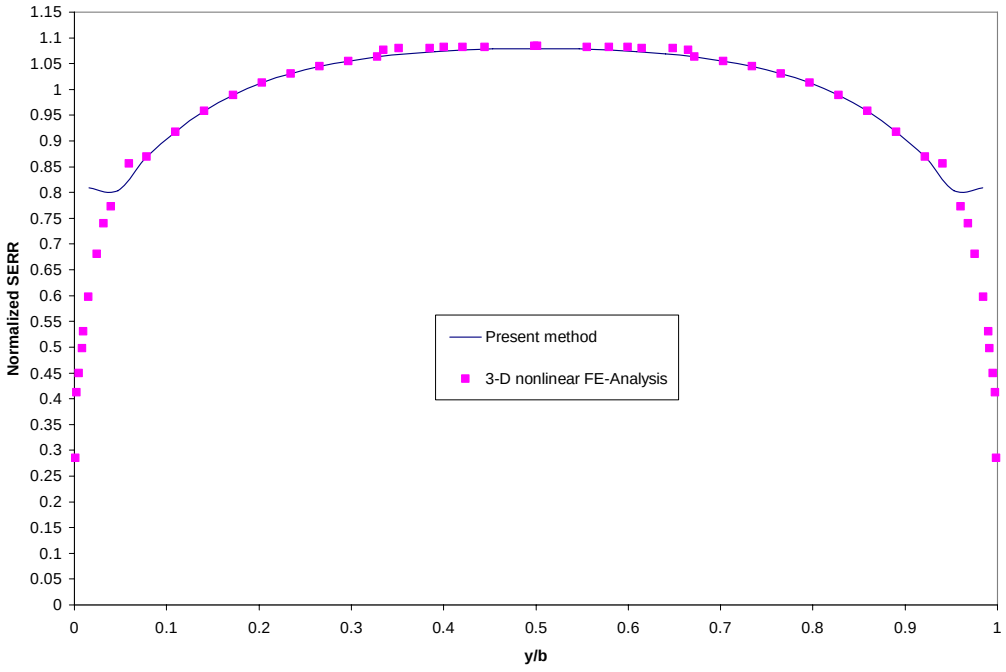

Figure 4.3 Normalized SERR distribution for the orthotropic double cantilever beam model under opening load

4.1.2 Symmetric Double Cantilever Beam Models

The next set of analyses is performed on orthotropic double cantilever beam models with multidirectional lay-up. The models chosen are symmetric with a mid-plane delamination. The geometry, material properties and loads are shown in Table 4.3. These values are taken from Davidson, Yu, and Hu (2000).

The mesh is similar to the one in the reference with the length of the crack tip elements being 1 mm and width being 8 mm with 50 elements along the delamination front. So there are a total of 51 nodes along the ends of each delaminated arm. The load, which is a moment of 100 N, is applied equally on all the nodes as a moment of 784.3137 N-mm in the *y*-direction for the upper plate and -784.3137 N-mm for the lower plate. The comparison of the total strain energy release rates plotted against the normalized width of the plate is shown in Figures 4.4-4.6.

Table 4.3 Properties of symmetric double cantilever beam model

a = 256 mm	c = 256 mm	b = 400 mm	h = 16 mm
E_1 = 1 N/mm^2	G_{12} = 0.5 N/mm^2	ν_{12} = 0.3	
E_2 = 0.1 N/mm^2	G_{13} = 0.5 N/mm^2	ν_{13} = 0.3	
E_3 = 0.1 N/mm^2	G_{23} = 0.5 N/mm^2	ν_{23} = 0.3	
Ply thickness t = 4 mm	Lay-ups: $[90/-45/45/0]_s$		M_y^1 = 100 N
		$[0/90/90/0]_s$	M_y^2 = -100 N
		30° Orthotropic	

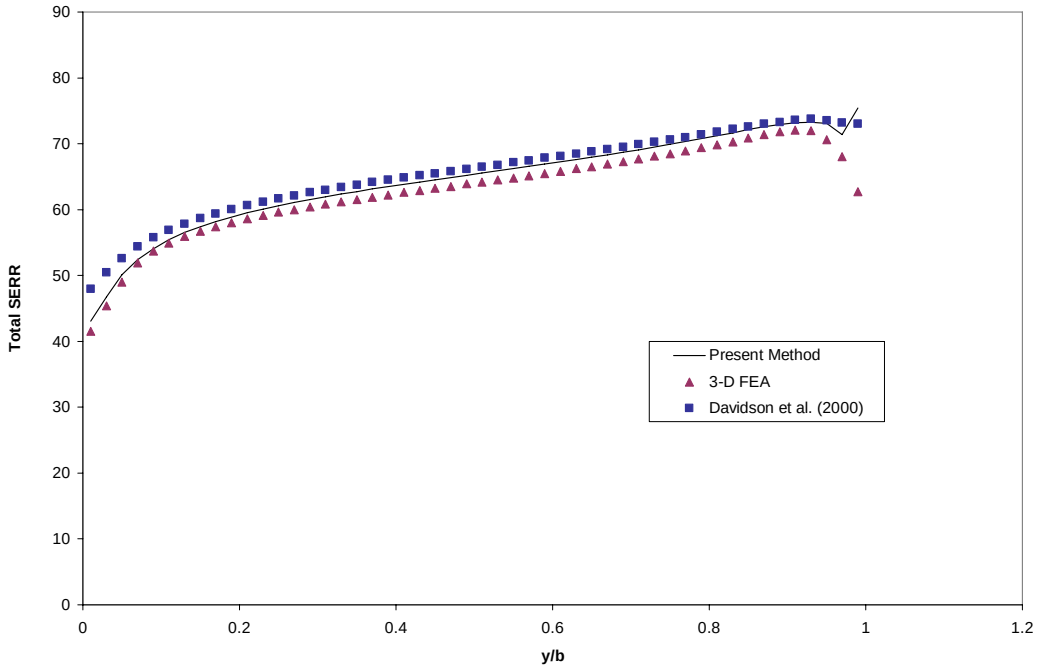

Figure 4.4 Total SERR distribution for the $[90/-45/45/0]_s$ model under opening load

It can be seen that there is an excellent correlation between values obtained using the present method and reference values obtained using three dimensional finite elements and three dimensional crack-tip element method for all the three lay-ups considered.

It should be noted that for these cases, an opening load produces only pure mode-I component of the SERR. So, the mode decomposition is simultaneously verified. The mode-II and mode-III components are correctly predicted to be zero for all the cases.

For the 30° orthotropic case, Figure 4.6 shows the mode-I component which is normalized using the SERR as predicted by the classical plate theory,

$$G_I^{CPT} = \frac{1}{2} M^2 (\delta_{11}^1 + \delta_{11}^2) \tag{4.2}$$

Where, M is the applied load, and $[\delta]$ is the bending compliance with the superscripts 1 and 2 representing the upper and lower laminates.

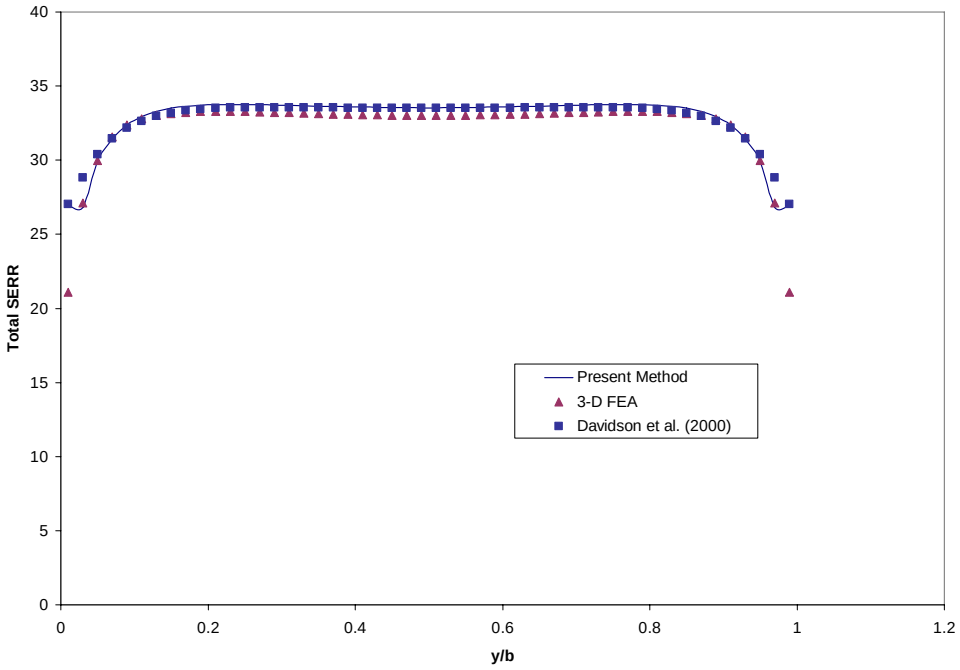

Figure 4.5 Total SERR distribution for the $[0/90/90/0]_s$ model under opening load

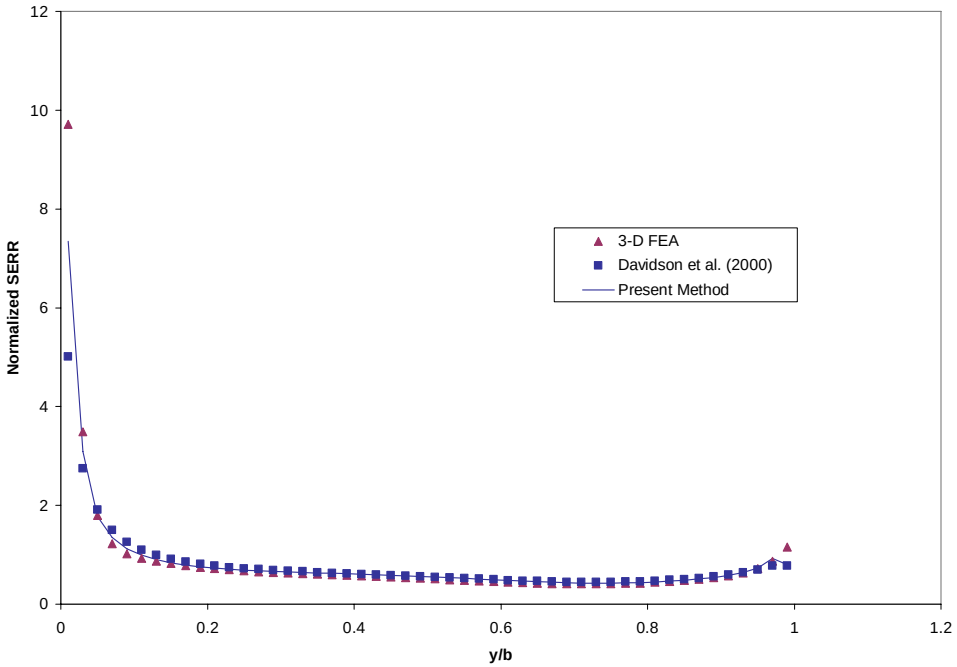

Figure 4.6 Normalized SERR distribution for the 30° orthotropic model under opening load

4.2 Mode Decomposition Verification

Double cantilever beam tests are performed on laminated composite plate models that produce mixed-mode energy release rates. The mode-II and mode-III components are calculated using the formulation given by Wang and Qiao (2004b). The mode-I component is evaluated as the difference between the total SERR, which has already been verified, and the sum of the mode-II and mode-III components.

First an isotropic double cantilever beam model with the material properties, geometry and loading given in the Table 4.4 is considered.

Table 4.4 Properties of isotropic double cantilever beam model under mode-II loading

a = 256 mm c = 256 mm b = 400 mm h = 16 mm
E = 80,000 N/mm^2 υ = 0.3
Ply thickness: t = 4 mm Loading: N_x^1 = 6.25 N/mm
N_x^2 = -6.25 N/mm

The mesh contains 50 elements along the delamination front. The in-plane shearing load of 6.25 N/mm is applied as a uniform load of $F_x^1 = -F_x^2 = 49.02$ N on all the 51 nodes along the end of the delaminated arms. This loading produces both mode-II and mode-III SERR which are normalized using the G_{II} value predicted by a two dimensional analysis under plane strain assumption and based on classical plate theory.

$$G_{II}^{CPT} = \frac{1}{2}N^2\left[\alpha_{11}^1 + \alpha_{11}^2 - \frac{(h_1+h_2)^2}{4}\delta_{11}^u\right] \tag{4.3}$$

In equation (4.3), N = 6.25 N/mm and $[\alpha]$, $[\delta]$ are the extension and bending compliance matrices with the superscripts 1, 2, and u representing the upper, lower and uncracked laminates respectively.

Figures 4.7 and 4.8 show the comparison between the values obtained using the present method and those obtained by Bruno, Greco, and Lonetti (2003) with a two-sublaminate model. It can be seen that there is excellent correlation between the predicted mode-II values, which is the predominant mode, along the entire delamination front and the mode-III values show good correlation only in the central 40% width of the specimen.

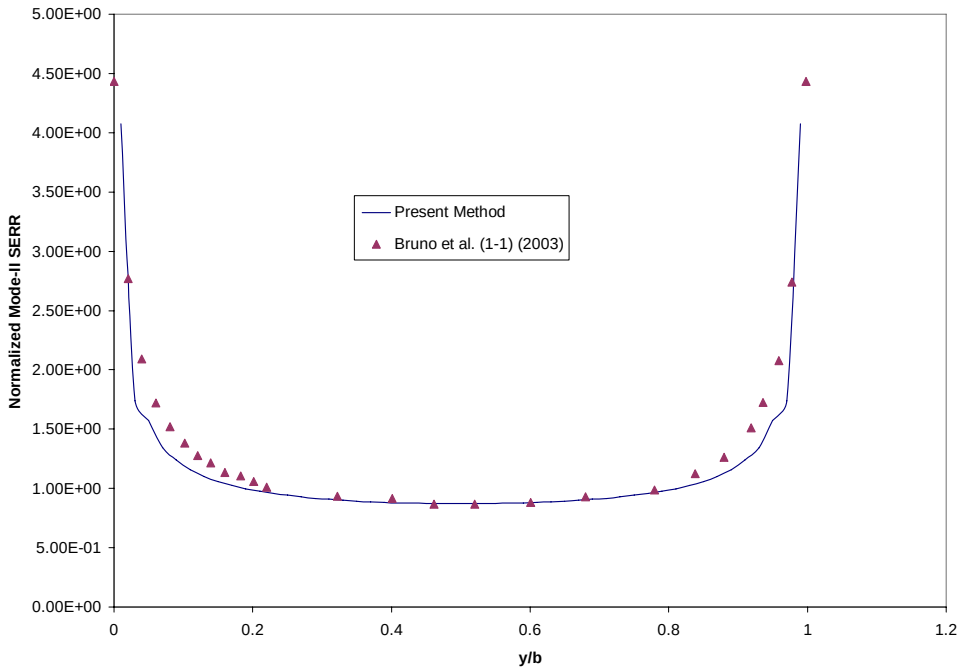

Figure 4.7 Normalized mode-II SERR distribution for isotropic double cantilever beam model under in-plane shearing load

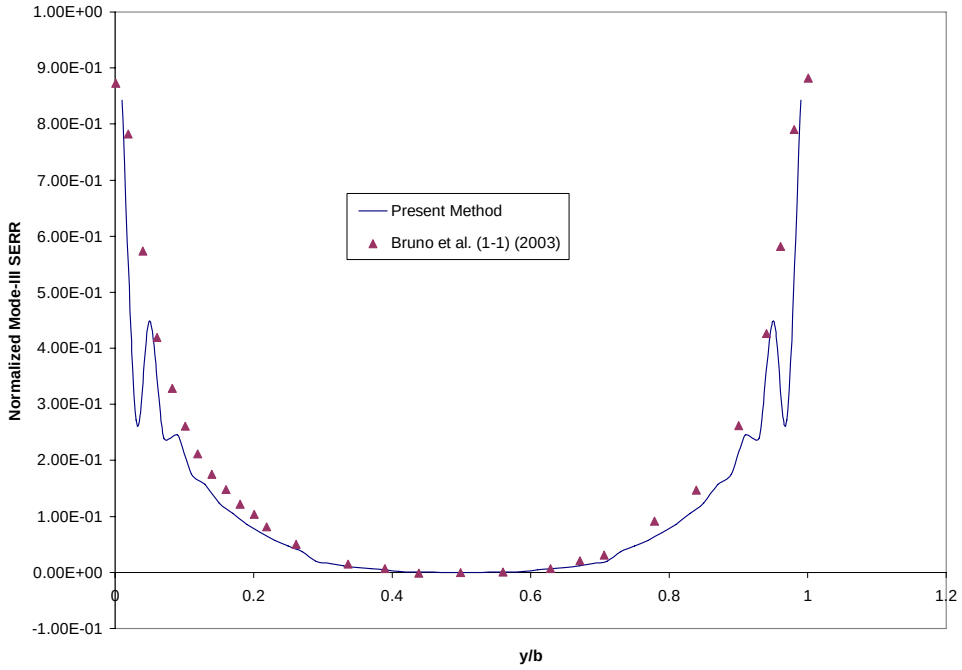

Figure 4.8 Normalized mode-III SERR distribution for isotropic double cantilever beam model under in-plane shearing load

Next, three orthotropic models with $[0/45_3/d/45/0]$, $[0/90_2/0/d/0_2]$ and $[45/0/45_2/d/0/45]$ lay-ups are analyzed. The first two lay-ups are chosen from Davidson (2001) and have an offset delamination between plies of same orientation and the third is chosen from Yu and Davidson (2001) which has an offset delamination between plies of different orientation. The loading and geometry are the same as in Table (4.3) with $h_1 = 8$ mm and $h_2 = 16$ mm. The opening load produces both G_I and G_{II} with G_{III} being negligible.

Figures 4.9-4.11 show the comparison of G, G_I and G_{II} for the $[0/45_3/d/45/0]$ laminate with those obtained by three dimensional finite element analysis. It can be seen that the total energy release rate G is almost identical for both the methods. The difference in the G_I and G_{II} values can be attributed to the different mode-mix values predicted by local approach of the three dimensional finite elements and global approach of the present method. This is because the three dimensional finite element analysis assumes the presence of singular stress and strain fields in the near-tip region while the present method based on laminate theory eliminates the singularity and thus predicts a different mode-mix value. The normalized G_I and G_{II} plots for the $[0/90_2/0/d/0_2]$ laminate

in Figure 4.12 follow the same trend.

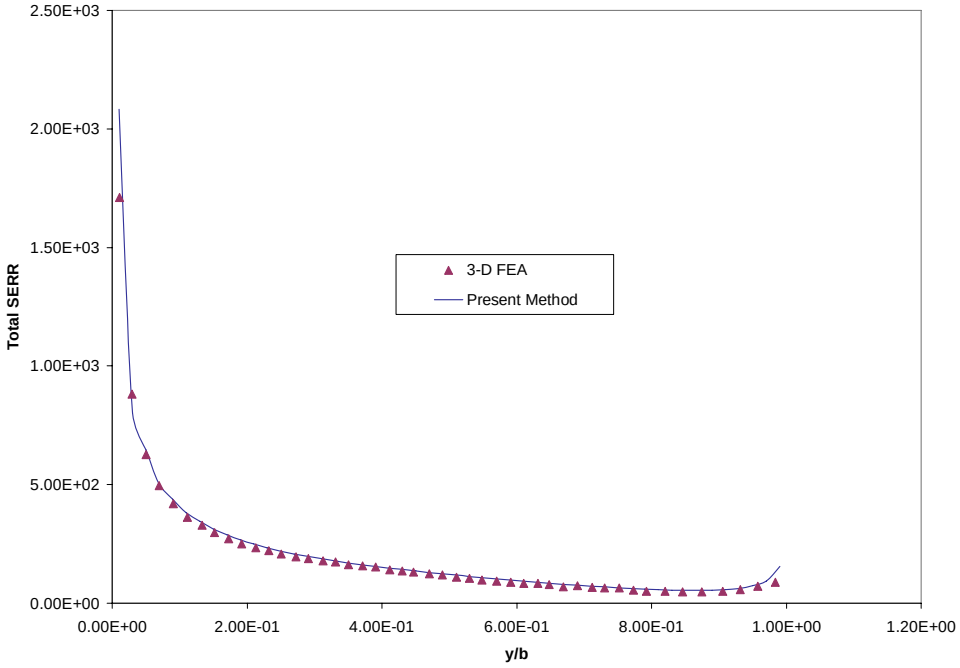

Figure 4.9 Total SERR distribution for the [0/45$_3$/d/45/0] model under opening load

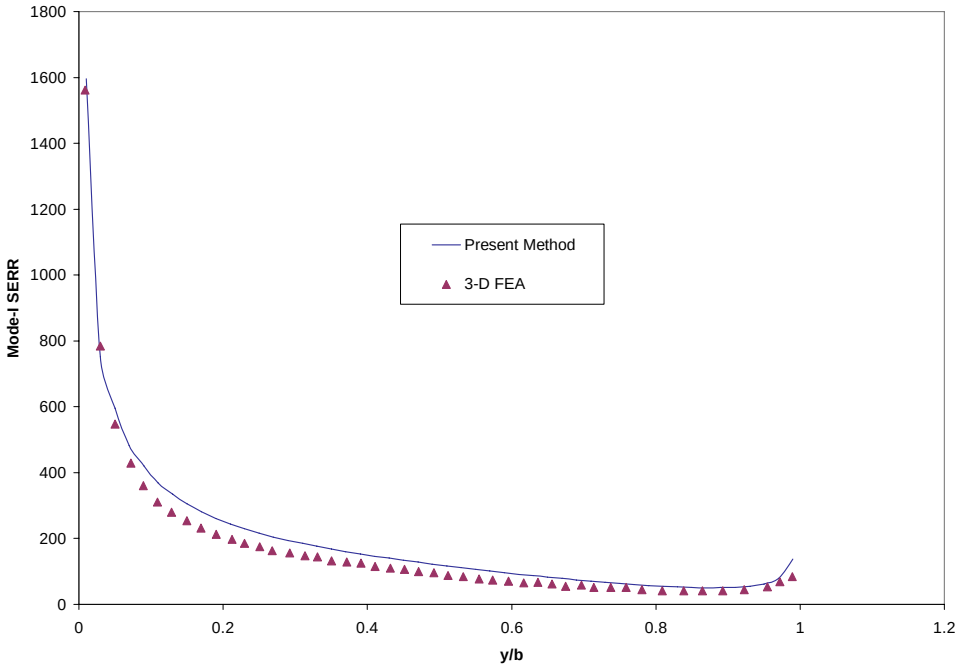

Figure 4.10 Mode-I SERR distribution for the [0/45$_3$/d/45/0] model under opening load

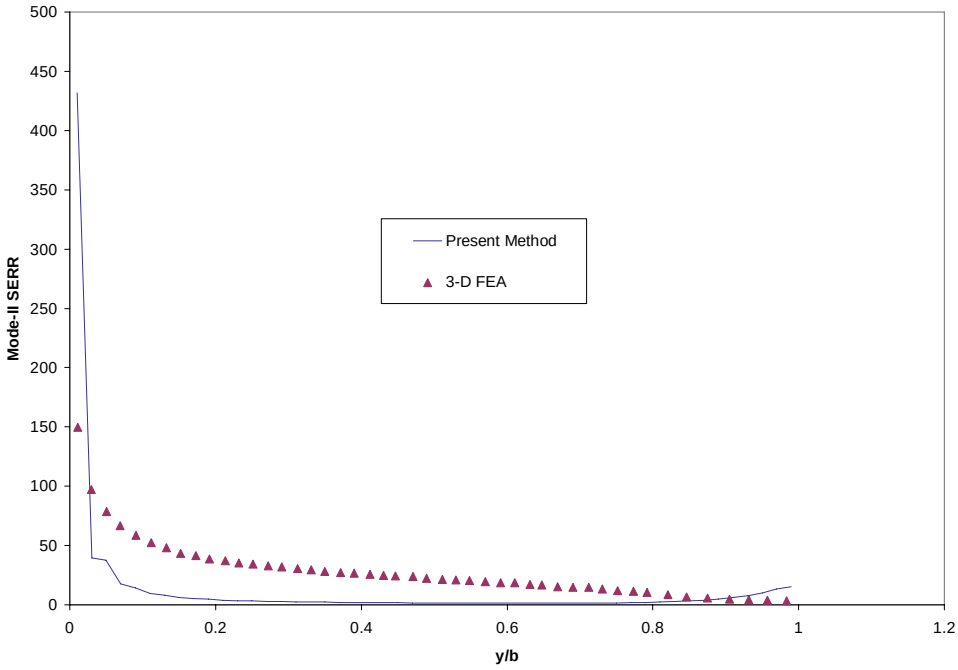

Figure 4.11 Mode-II SERR distribution for the [0/45$_3$/d/45/0] model under opening load

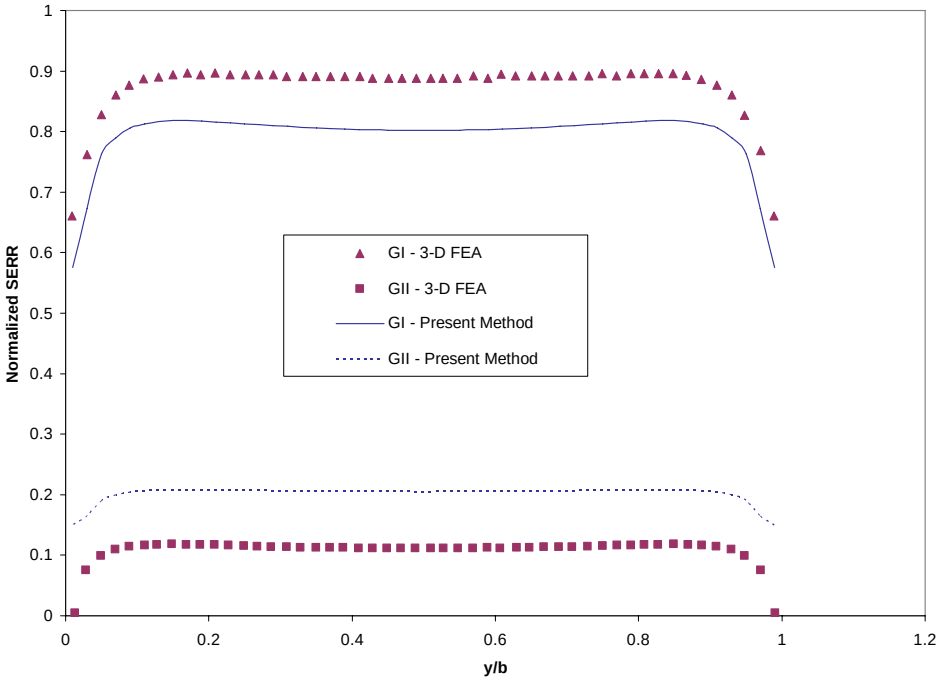

Figure 4.12 Normalized SERR distribution for the [0/90$_2$/0/d/0$_2$] model under opening load

For the third laminate considered, [45/0/-45$_2$/d/0/45], the mode-I and mode-II strain energy release rate distributions in Figures 4.13 and 4.14 confirm this.

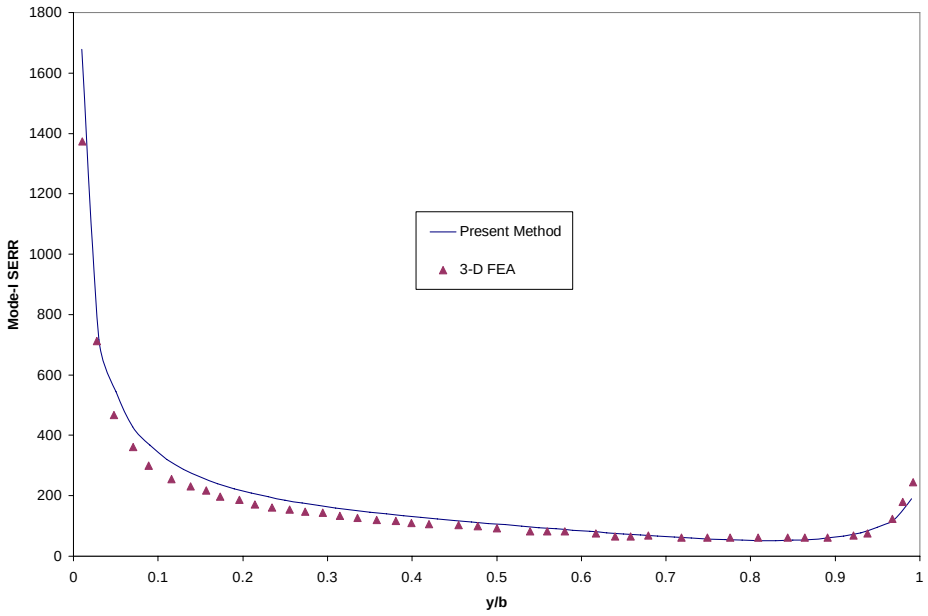

Figure 4.13 Mode-I SERR distribution for the [45/0/-45$_2$/d/0/45] model under opening load

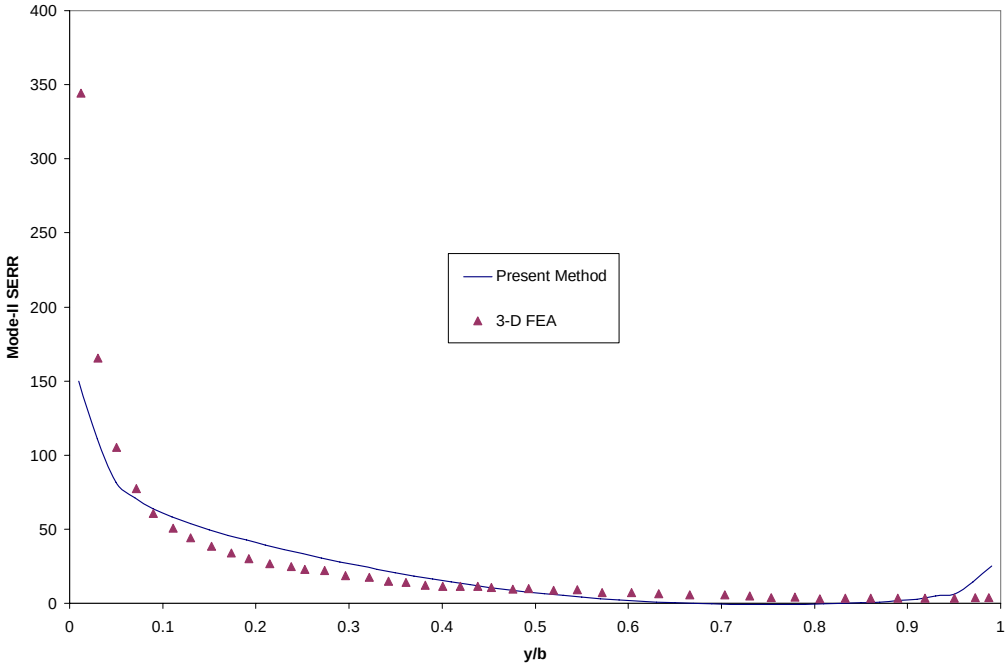

Figure 4.14 Mode-II SERR distribution for the [45/0/-45$_2$/d/0/45] model under opening load

4.3 Sliding Friction and Layer Interpenetration

To verify the present method for calculating the friction energy dissipation and to demonstrate the need for using contact elements to prevent layer interpenetration the end-notched flexure model is considered. The setup is as shown in Figure 4.11 and the geometry and material properties are given in Table 4.5. In the finite element model, the left end is fixed and the displacement in the transverse direction is constrained at the right end of the lower plate. Instead of applying a uniform load at the center of the plate, a displacement of 5 mm is applied in the *z*-direction on all the nodes that lie at the center of the laminate in the length direction. The boundary conditions are shown in Figure 4.16.

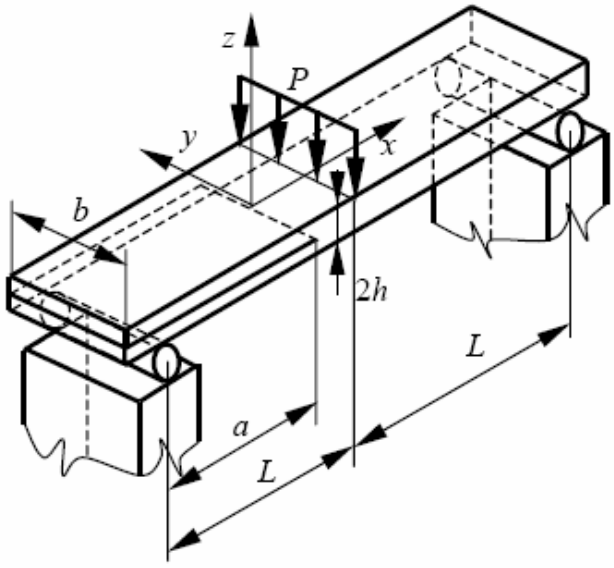

Figure 4.15 End-notched flexure test [Szekrényes (2005)]

Table 4.5 Properties of end-notched flexure model

a = 25 mm	$2L$ = 100 mm	b = 25 mm	h = 1.6 mm	t = 0.4 mm
E_1 = 146860 N/mm^2	G_{12} = 5450 N/mm^2	ν_{12} = 0.33		
E_2 = 10620 N/mm^2	G_{13} = 5450 N/mm^2	ν_{13} = 0.33		
E_3 = 10620 N/mm^2	G_{23} = 3990 N/mm^2	ν_{23} = 0.33		
Loading: U_Z = 5 mm	Lay-ups: [90/-45/45/0/d/0/45/-45/90]			
	[0/45/-45/-45/d/45/0]			

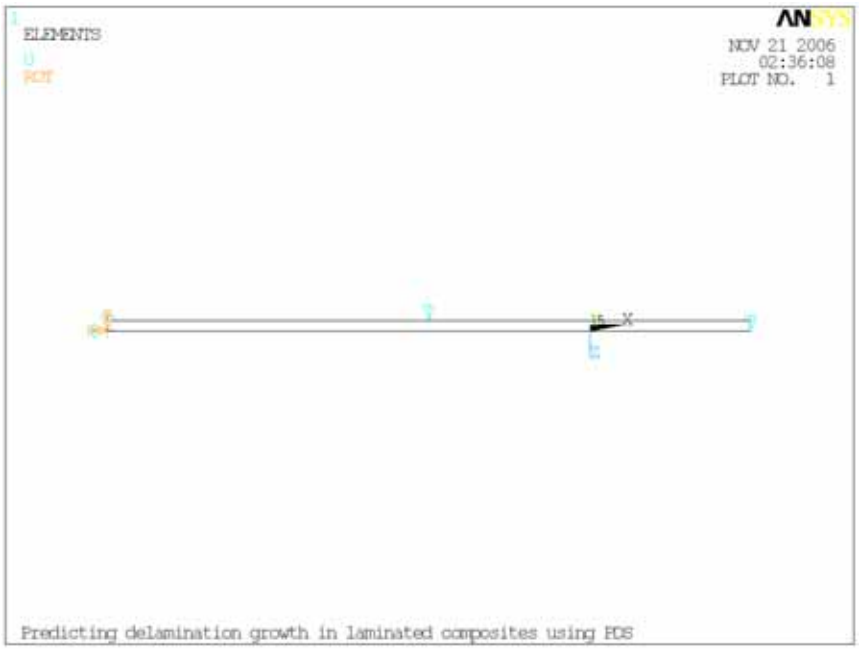

Figure 4.16 Boundary conditions for the end-notched flexure model

Since there are no constraints for the upper sub-laminate it can be seen from Figure 4.17 that it penetrates the lower arm completely, which is physically inadmissible.

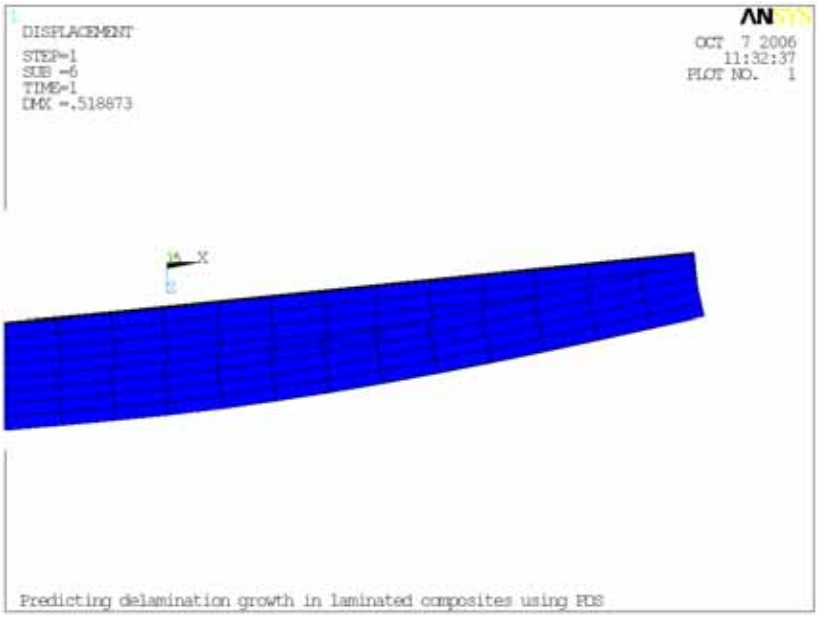

Figure 4.17 Element plot: Interpenetration of delaminated arms

When contact elements are used in the cracked region, the displacement profile shows that there is only an infinitesimal amount of penetration. This depends on the contact algorithm, normal penalty stiffness, penetration tolerance, and other contact element properties and key options specified.

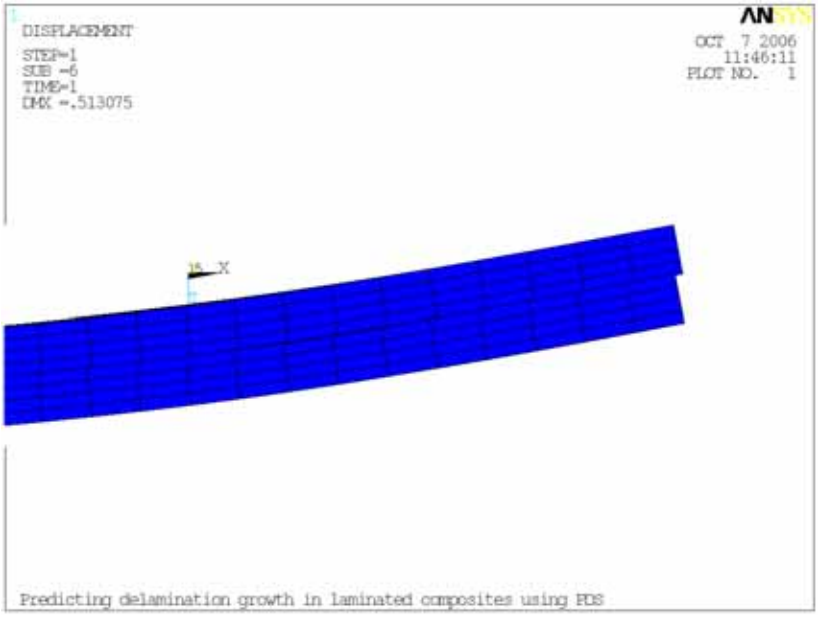

Figure 4.18 Element plot: No interpenetration of delaminated arms

The verification for friction energy dissipation is done by solving the end-notched flexure model twice for both the lay-ups, once with frictionless contact and once with a friction coefficient of μ = 0.5. First, the total potential energy of all the elements is calculated directly from the element output as the sum of potential energy of the individual elements, stored in an element table using the *ETABLE* command in ANSYS and then summing the results in the table using the *SSUM* command. The change in potential energy between the two cases, $\Delta\Pi$ is found. Similarly the energy lost to friction, W^f and strain energy locked up in the contact elements due to layer interpenetration, W^p are calculated by summing the results of the individual contact elements. Since the delamination length is constant, the strain energy release rate, ΔU is zero. Finally the change in potential energy is calculated using Equation 2.59. Table 4.6 lists the change in potential energies calculated from direct element output and using Equation 2.59 for both the lay-ups considered.

Table 4.6 Verification of friction energy dissipation

Laminate	$\Delta\Pi = \Delta\Pi_{\mu=0} - \Delta\Pi_{\mu=0.5}$ **(N-mm)**	$\Delta\Pi = \Delta U + W^f - W^p$ **(N-mm)**	**Error**
$[90/-45/45/0/d]_s$	4.894	4.936	0.86%
[0/45/-45/-45/d/45/0]	0.288	0.294	2%

By comparing the results in the second and third columns of Table 4.6, the validity of Equation 2.59 for calculating the energy lost to contact and friction and also the change in potential energy is verified. The maximum difference in the values calculated using the two approaches is 2%, which is acceptable. Another inference that can be made is that, when there is no crack extension, the only form of energy loss in the delaminated region is by sliding friction.

5 RESULTS AND DISCUSSION

5.1 Introduction

Probabilistic analyses are performed on C12K/R6376 graphite/epoxy composite double cantilever beam and end-notched flexure models with a single through-the-width delamination using ANSYS finite element analysis software. The effects of uncertainties on the mixed-mode strain energy release rates are studied using the Monte Carlo simulation technique. The material properties, coefficient of friction, ply thickness, change in fiber orientation, mesh density and consequently, the virtual crack closure length are considered as the random input variables (RVs). Due to the variations in material properties, the transverse shear correction factors for the two sublaminates are also implicit random input variables. Appropriate probability distributions are assumed for the random variables to account for the scatter in the data. Since ANSYS allows only scalar parameters to be assigned as random output parameters (RPs), the total (GSUM), average (GAVG), maximum (GMAX), minimum (GMIN) and mid-point (GMID) strain energy release rate values for each of the three mode components are assigned as the RPs. For analyses in which the effect of friction is included, the total energy release rate (G), the change in elastic strain energy (DELU), total energy lost to friction (WFSUM), total change in potential energy (DELPE) and the ratio of change in elastic strain energy to the energy lost to friction (ERATIO) are assigned as RPs. Since the virtual crack closure length (VCCL) is varied only through the change of mesh density (MRV), it is also declared as an RP. A macro is created to write the mixed-mode SERR distributions along the delamination front with the corresponding RVs for each simulation loop to a text file. This data is later read into MATLAB software as arrays and processed to produce three dimensional contour plots. Then, the maximum and average strain energy release rate values are fit to appropriate distributions. The Anderson-Darling goodness-of-fit test is performed on the data to first check for Weibullness, if that is rejected, the data is subsequently checked for normality and log-normality and a corresponding B-basis value is found. If none of the three distributions fit adequately, then a non-parametric basis value is calculated.

5.2 Probabilistic Analysis Specifications

Table 5.1 lists the settings used for performing the probabilistic analysis using the ANSYS Probabilistic Design System (PDS). As described in section 3.2.5.2, ANSYS offers two probabilistic techniques viz. Monte Carlo simulation and response surface method. Unlike the response surface method, Monte Carlo simulation technique is applicable irrespective of the physical effect modeled and so it is chosen for this study. Out of the direct sampling and the Latin hypercube sampling methods offered by ANSYS, the latter possesses process memory and so clusters of samples are avoided and also it gives importance to the tail of the distribution. So the Latin hypercube sampling method is chosen for this study. During the execution of the probabilistic run, the mean and standard deviation histories of the random output parameters are checked for an accuracy of 1% and 2% respectively every tenth simulation loop. If the accuracy is within the prescribed criteria for all the output parameters, the probabilistic run is automatically stopped.

Table 5.1 Probabilistic analysis specifications

Probabilistic analysis technique	Monte Carlo Simulation
Sampling method	Latin Hypercube Sampling
Location of samples	Random location within the intervals
Simulation loops	60
Repetition cycles	2
Auto-stop criteria	Mean accuracy = 1% Standard Deviation accuracy = 2%
Random number generation	Continue updating using derived seed value

Table 5.2 lists the random input variables, their notations in parentheses, and their assumed distributions. The mean values of the material properties correspond to that of the C12K/R6376 graphite/epoxy composite. Fiber misalignment is the small error in the orientation that is manifested by the laying-up process. Figures 5.1-5.9 show the plots of

the probability density functions (PDF) and cumulative distribution functions (CDF) of the random input variables. For all the double cantilever beam and end-notched flexure models a constant laminate length, laminate width and delamination length of 100 mm, 25 mm and 25 mm, respectively, are used. For the double cantilever beam models, all the random input variables except friction coefficient are considered.

Table 5.2 Random input variable definitions

Random Input Variable	Probability distribution	Specification
Longitudinal modulus (E11)	Normal	μ = 146.86 GPa σ = 0.3
Transverse modulus (E22)	Normal	μ = 10.62 GPa σ = 0.2
In-plane shear modulus (G12)	Normal	μ = 5.45 GPa σ = 0.2
Transverse shear modulus (G13)	Normal	μ = 5.45 GPa σ = 0.2
Transverse shear modulus (G23)	Normal	μ = 3.99 GPa σ = 0.2
Ply thickness (TPLY)	Normal	μ = 0.4 mm σ = 0.004
Fiber misalignment (THETA)	Uniform	Minimum = -1° Maximum = 1°
Mesh refinement (MRV)	Uniform	Minimum = 4 Maximum = 22
Virtual crack closure length (VCCL)	Uniform	Minimum = 0.04 mm Maximum = 0.18 mm
Friction Coefficient (FC)	Uniform	Minimum = 0.0 Maximum = 0.8

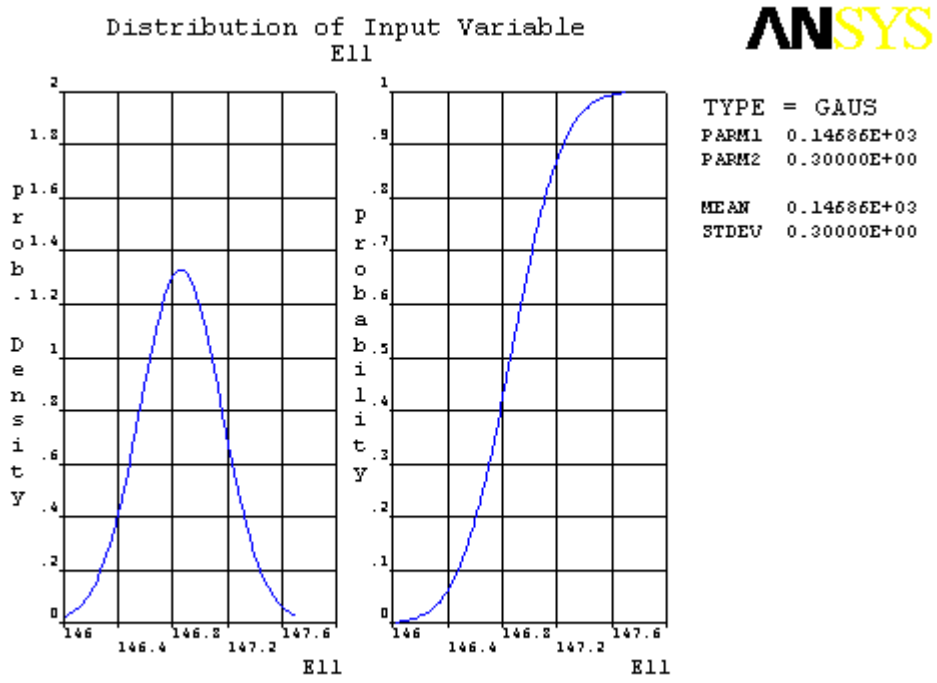

Figure 5.1 Probability density function & cumulative distribution function of longitudinal modulus

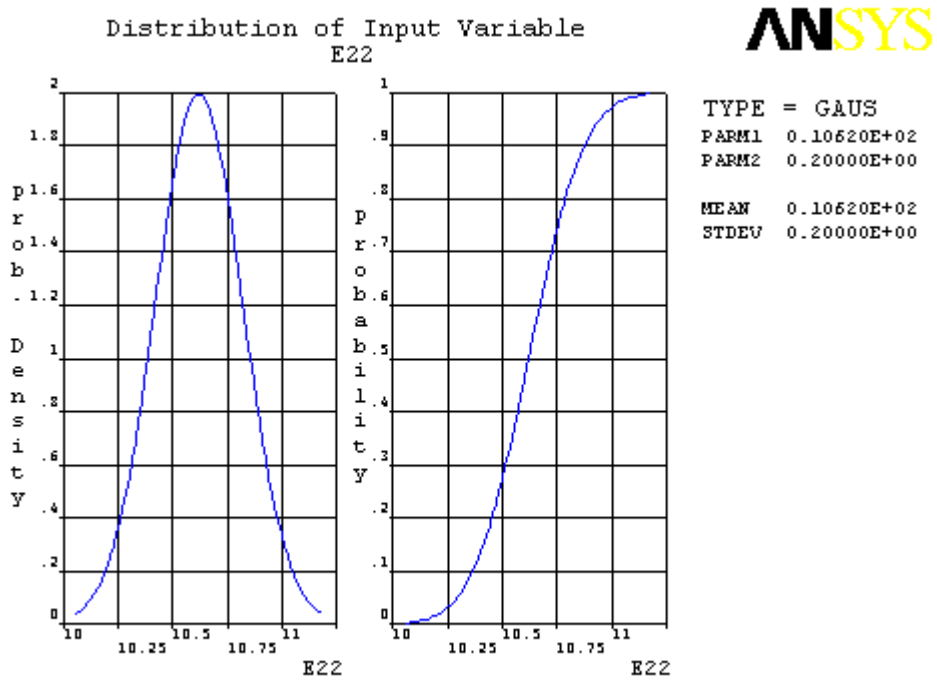

Figure 5.2 Probability density function & cumulative distribution function of transverse modulus

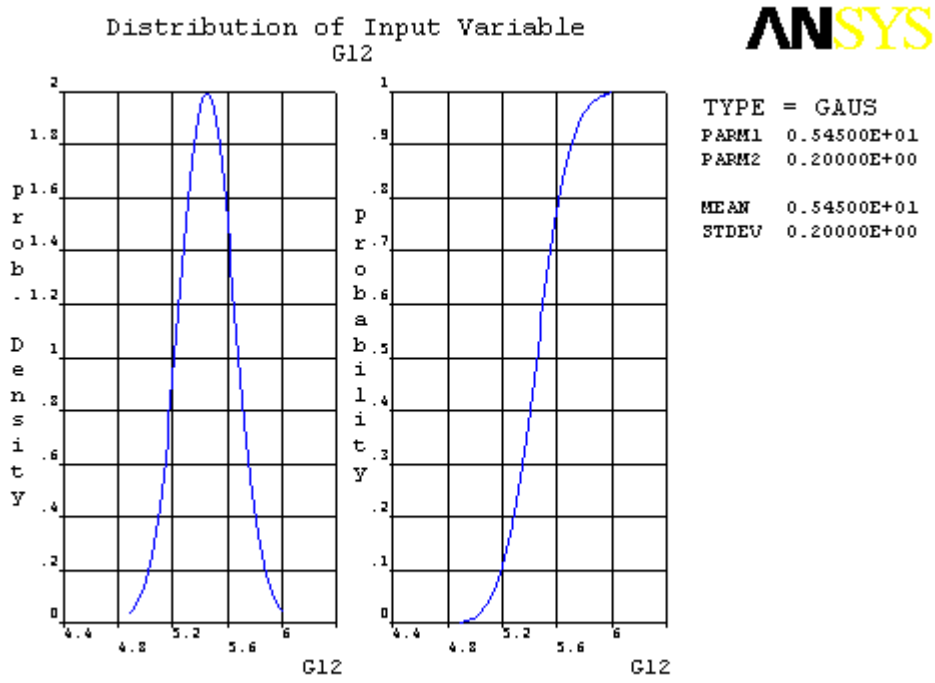

Figure 5.3 Probability density function & cumulative distribution function of in-plane shear modulus

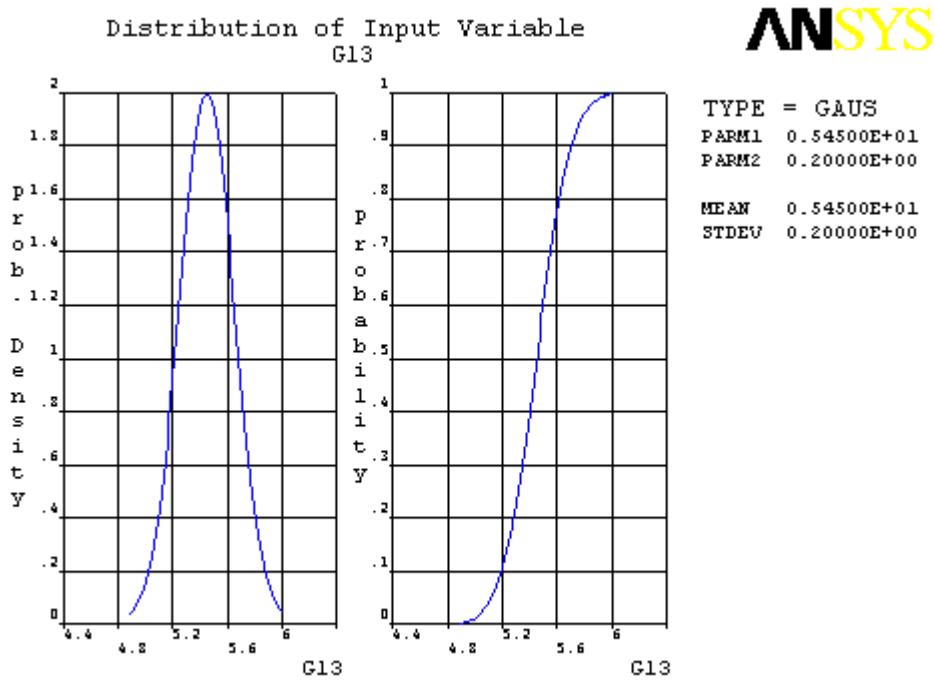

Figure 5.4 Probability density function & cumulative distribution function of transverse shear modulus

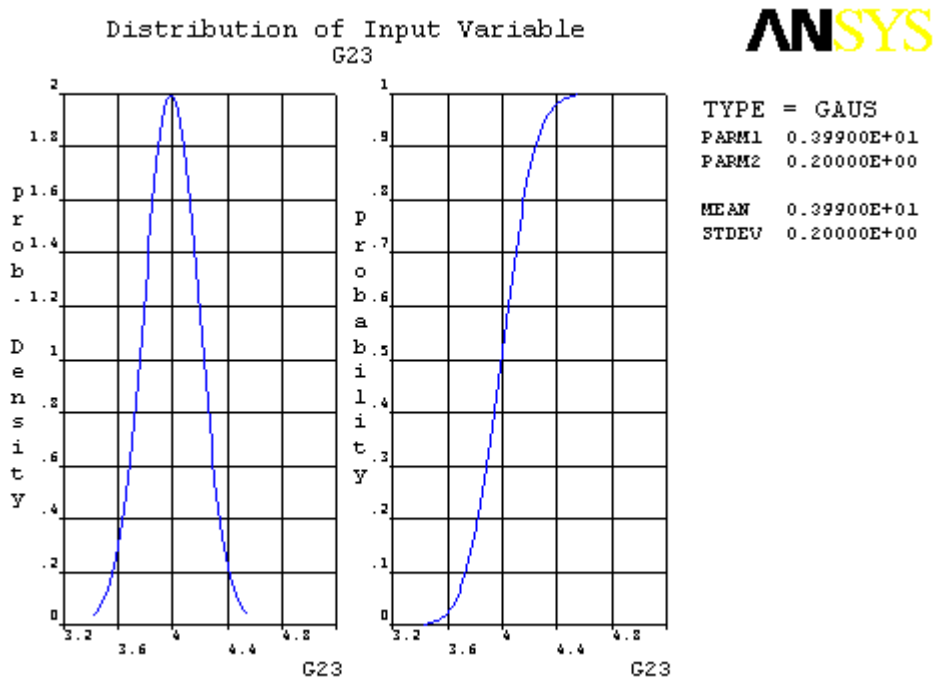

Figure 5.5 Probability density function & cumulative distribution function of transverse shear modulus

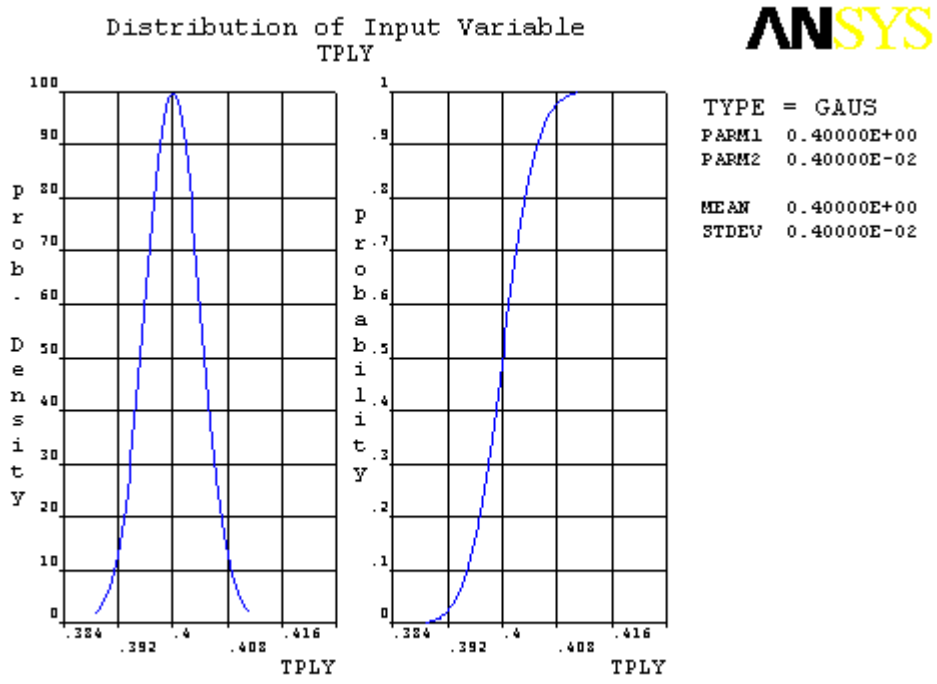

Figure 5.6 Probability density function & cumulative distribution function of ply thickness

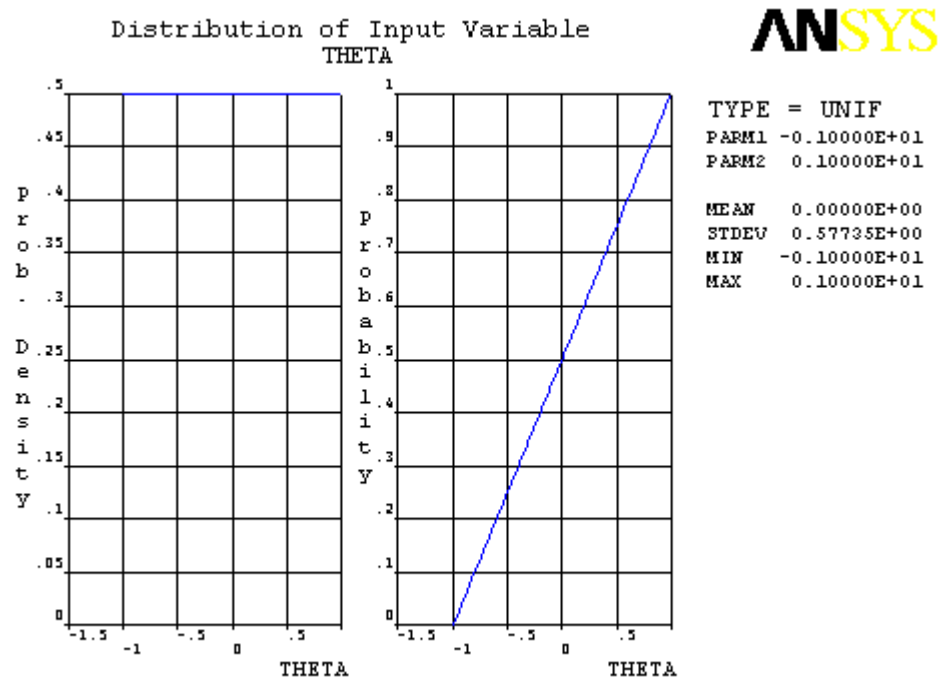

Figure 5.7 Probability density function & cumulative distribution function of fiber misalignment

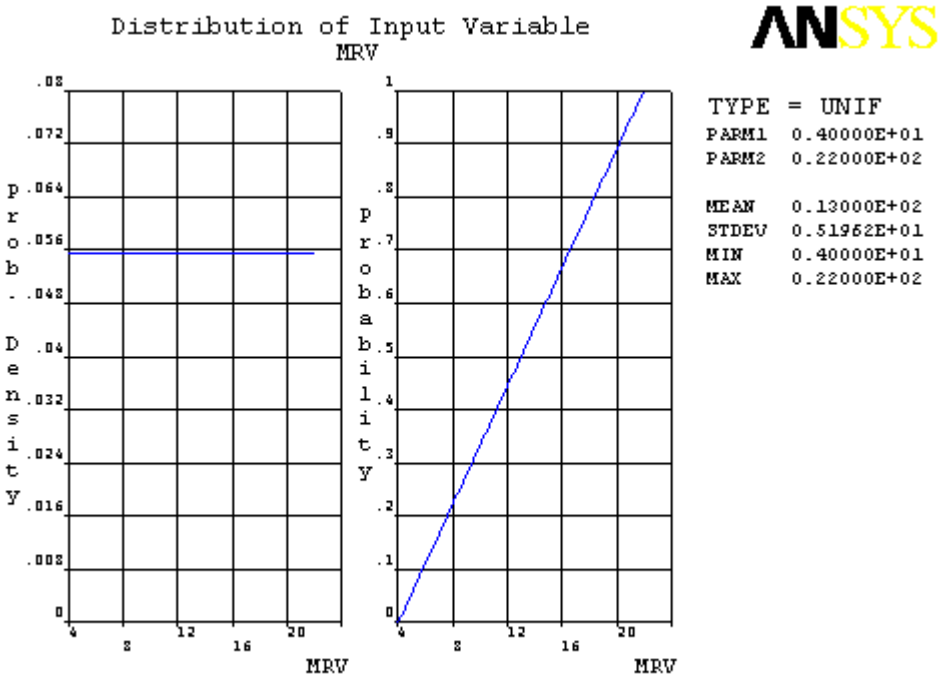

Figure 5.8 Probability density function & cumulative distribution function of mesh refinement value

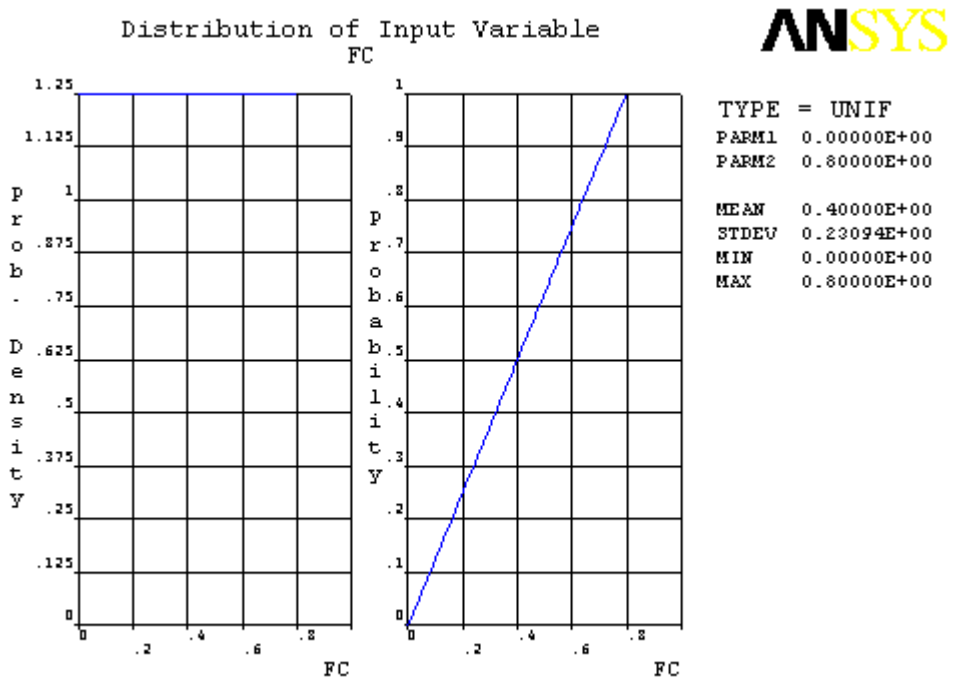

Figure 5.9 Probability density function & cumulative distribution function of friction coefficient

The notations used for the random output parameters are listed in Table 5.3. For the double cantilever beam models, the total strain energy release rate and its mode components are calculated at the centroidal *y*-location of all the crack-tip elements along the delamination front. These values are stored in vectors and their total, average, maximum and minimum values are found and stored in scalar parameters. Similarly, for the end-notched flexure models, the change in elastic strain energy, energy lost to friction, the ratio of these two values and the total strain energy release rate are stored in parameters. The scalar parameters used for storing all these values are declared as random output parameters before the execution of the probabilistic analysis. So, at the end of every simulation loop ANSYS appends the random output parameters to a results file, which is processed to obtain the statistics and trends of the parameters.

Table 5.3 Random output parameter definitions

Random Output Parameter	Description
GSUM/GISUM/GIISUM/GIIISUM	Sum of the total SERR, mode-I, mode-II and mode-III components respectively, across the delamination front
GAVG/GIAVG/GIIAVG/GIIIAVG	Average of the total SERR, mode-I, mode-II and mode-III components respectively, across the delamination front
GMAX/ GIMAX/ GIIMAX/ GIIIMAX	Maximum of the total SERR, mode-I, mode-II and mode-III components respectively, across the delamination front
GMIN/ GIMIN/ GIIMIN/ GIIIMIN	Minimum of the total SERR, mode-I, mode-II and mode-III components respectively, across the delamination front
GMID/ GIMID/ GIIMID/ GIIIMID	Total SERR, mode-I, mode-II and mode-III components respectively at the mid-point of the laminate width
COD	Crack-tip opening displacement at $y = 0$
G	Total SERR in the presence of friction
DELU	Change in elastic strain energy
WFSUM	Total energy lost due to friction
DELPE	Change in potential energy
ERATIO	Ratio of change in elastic strain energy to the energy lost due to friction

5.3 Double Cantilever Beam Model

First, a $[90/-45/45/0]_s$ double cantilever beam model, as shown in Figure 4.1, is considered. The finite element model contains 50 elements along the delamination front. An opening load of 50 N is applied. The opening load produces pure mode-I SERR, as described in chapter 4.1.2, even though the fiber orientation is varied and the bending stiffness matrix coefficients D_{16} and D_{26} are not equal to zero. This is because the laminate is still symmetric with a mid-plane delamination. The total strain energy release rate is almost constant even for a fiber misalignment of THETA = -1°. To study the effects of small change in material mismatch, THETA = -1° is added to the plies of the upper plate and subtracted from the lower plate. A maximum increase in mode-II component of the SERR of 6 J/m^2 is observed at the free edge where the mode-I strain energy release rate peaks. The slope of the trendline that is fit for the maximum mode-I value versus THETA is very small indicating that there is not much variation.

To check if the number of simulation loops is adequate, the mean value history and standard deviation history of all the random output parameters are plotted. It can be seen from the plots for average mode-I SERR (GIAVG) that both the mean and standard deviation converge, i.e., the curves approach a plateau and the width of the confidence bounds are reduced. The same trend is observed for all the other RPs and for all the analyses too. So it is concluded that 120 simulation loops are sufficient for getting accurate statistical data. Table 5.4 lists the statistical properties of the random output parameters.

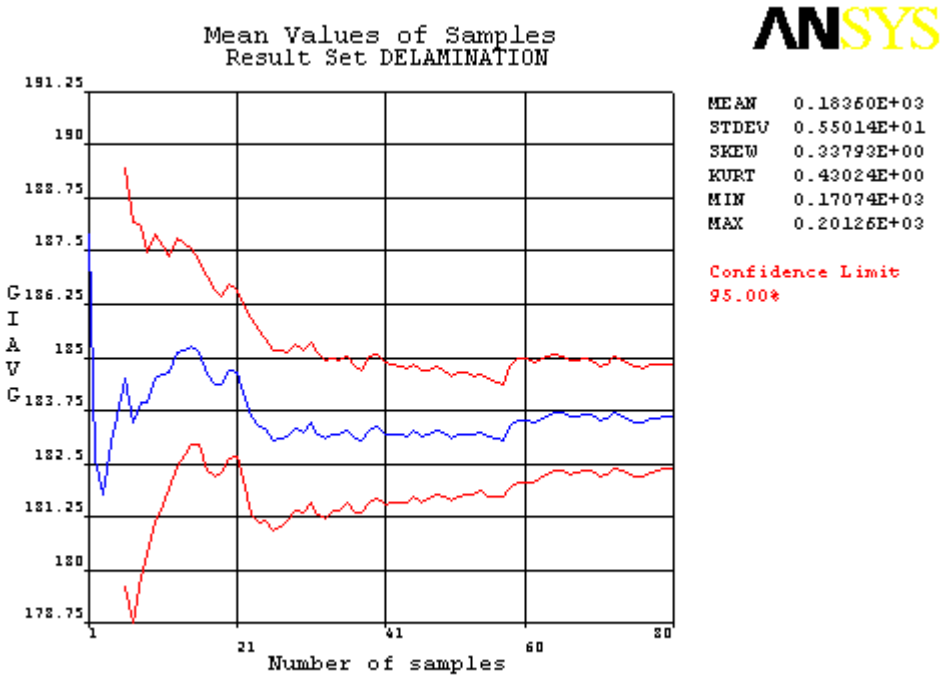

Figure 5.10 Mean value history of GIAVG: $[90/-45/45/0]_s$ double cantilever beam model

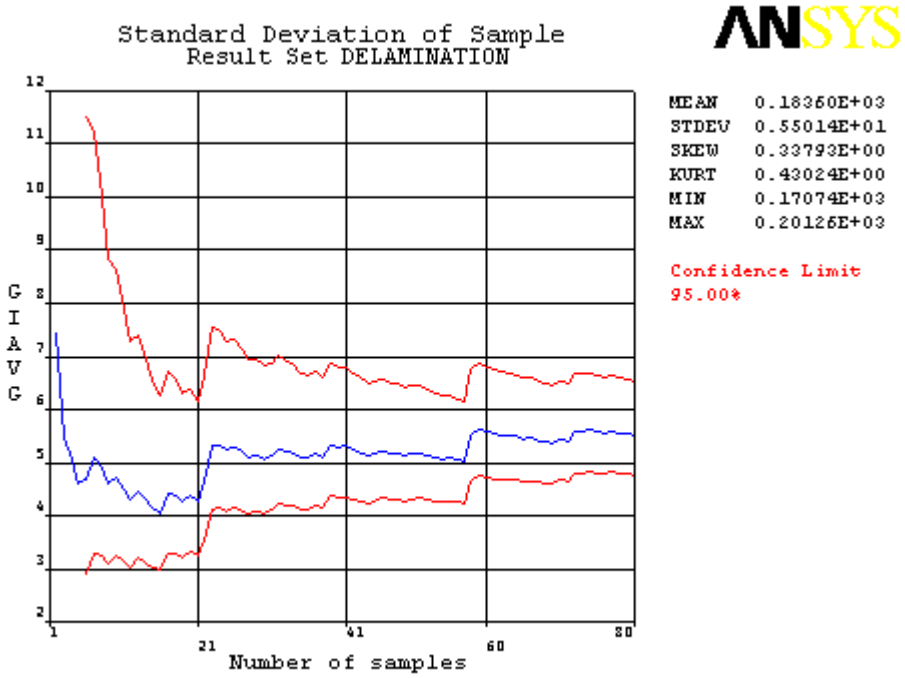

Figure 5.11 Standard deviation history of GIAVG: $[90/-45/45/0]_s$ double cantilever beam model

Table 5.4 Statistics of the random output parameters: $[90/-45/45/0]_s$ double cantilever beam model

Name	Mean	Standard Deviation	Minimum	Maximum
GISUM (J/m^2)	9180.0	275.1	8537	10063
GIAVG (J/m^2)	183.6	5.501	170.7	201.3
GIMAX (J/m^2)	437.4	16.04	403.9	493.9
GIMIN (J/m^2)	109.6	3.654	101.7	122.2
GIMID (J/m^2)	162.9	4.825	150.9	177.5

The average strain energy release rate, GIAVG, can be considered as the total strain energy release rate obtained from a two dimensional analysis under plane stress conditions. So it can be used to compare the delamination growth predictions of two dimensional problems that are currently available in the literature. The maximum strain energy release rate, GIMAX, can be compared with the fracture toughness to determine if delamination growth occurs. The minimum and maximum values for these random output parameters indicate that there is almost an 18.25% scatter in GIAVG values due to the randomness of the input variables. Similarly GIMAX shows a 22.25% scatter. If the fracture toughness were, say, 450 J/m^2 then a deterministic model would predict that delamination growth may or may not occur depending on the values assumed by the input variables. This shows the need for a probabilistic design methodology for prediction of delamination growth.

To find out which of the random input variables have a significant influence on the output parameters, the sensitivities between the input and output based on the Pearson linear correlation coefficients listed in Table 5.5 are visualized using sensitivity plots. A significance level of 2.5% is used to identify the significant and insignificant random input variables for each of the random output parameters. Both absolute and relative sensitivities are plotted in bar and pie chart forms respectively.

Table 5.5 Correlation between input and output variables: $[90/-45/45/0]_s$ double cantilever beam

model

Out\Inp	E11	E22	G12	G13	G23	TPLY	THETA	MRV
VCCL	0.094	small	-0.185	0.141	-0.056	0.056	0.218	-0.914
COD	-0.051	0.184	0.078	0.044	-0.280	0.940	-0.056	-0.019
GISUM	0.036	-0.136	0.038	-0.062	0.281	-0.966	0.019	0.088
GIAVG	0.036	-0.136	0.038	-0.062	0.281	-0.966	0.019	0.088
GIMAX	0.049	-0.333	-0.206	small	0.344	-0.797	0.023	0.280
GIMIN	0.029	-0.091	-0.039	0.050	0.347	-0.957	0.050	-0.051
GIMID	0.016	-0.043	0.131	-0.086	0.253	-0.987	-0.002	0.088

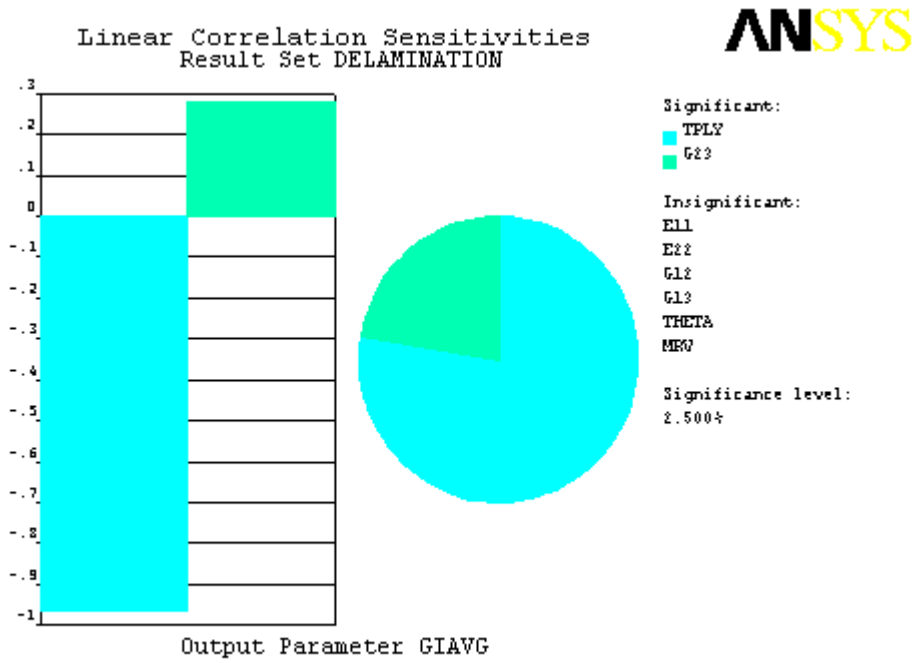

Figure 5.12 Sensitivity plot of GIAVG: $[90/-45/45/0]_s$ double cantilever beam model

Interlaminar stresses contribute significantly to the mode-I energy release rate. This is evident from the sensitivity plots of GIAVG and GIMAX shown in Figures 5.12 and 5.13 respectively, where transverse shear modulus is a significant variable. As

transverse shear modulus increases the mode-I strain energy release rate increases. Also, the SERR is directly proportional to the compliances of the two sublaminates. Since the compliance decreases with increase in thickness, the SERR decreases when thickness increases. From figure 5.3(b) it can be seen that as the mesh refinement value (MRV) increases, the virtual crack closure length decreases and so the maximum SERR, GIMAX, is evaluated accurately. This is mainly because the maximum value occurs at the free edge. It should be noted that the present formulation is not sensitive to the mesh density in evaluating the average strain energy release rate or the minimum and midpoint values.

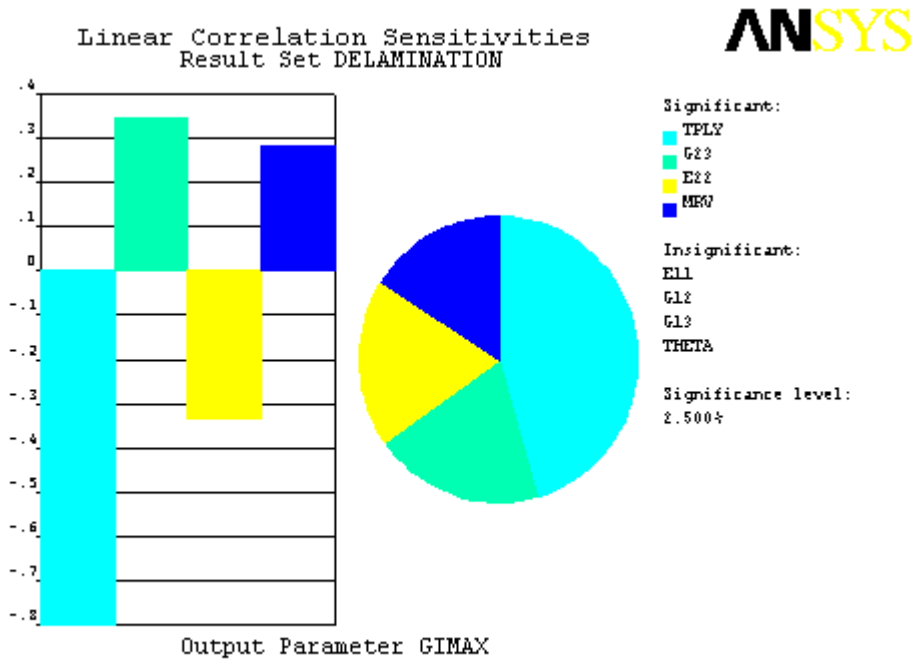

Figure 5.13 Sensitivity plot of GIMAX: $[90/-45/45/0]_s$ double cantilever beam model

After finding out the sensitivities, scatter plots of GIAVG and GIMAX versus the most significant design variable, the ply thickness, are obtained. The scatter plots in Figures 5.14-5.15 show the sample points and the trendline fitted for the data. For both cases a cubic polynomial is sufficient to describe the relationship between the input and output variables. The advantage of fitting a trendline is that, an approximate solution for the output parameter as a function of the random input variable is obtained. The coefficients of the cubic equations and the accuracy measures of the trendlines are listed

beside the scatter plots. The deviation of the sample points from this trendline are controlled by the influence of all the other input variables. For example, in the scatter plot for GIAVG, the deviation from the trendline is controlled by the variation in the transverse shear modulus. The scatter plots help in assessing how far the accuracy of prediction of the SERR values can be improved by reducing the scatter in the ply thickness. By controlling the tolerance of ply thickness to ± 0.002 mm, the average SERR could be predicted to an accuracy of ± 3 J/m^2.

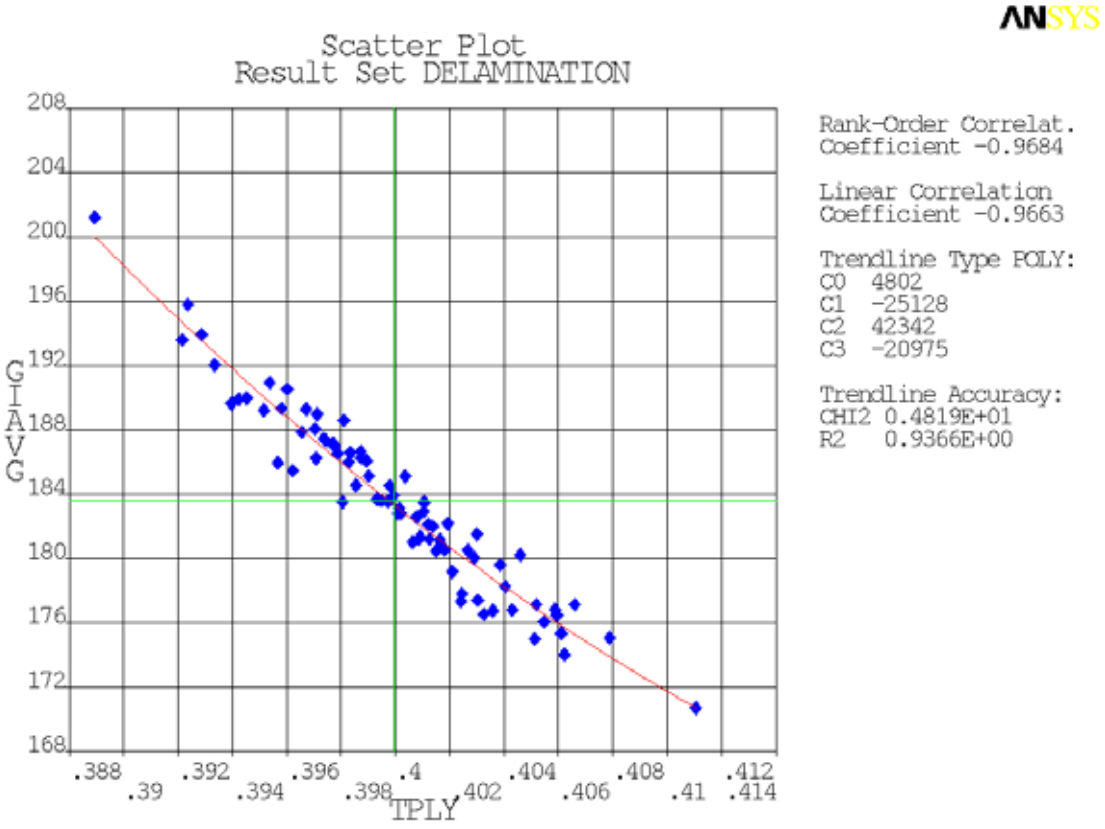

Figure 5.14 Scatter plot of GIAVG vs. ply thickness: [90/-45/45/0]$_s$ double cantilever beam model

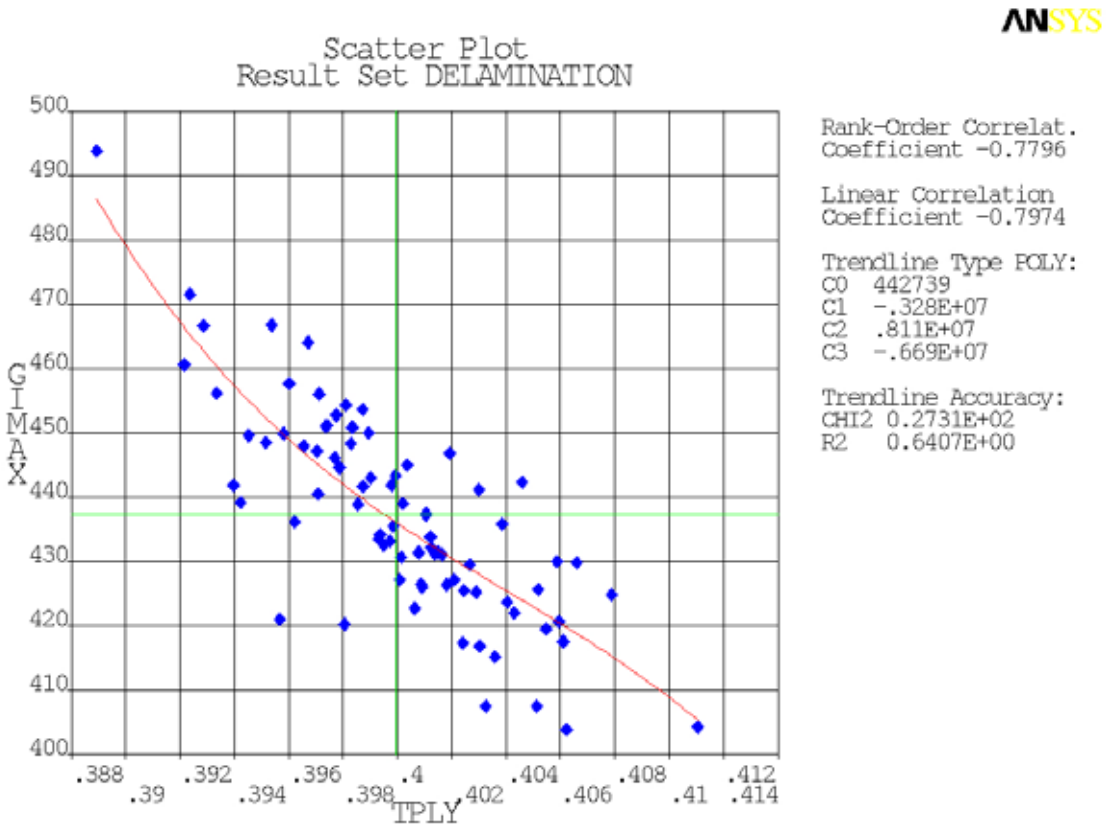

Figure 5.15 Scatter plot of GIMAX vs. ply thickness: $[90/-45/45/0]_s$ double cantilever beam model

As stated in Section 5.1, the distribution of mode-I SERR along the delamination front and the normalized width data are appended to a text file every simulation loop. This data is read into MATLAB software as arrays. A mesh grid is created by converting arrays into matrices for the normalized width versus ply thickness values using the '*meshgrid*' command with a grid resolution of 360 along both the axes. The interpolation of the SERR values to fit this grid is done using the MATLAB v4 grid data method. Figure 5.5 shows the three dimensional contour plot of the distribution as a function of the ply thickness created using the '*mesh*' command. The critical SERR, G_{IC} can be compared with the data points in the plot to determine at which locations along the crack front delamination growth would occur.

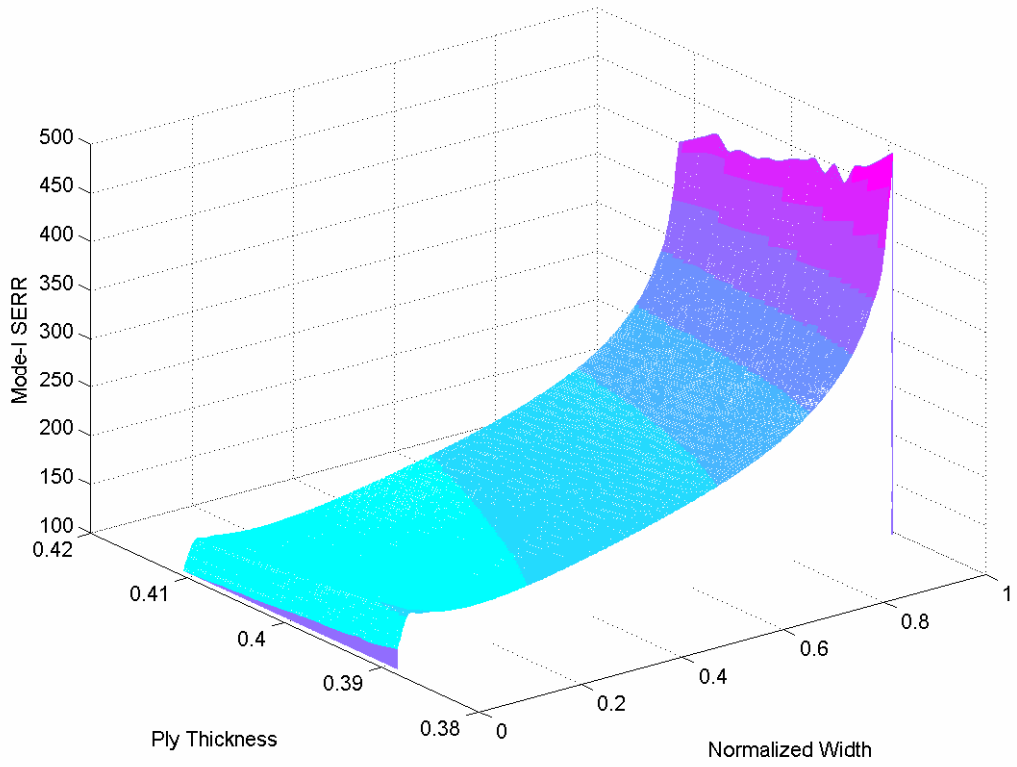

Figure 5.16 Three dimensional contour plot of mode-I SERR distribution: $[90/-45/45/0]_s$ double cantilever beam model

The next step is to fit the maximum and average strain energy release rates to appropriate distributions and calculate the basis values. The GIAVG values from the 80 simulation loops (solution converged after 80 loops) are listed in Table 5.6. An Anderson-Darling test is performed to first test if the data is from a Weibull distribution. For that an estimate of the scale parameter, α, and shape parameter, β of the Weibull distribution are required. Using the guidelines given in the Composite Materials Handbook (2002), the initial guess for β is chosen to be $(1.28/S_y)$ which is equal to 33.327, where S_y is the geometric standard deviation of the data. The final solution for β (31.618) is obtained through iteration and α (1.863) is calculated as a function of β. The Anderson-Darling test statistic is found to be 1.552 and the Observed Significance Level (*OSL*) is $5.08e^{-4}$. Since the *OSL* is less than 0.05, the hypothesis that the data fits a Weibull distribution is rejected. Next the data is checked for normality and an *OSL* of 0.394 is obtained. So the hypothesis that the data comes from a normal distribution is accepted.

The *B*-basis value is calculated as a function of the mean, standard deviation and the sample size of 80. In Table 5.7, 'parameter 1' refers to the mean and 'parameter 2' refers to the standard deviation. The *B*-basis value is found to be 175 J/m^2, which means that if sample data is obtained repeatedly from the population and basis values calculated, 95% of time the calculated value falls below the 10th percentile.

Table 5.6 GIAVG (J/m^2) values from probabilistic analysis: [90/-45/45/0]$_s$ double cantilever beam model

1.88E+02	1.84E+02	1.77E+02	1.81E+02	1.83E+02
1.77E+02	1.75E+02	1.84E+02	1.87E+02	1.77E+02
1.80E+02	1.71E+02	1.82E+02	1.89E+02	1.81E+02
1.87E+02	1.78E+02	1.82E+02	1.88E+02	1.84E+02
1.86E+02	1.81E+02	1.90E+02	1.84E+02	1.91E+02
1.89E+02	1.77E+02	1.76E+02	1.78E+02	1.87E+02
1.77E+02	1.85E+02	1.85E+02	1.84E+02	1.75E+02
1.87E+02	1.84E+02	1.89E+02	1.88E+02	1.81E+02
1.84E+02	1.89E+02	1.80E+02	1.82E+02	1.94E+02
1.90E+02	1.81E+02	1.77E+02	1.74E+02	1.85E+02
1.85E+02	1.90E+02	1.89E+02	1.86E+02	1.80E+02
1.85E+02	1.75E+02	1.83E+02	1.96E+02	1.81E+02
1.91E+02	1.79E+02	1.81E+02	1.77E+02	2.01E+02
1.86E+02	1.87E+02	1.87E+02	1.76E+02	1.94E+02
1.86E+02	1.83E+02	1.77E+02	1.81E+02	1.83E+02
1.83E+02	1.86E+02	1.84E+02	1.82E+02	1.92E+02

Table 5.7 Statistical characteristics of SERR values: [90/-45/45/0]$_s$ double cantilever beam model

Variable	Distribution	Parameter 1	Parameter 2	*B*-Basis Value
GIAVG (J/m^2)	Normal	183.6	5.528	175
GIMAX (J/m^2)	Normal	437.4	16.04	412.38

The next double cantilever beam model is the [0/45$_3$/d/45/0] laminate which has an offset delamination between plies of same orientation. For this model too, an opening load of 50 N is applied. The loading produces all three components of the strain energy release rate though the distribution of the mode-III component is fairly constant along the delamination front and is small compared to the mode-I and mode-II components. Both the mode-I and mode-II components peak at one of the free edges. Unlike the symmetric laminate with mid-plane delamination, the effects of fiber misalignment, THETA are not negligible and control all three components to some extent. The statistics are listed in Table 5.8 and the sensitivity plots are shown in Figures 5.17-5.22.

Table 5.8 Statistics of the random output parameters: [0/45$_3$/d/45/0] double cantilever beam model

Name	Mean	Standard Deviation	Minimum	Maximum
GAVG (J/m^2)	725.0	21.15	668.3	779.9
GMAX (J/m^2)	1578	95.70	1322	1792
GIAVG (J/m^2)	695.8	20.35	641.1	747.8
GIMAX (J/m^2)	1431	86.35	1198	1625
GIIAVG (J/m^2)	12.16	0.7149	10.52	13.97
GIIMAX (J/m^2)	137.0	14.63	98.12	170.5
GIIIMAX (J/m^2)	31.87	1.309	28.99	35.17

The mode-I component is mostly controlled by the amount by which the other two components vary. Figures 5.19-5.21 show that, the in-plane shearing mode component, mode-II, is influenced by the in-plane shear modulus and similarly the scissoring mode component, mode-III, is controlled by the transverse modulus. As can be seen in Figure 5.17, the mode-I SERR is negatively correlated to the ply thickness as described for the previous laminate configuration. In the case of the symmetric laminate the transverse shear modulus influenced the total SERR and mode-I component directly. But in this case, the in-plane shear modulus and the transverse modulus, which are

inversely correlated to the mode-II and mode-III components, control the average of the total strain energy release rate and also the minimum and midpoint values while the transverse shear modulus has a negligible effect. This trend is reflected in the distribution of the mode-I component as well. But, at the free edge, the reverse trend of GIMAX increasing with increase in in-plane shear modulus is observed. This can be attributed to the increase in the crack-tip opening displacement with an increase in the in-plane shear modulus. The virtual crack closure length has a sizeable effect on the evaluation of the maximum mode-I and mode-II strain energy release rate values. Also, as the fiber misalignment increases, the material mismatch increases. This leads to an increase in the predicted mode-ratio, G_{II}/G and consequently the mode-I SERR decreases and the mode-II component increases.

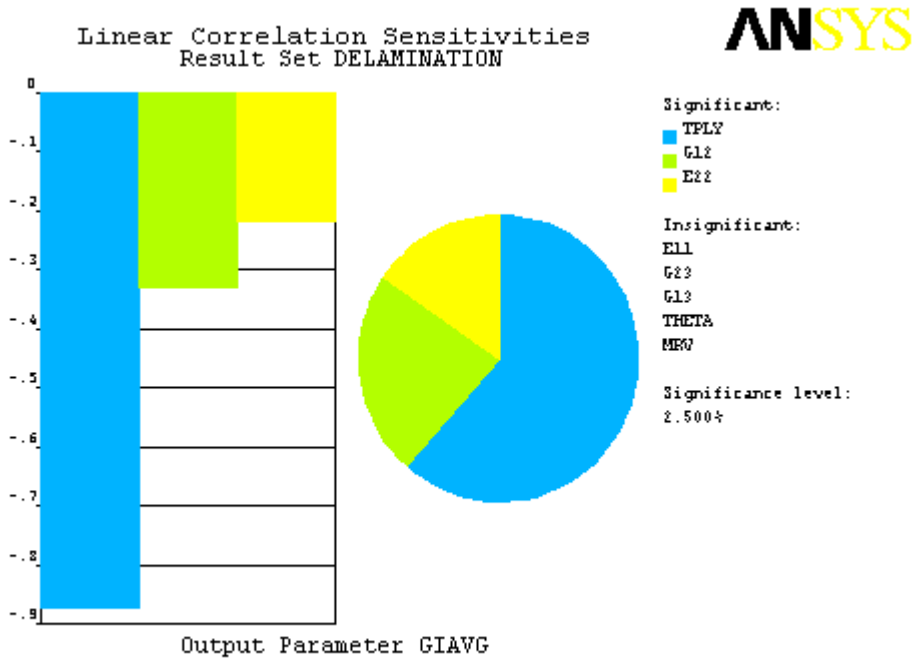

Figure 5.17 Sensitivity plot of GIAVG: [0/45$_3$/d/45/0] double cantilever beam model

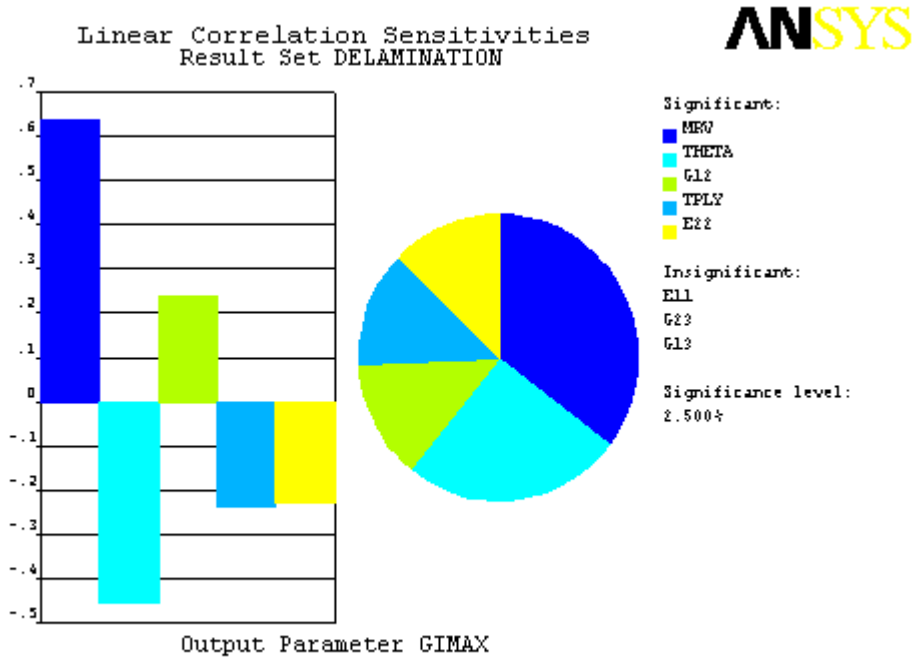

Figure 5.18 Sensitivity plot of GIMAX: [0/45$_3$/d/45/0] double cantilever beam model

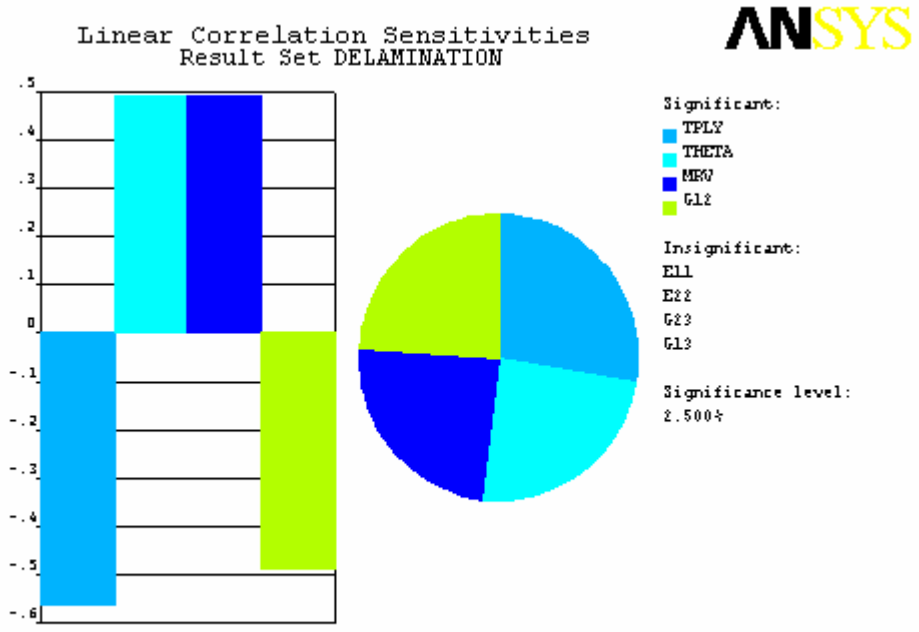

Figure 5.19 Sensitivity plot of GIIAVG: [0/45$_3$/d/45/0] double cantilever beam model

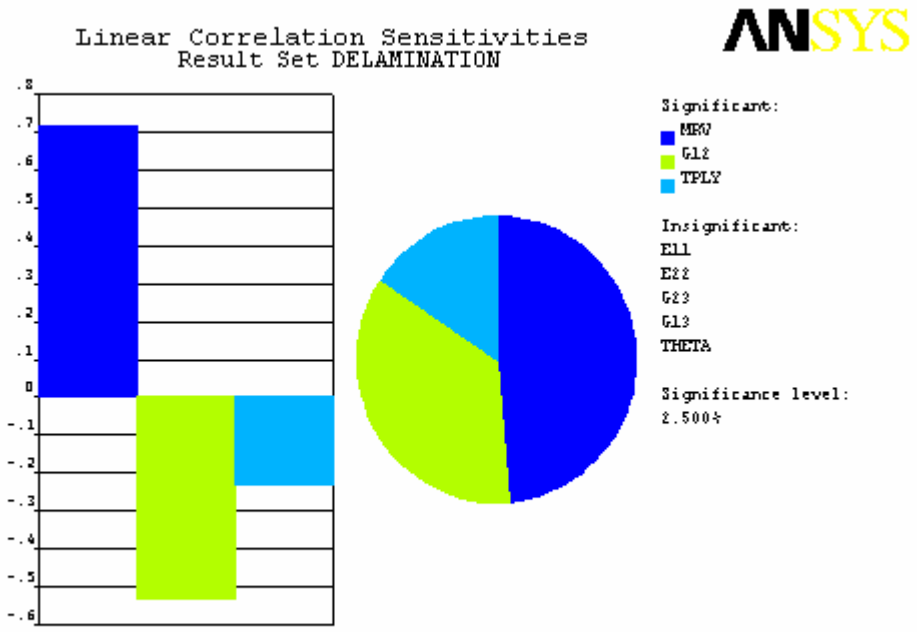

Figure 5.20 Sensitivity plot of GIIMAX: [0/45$_3$/d/45/0] double cantilever beam model

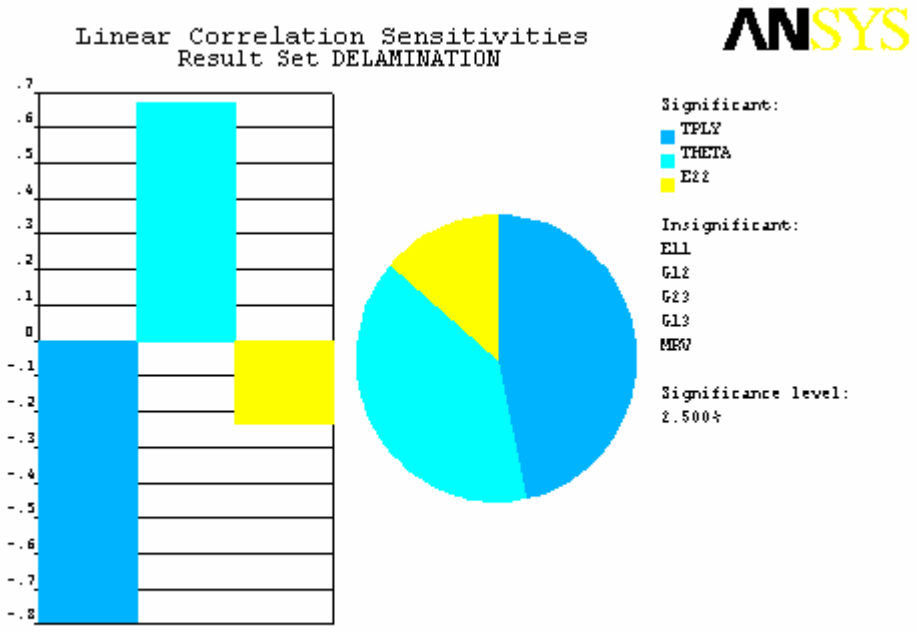

Figure 5.21 Sensitivity plot of GIIIMAX: [0/45$_3$/d/45/0] double cantilever beam model

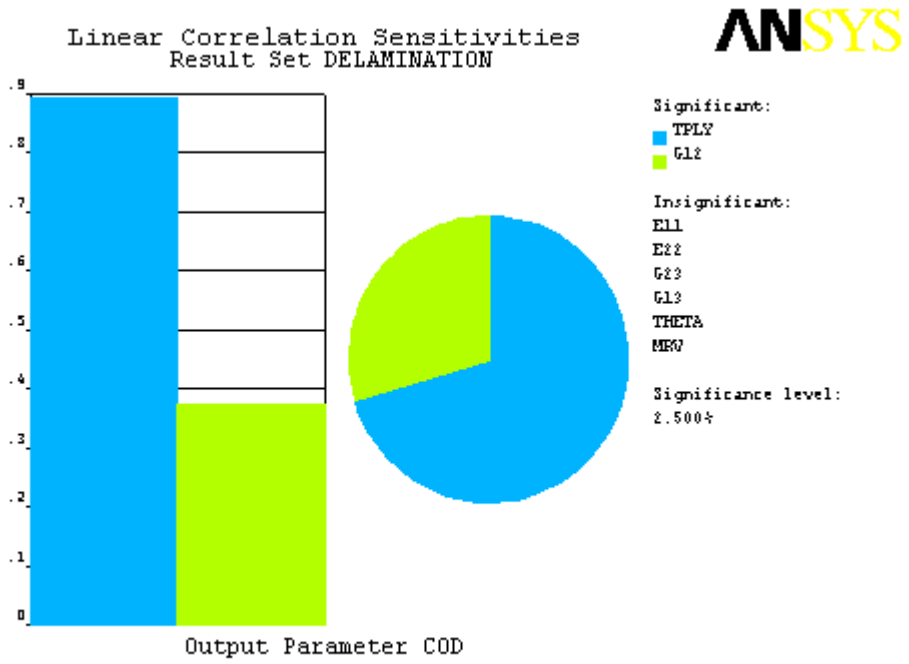

Figure 5.22 Sensitivity plot of COD: [0/45$_3$/d/45/0] double cantilever beam model

Figures 5.23-5.26 show the scatter plots of the SERR values versus the corresponding significant random input variables. For GIAVG, the slope of the trendline indicates a very high scatter even for small variations in ply thickness. By controlling the tolerance of the ply thickness to $\pm$ 0.002 mm, the average SERR can be predicted to an accuracy of $\pm$ 9 J/m^2. Similarly, by controlling the tolerance of fiber orientation to $\pm$ 0.2 degrees, the average SERR can be predicted to an accuracy of $\pm$ 20 J/m^2.

Table 5.9 lists the type of distribution that fit the various strain energy release rate values, the parameters of the distributions and the *B*-basis values. It can be seen that the maximum mode-II SERR value could not be fit to a Weibull, normal, or log-normal distribution and so a non-parametric basis value is calculated using the method described in Section 2.10.1.4.

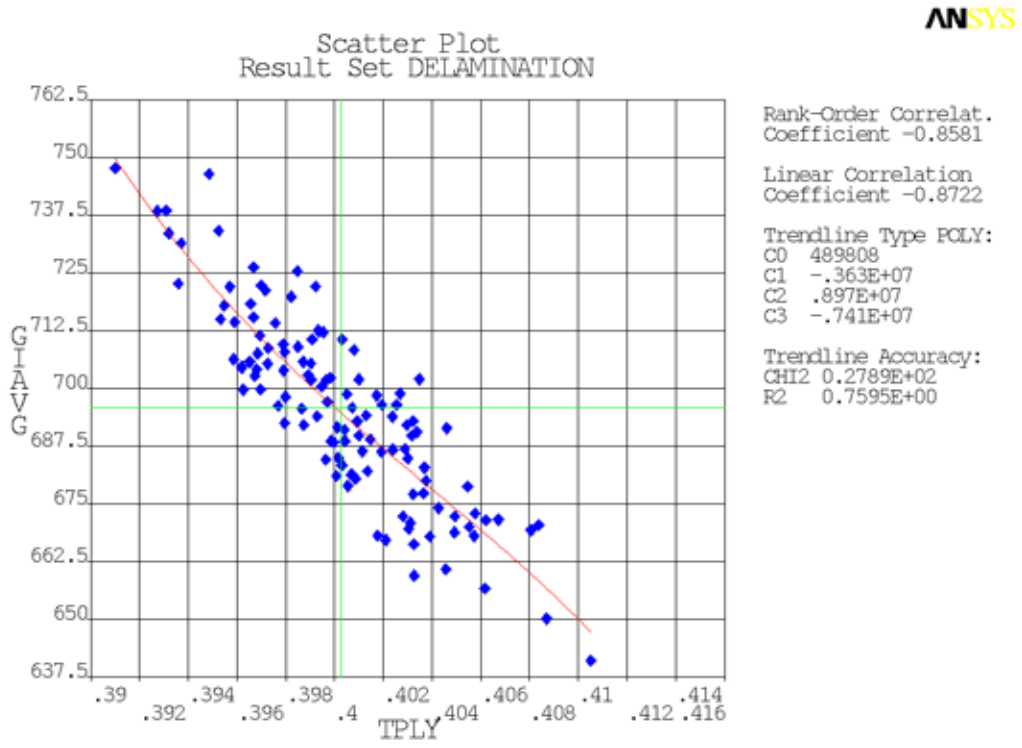

Figure 5.23 Scatter plot of GIAVG vs. ply thickness: [0/45$_3$/d/45/0] double cantilever beam model

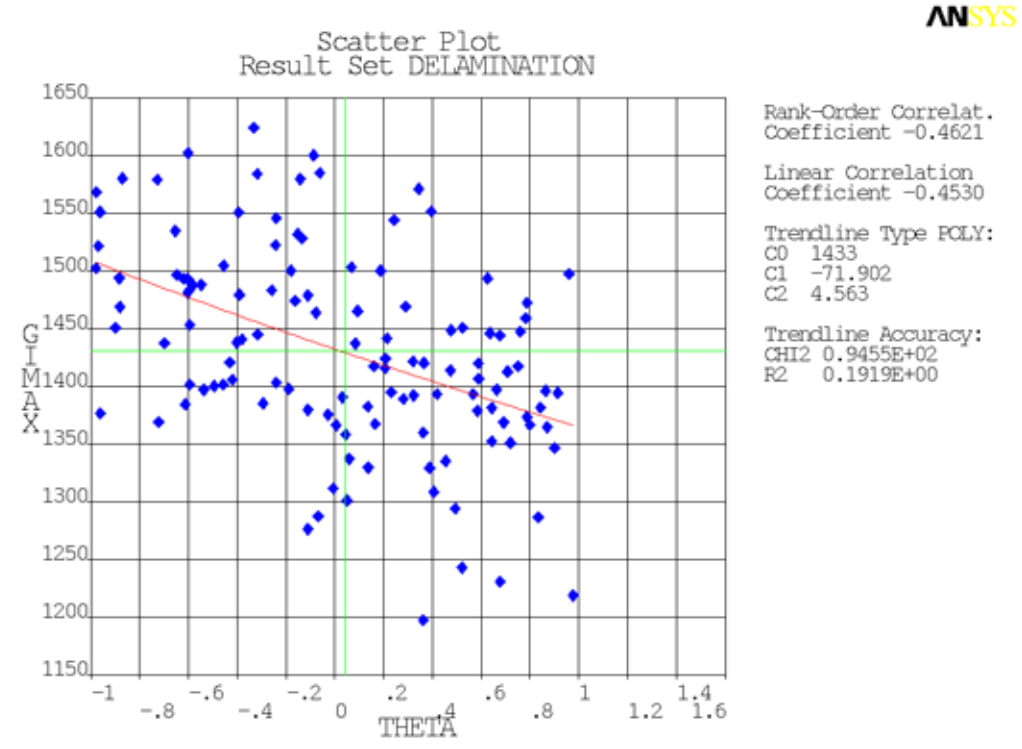

Figure 5.24 Scatter plot of GIMAX vs. fiber misalignment: [0/45$_3$/d/45/0] double cantilever beam model

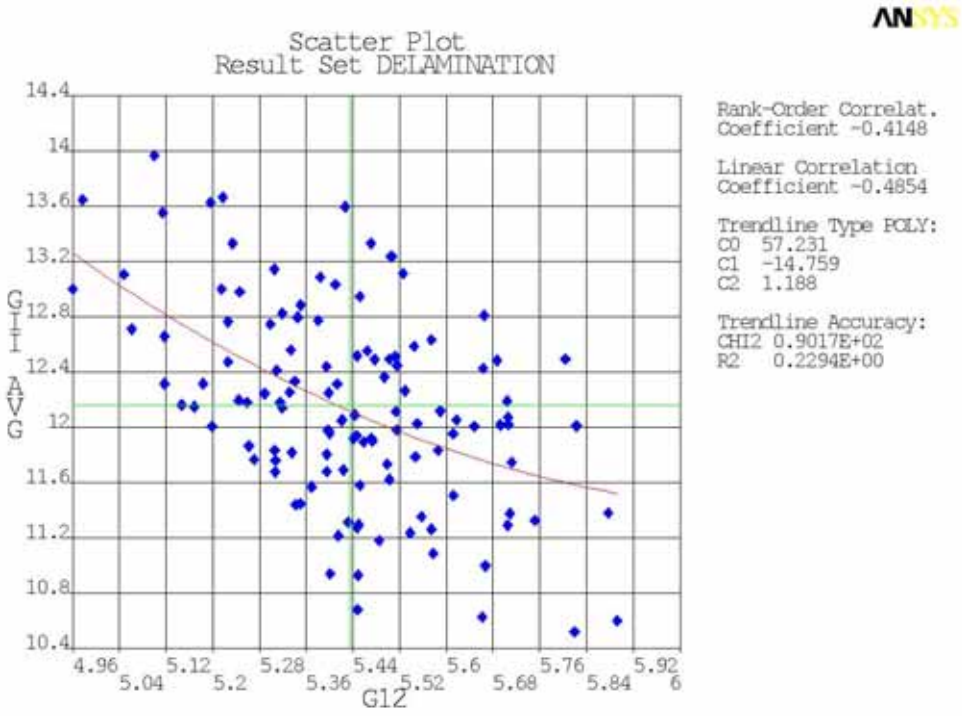

Figure 5.25 Scatter plot of GIIAVG vs. in-plane shear modulus: [0/45$_3$/d/45/0] double cantilever beam model

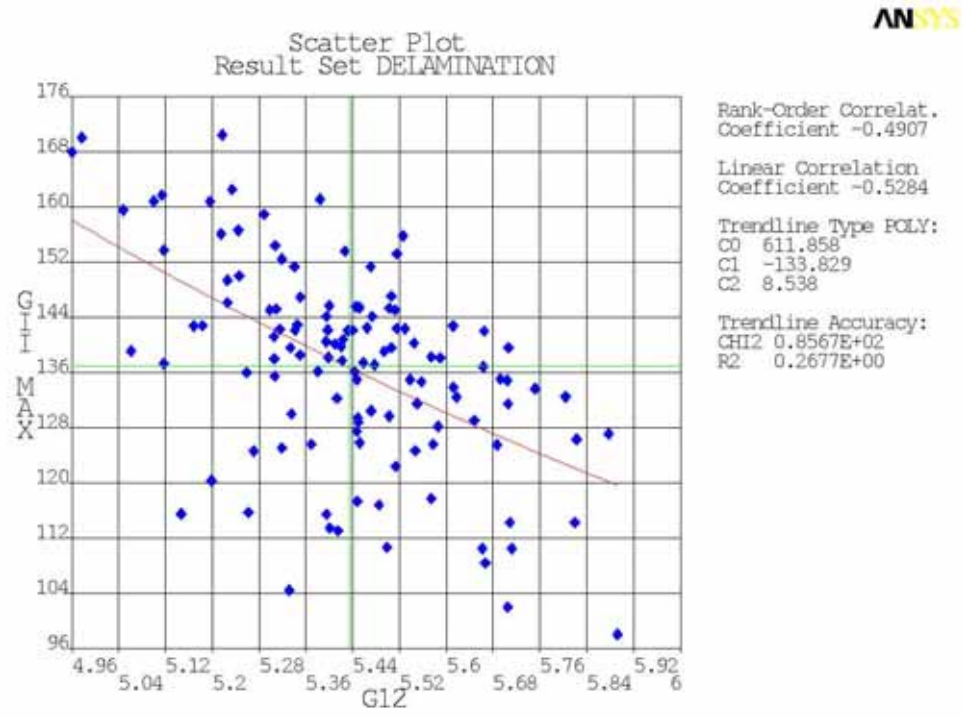

Figure 5.26 Scatter plot of GIIMAX vs. in-plane shear modulus: [0/45$_3$/d/45/0] double cantilever beam model

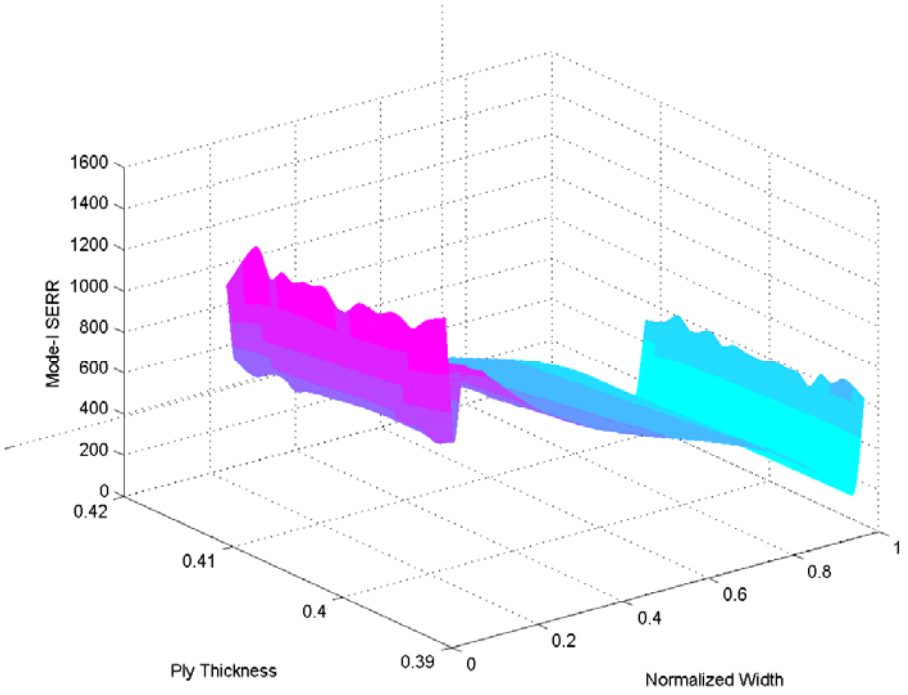

Figure 5.27 Three dimensional contour plot of Mode-I SERR distribution: [0/45$_3$/d/45/0] double cantilever beam model

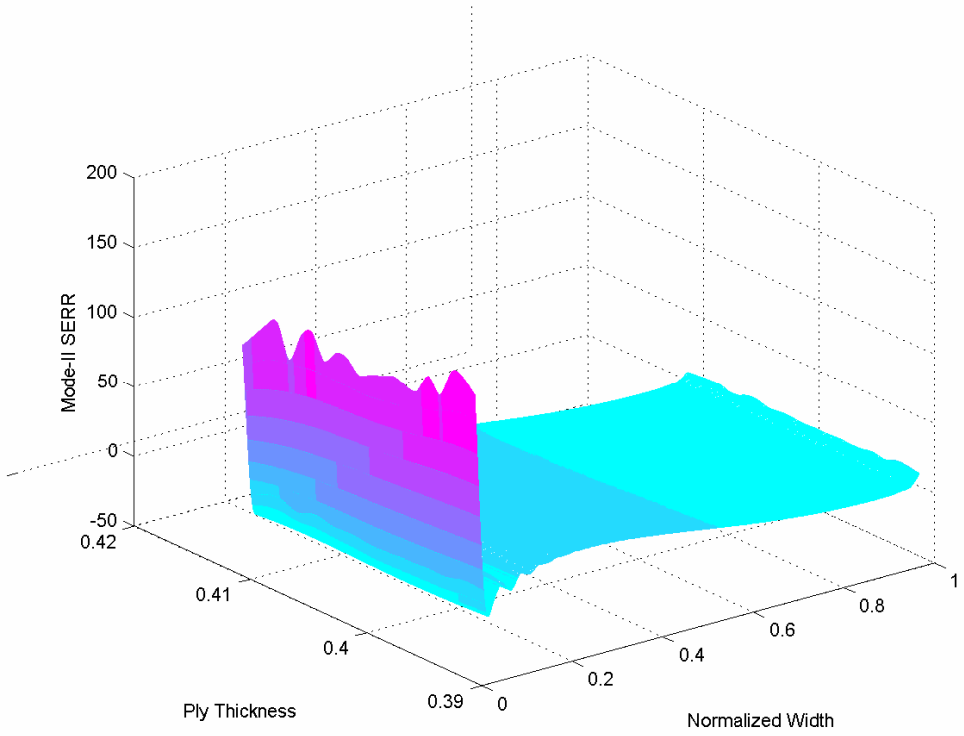

Figure 5.28 Three dimensional Contour plot of Mode-II SERR distribution: [0/45$_3$/d/45/0] double cantilever beam model

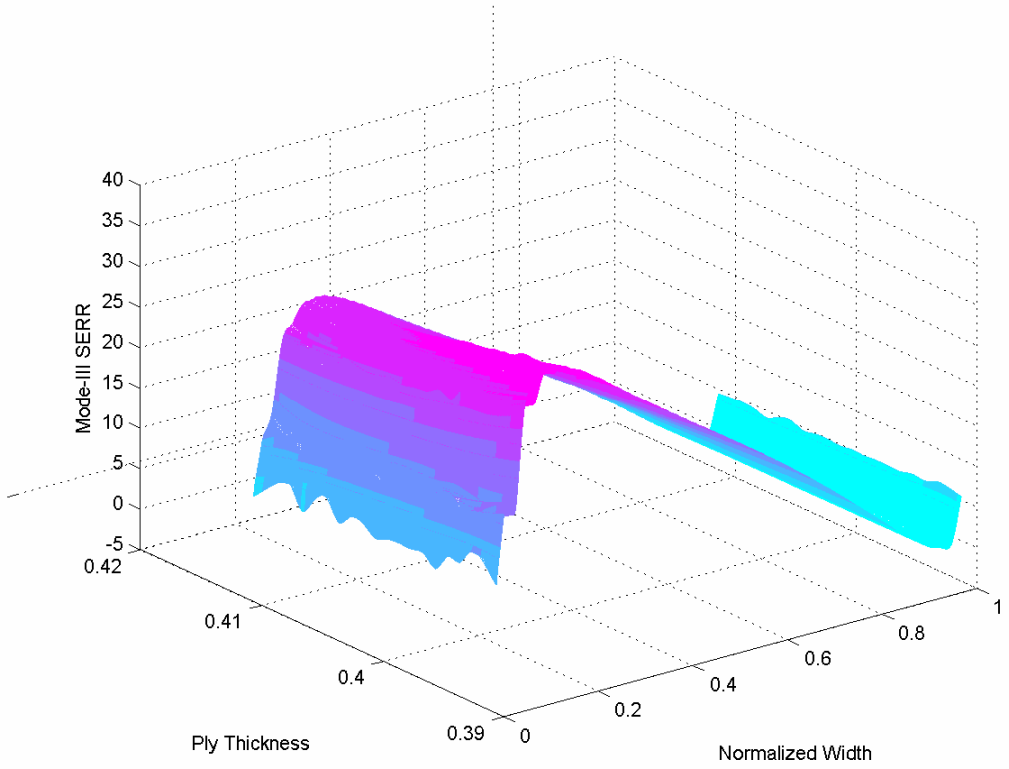

Figure 5.29 Three dimensional contour plot of Mode-III SERR distribution: [0/45$_3$/d/45/0] double cantilever beam model

Table 5.9 Statistical characteristics of SERR values: [0/45$_3$/d/45/0] double cantilever beam model

Variable	Distribution	Parameter 1	Parameter 2	*B*-Basis Value
GAVG (J/m^2)	Normal	724.95	21.12	693.18
GMAX (J/m^2)	Normal	1578.08	95.76	1434.05
GIAVG (J/m^2)	Normal	695.85	20.41	665.14
GIMAX (J/m^2)	Normal	1430.91	85.96	1301.62
GIIAVG (J/m^2)	Normal	12.16	0.71	11.08
GIIMAX (J/m^2)	Non-parametric	-	-	111.00
GIIIMAX (J/m^2)	Normal	31.87	1.31	29.89

The next model to be analyzed is a [0/45/-45/-45/d/45/0] laminate since it has an offset delamination which is between plies of different orientation. The opening load is doubled to 100 N from 50 N to see if the mode-II component would increase appreciably. But the mode-II and the mode-III components observed are too small to initiate failure. The statistics of the random output parameters are given in Table 5.10 and the sensitivity plots are shown in Figures 5.30-5.34. Unlike the previous case, a small change in fiber orientation has a significant effect on even the average mode-I component of the strain energy release rate. The trends of the other parameters are similar except that the mode-III component is not influenced by the transverse modulus. Figures 5.35-5.38 show the scatter plots of the SERR values versus the corresponding significant random input variables. By controlling the tolerance of the ply thickness to ± 0.002 mm, the average SERR can be predicted to an accuracy of $\pm$ 40 J/m^2. Similarly, by controlling the tolerance of fiber orientation to ± 0.2 degrees, the maximum mode-I and mode-II SERR can be predicted to an accuracy of $\pm$ 125 J/m^2 and $\pm$ 10 J/m^2 respectively.

Table 5.10 Statistics of the random output parameters: [0/45/-45$_2$/d/45/0] double cantilever beam model

Name	Mean	Standard Deviation	Minimum	Maximum
GAVG (J/m^2)	3317	121.5	3033	3676
GMAX (J/m^2)	6576	465.7	5585	7843
GIAVG (J/m^2)	3187	115.7	2916	3529
GIMAX (J/m^2)	6348	433.3	5435	7504
GIIAVG (J/m^2)	75.01	7.178	60.55	96.93
GIIMAX (J/m^2)	224.7	45.31	140.8	332.3
GIIIMAX (J/m^2)	84.36	4.331	75.76	96.73

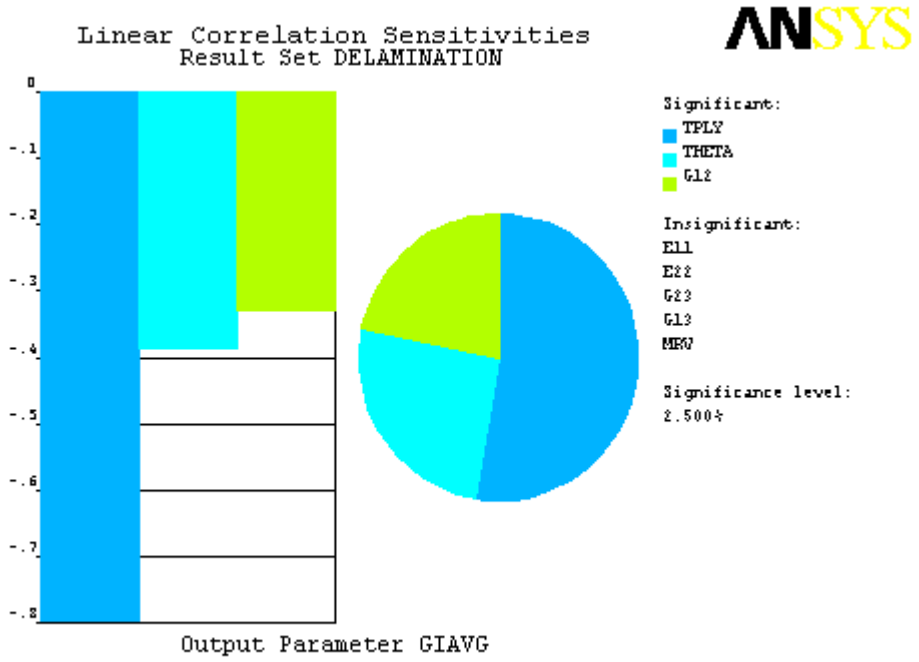

Figure 5.30 Sensitivity plot of GIAVG: [0/45/-45$_2$/d/45/0] double cantilever beam model

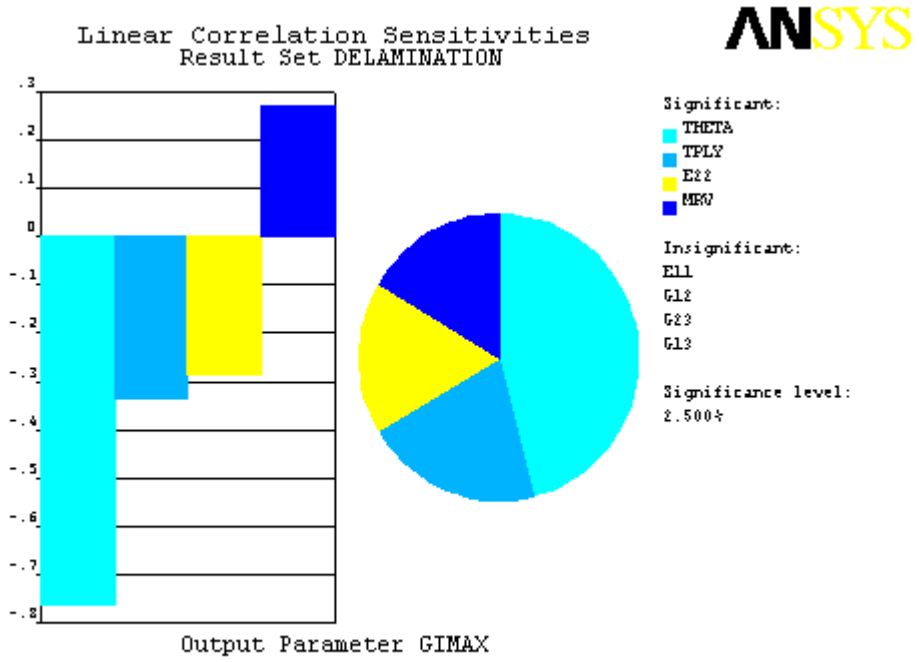

Figure 5.31 Sensitivity plot of GIMAX: [0/45/-45$_2$/d/45/0] double cantilever beam model

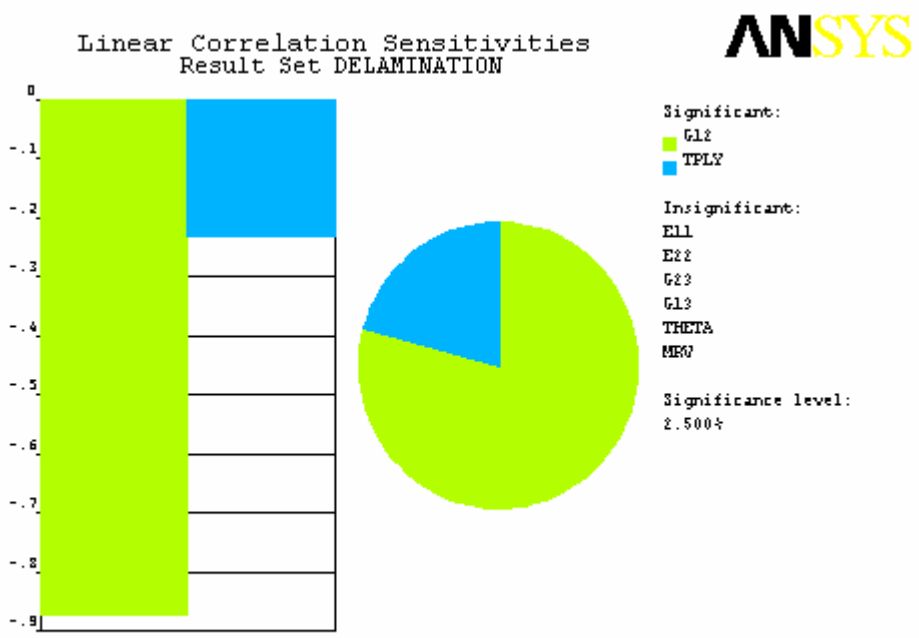

Figure 5.32 Sensitivity plot of GIIAVG: [0/45/-45$_2$/d/45/0] double cantilever beam model

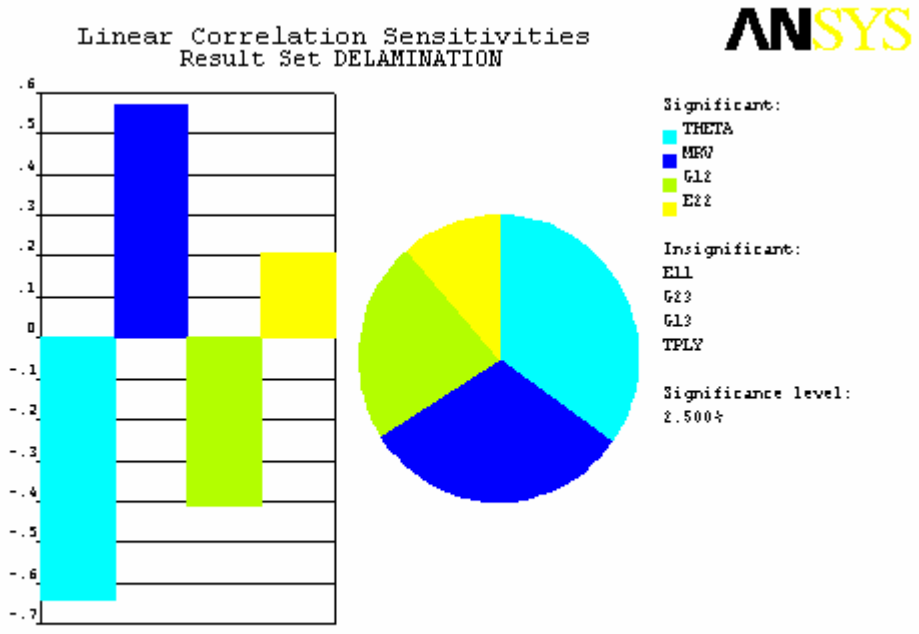

Figure 5.33 Sensitivity plot of GIIMAX: [0/45/-45$_2$/d/45/0] double cantilever beam model

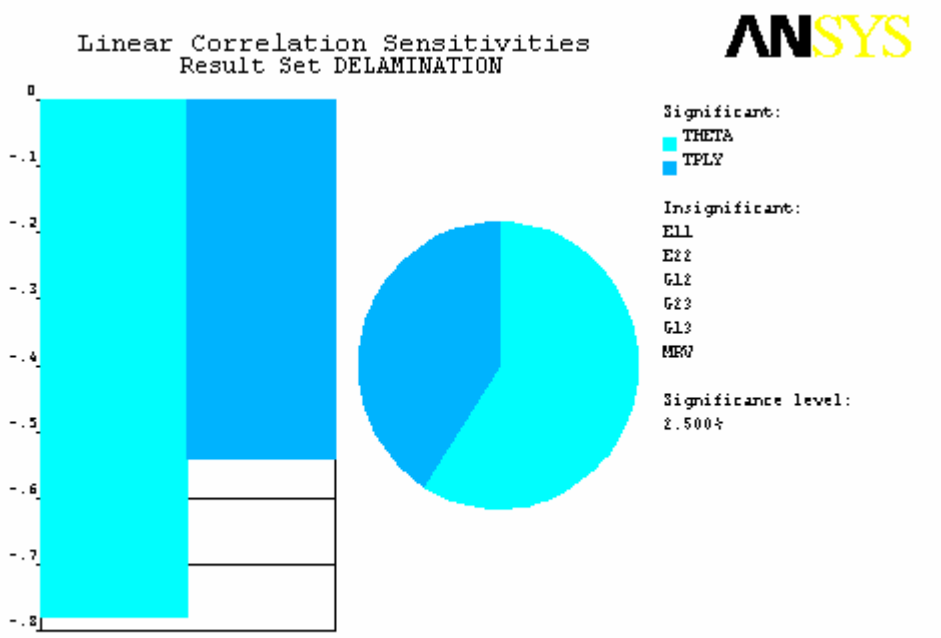

Figure 5.34 Sensitivity plot of GIIIMAX: [0/45/-45$_2$/d/45/0] double cantilever beam model

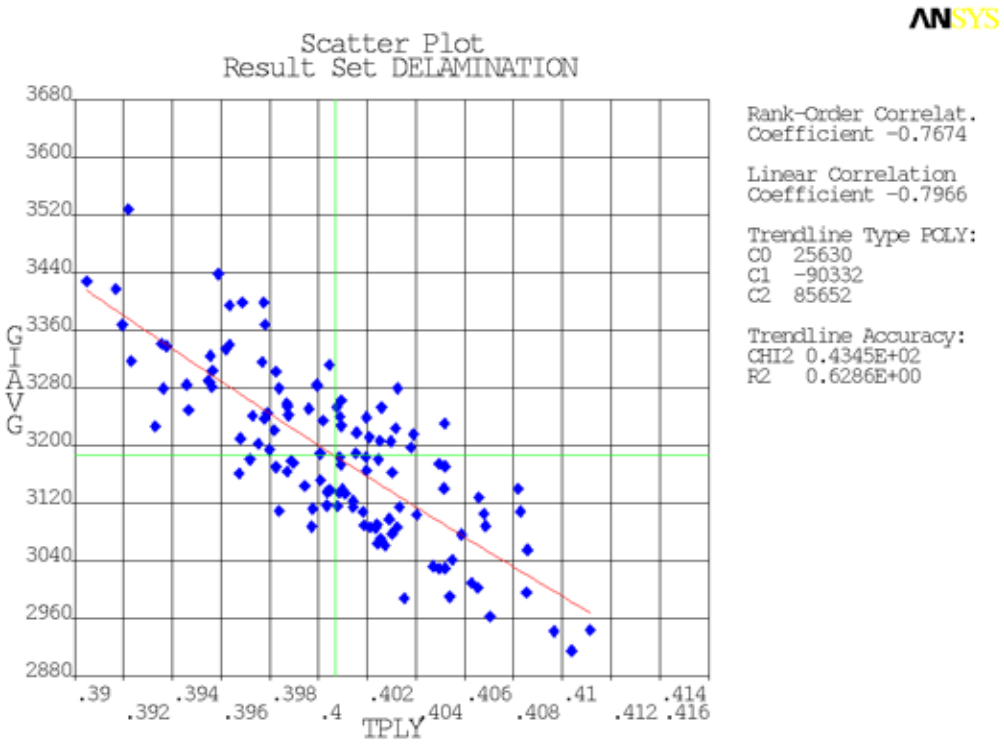

Figure 5.35 Scatter plot of GIAVG vs. ply thickness: [0/45/-45$_2$/d/45/0] double cantilever beam model

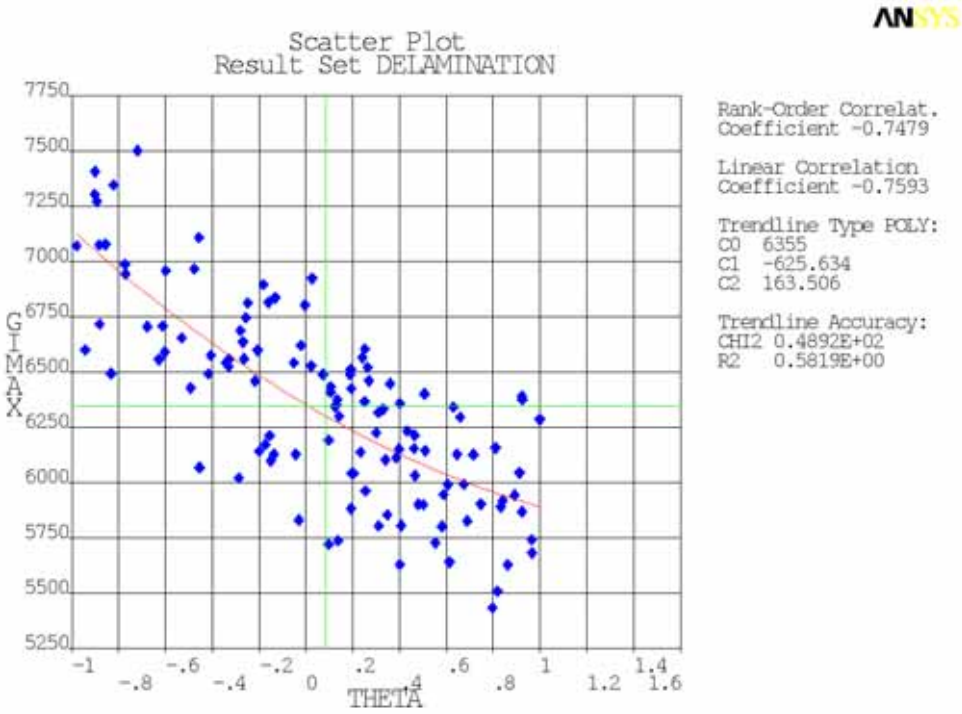

Figure 5.36 Scatter plot of GIMAX vs. fiber misalignment: [0/45/-45$_2$/d/45/0] double cantilever beam model

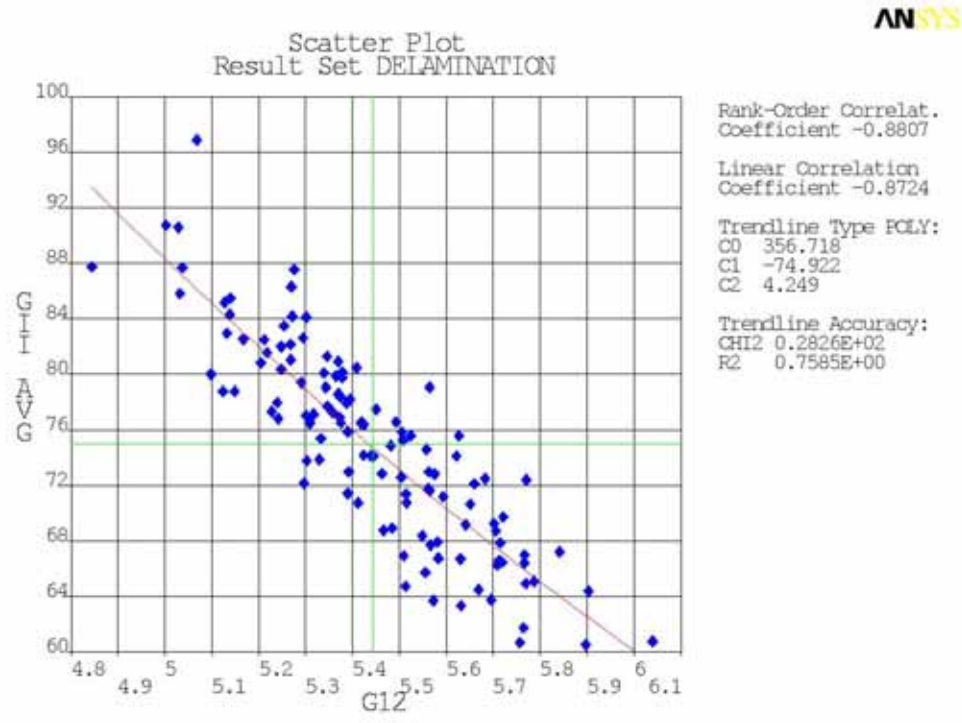

Figure 5.37 Scatter plot of GIIAVG vs. in-plane shear modulus: [0/45/-45$_2$/d/45/0] double cantilever beam model

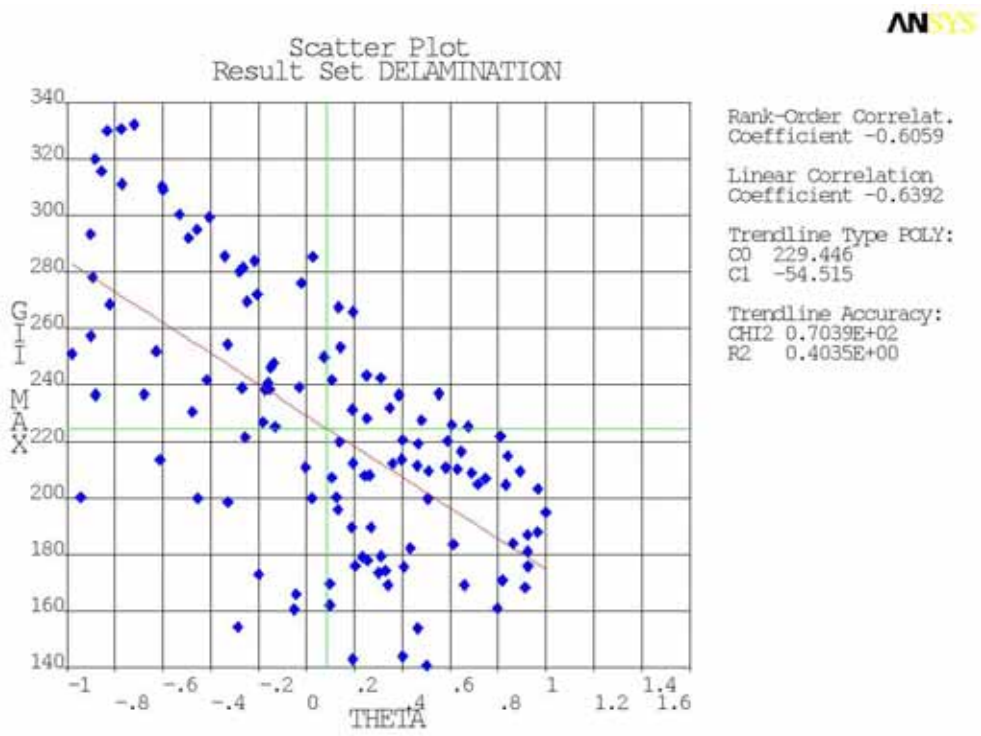

Figure 5.38 Scatter plot of GIIMAX vs. fiber misalignment: [0/45/-45$_2$/d/45/0] double cantilever beam model

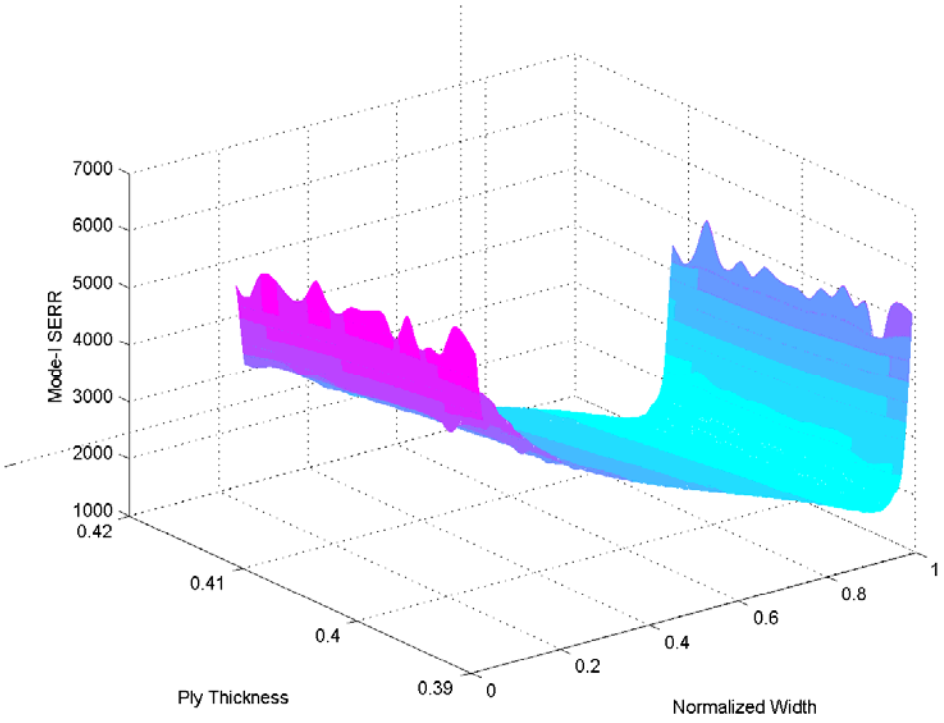

Figure 5.39 Three dimensional contour plot of Mode-I SERR distribution: [0/45/-45$_2$/d/45/0] double cantilever beam model

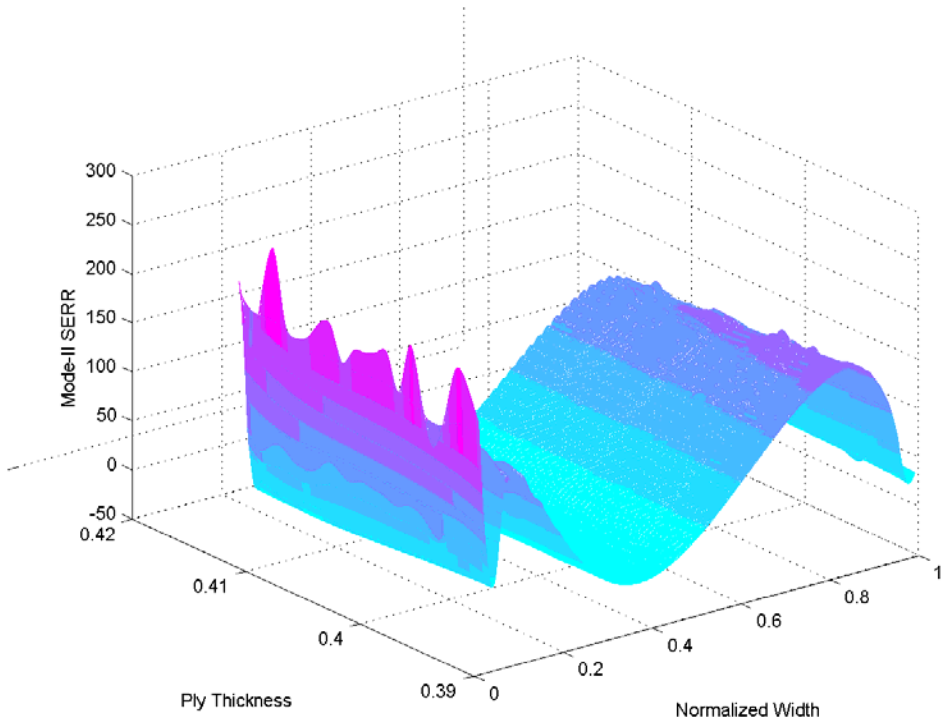

Figure 5.40 Three dimensional contour plot of Mode-II SERR distribution: [0/45/-45$_2$/d/45/0] double cantilever beam model

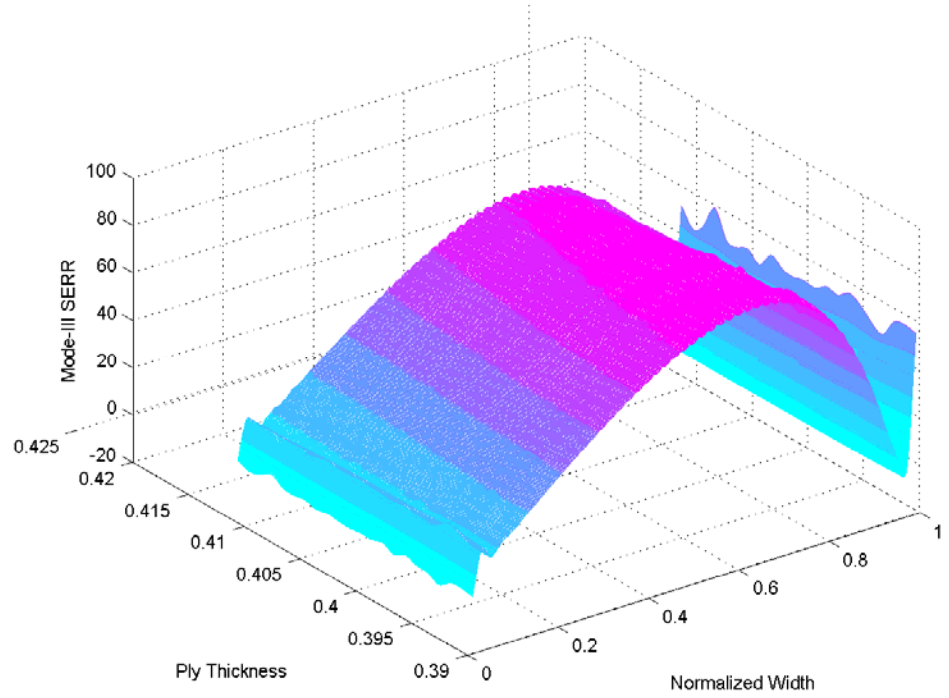

Figure 5.41 Three dimensional contour plot of Mode-III SERR distribution: [0/45/-45$_2$/d/45/0] double cantilever beam model

Table 5.11 Statistical characteristics of SERR values: [0/45/-45$_2$/d/45/0] double cantilever beam model

Variable	Distribution	Parameter 1	Parameter 2	*B*-Basis Value
GAVG (J/m^2)	Normal	3317.33	121.36	3134.8
GMAX (J/m^2)	Normal	6575.66	465.37	5875.73
GIAVG (J/m^2)	Normal	3187.16	115.88	3012.87
GIMAX (J/m^2)	Normal	6347.75	433.62	5695.55
GIIAVG (J/m^2)	Normal	75.00	7.17	64.21
GIIMAX (J/m^2)	Lognormal	219.2	1.22	162.98
GIIIMAX (J/m^2)	Normal	84.35	4.32	77.84

5.4 End-notched Flexure Models

End-notched flexure models of [90/-45/45/0]$_s$, [0/45$_3$/d/45/0] and [0/45/-45$_2$/d/45/0] laminates are analyzed with consideration for sliding friction between the delaminated surfaces. The laminate length, width, delamination length and ply thickness are kept constant at 100 mm, 25 mm, 25 mm and 0.4 mm respectively. Instead of a uniform load at the center of the laminate length, the nodes are selected and a constant displacement of 5 mm is applied.

First the [0/45$_3$/d/45/0] laminate is considered. The coefficient of friction between the delaminated surfaces is defined as a random input variable using a uniform distribution with a range of 0.0 to 0.8. The statistics of the random output parameters are given in Table 5.12. The sensitivity plots are not plotted since friction coefficient is the only random input variable. The scatter plots are shown in Figures 5.42-5.45. The contribution of energy lost due to friction to the total energy release rate increases with increase in friction and the contribution of the change in elastic strain energy decreases with increase in the friction coefficient. The total strain energy release rate is 84.66 J/m^2

when friction coefficient is 0.0 and is 117.2 J/m^2 when the friction coefficient is 0.8. The parameter ERATIO is the ratio of change in elastic strain energy to the energy loss due to friction. It can be seen from Figure 5.45 that ERATIO is 70.5 when there is frictionless contact between the surfaces and decreases to 1.85 when friction coefficient is 0.8. All the output parameters fit a Weibull distribution adequately. In Table 5.13, 'parameter 1' and 'parameter 2' represent the scale and shape parameters of the Weibull distribution respectively.

Table 5.12 Statistics of the random output parameters: [0/45$_3$/d/45/0] end-notched flexure model

Name	Mean	Standard Deviation	Minimum	Maximum
G (kJ/m^2)	0.1024	1.0316E-02	8.466E-02	0.1172
DELU (N-mm)	2.168	7.8506E-02	2.041	2.297
WFSUM (N-mm)	0.6057	0.3356	3.259E-02	1.102
DELPE (N-mm)	2.561	0.2579	2.117	2.931
ERATIO	8.603	15.40	1.852	70.48

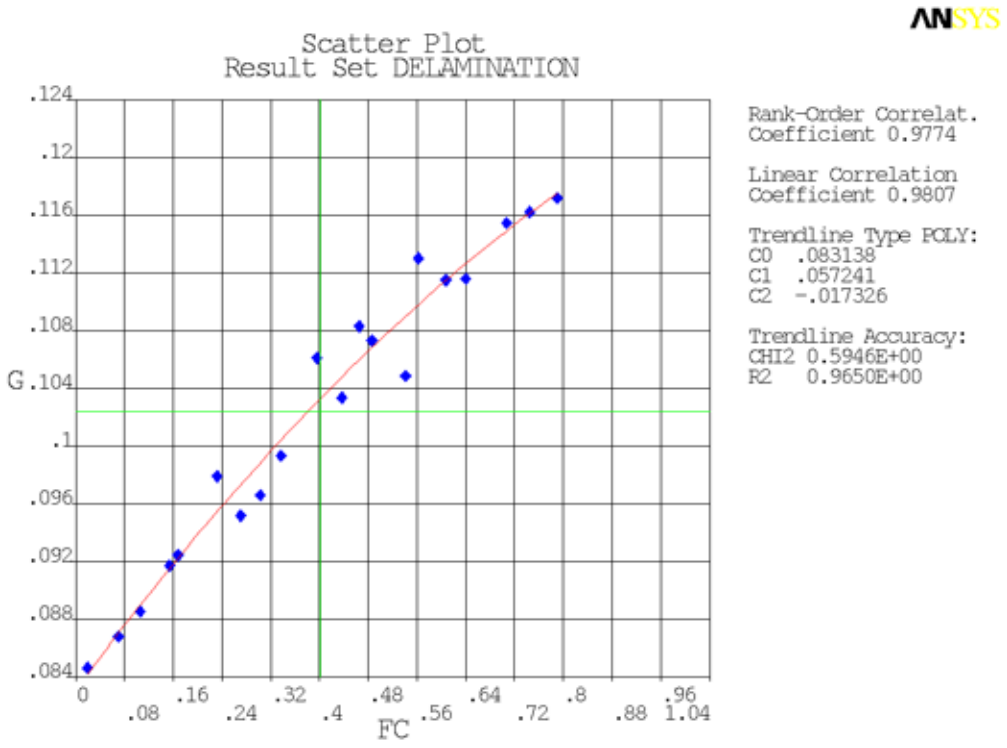

Figure 5.42 Scatter plot of G vs. friction coefficient: [0/45$_3$/d/45/0] end-notched flexure model

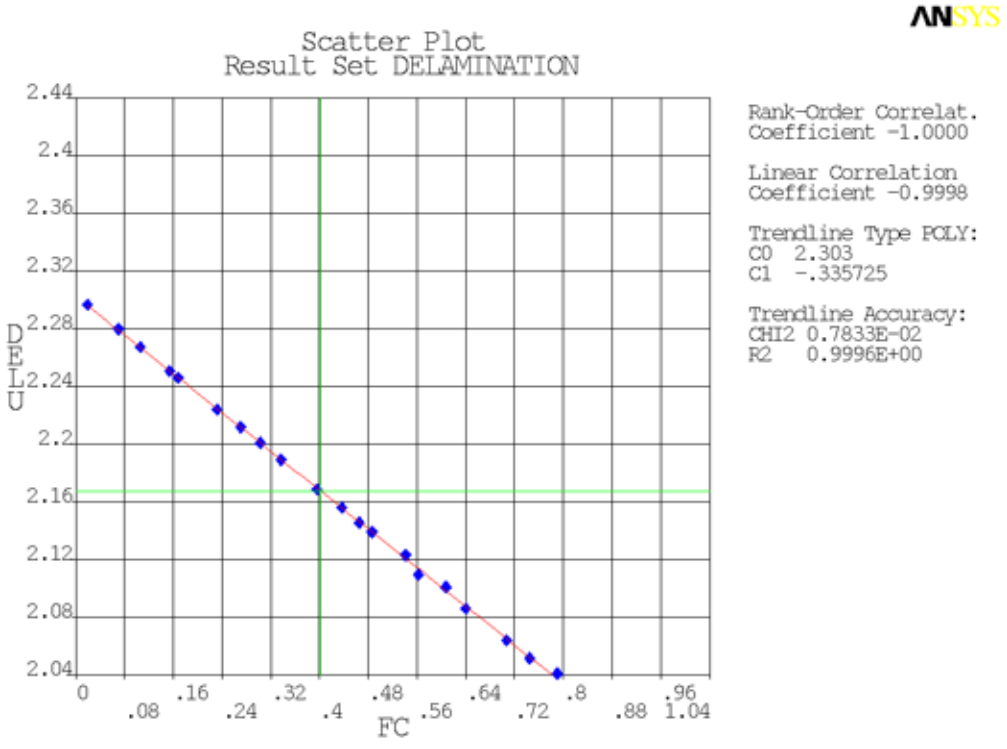

Figure 5.43 Scatter plot of DELU vs. friction coefficient: [0/45$_3$/d/45/0] end-notched flexure model

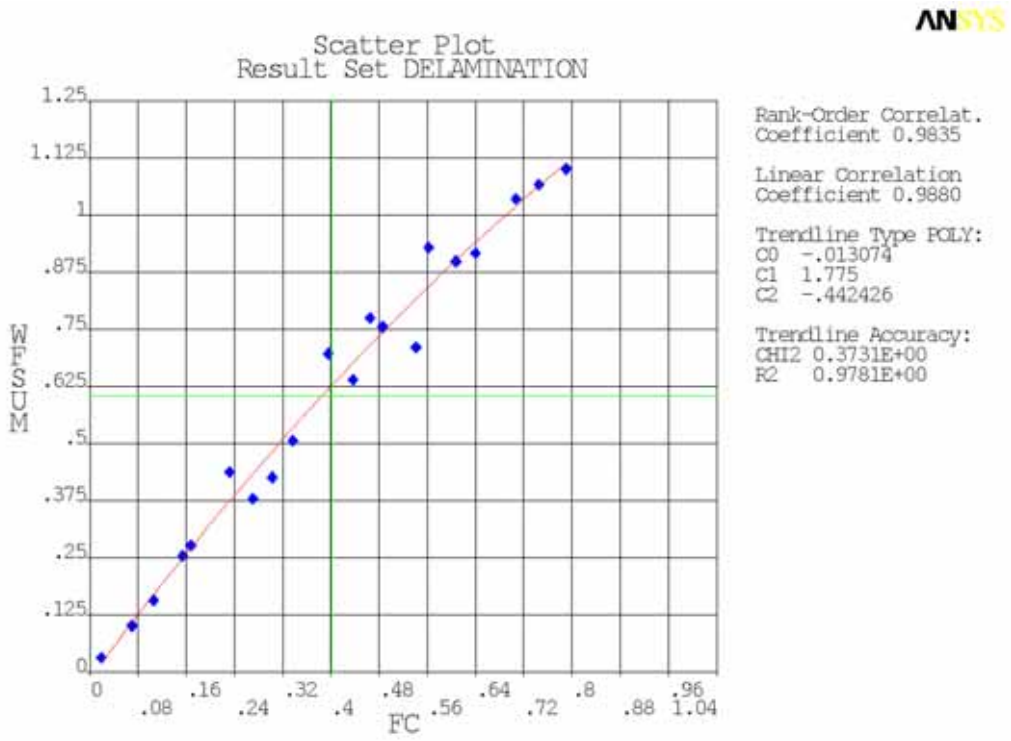

Figure 5.44 Scatter plot of WFSUM vs. friction coefficient: [0/45$_3$/d/45/0] end-notched flexure model

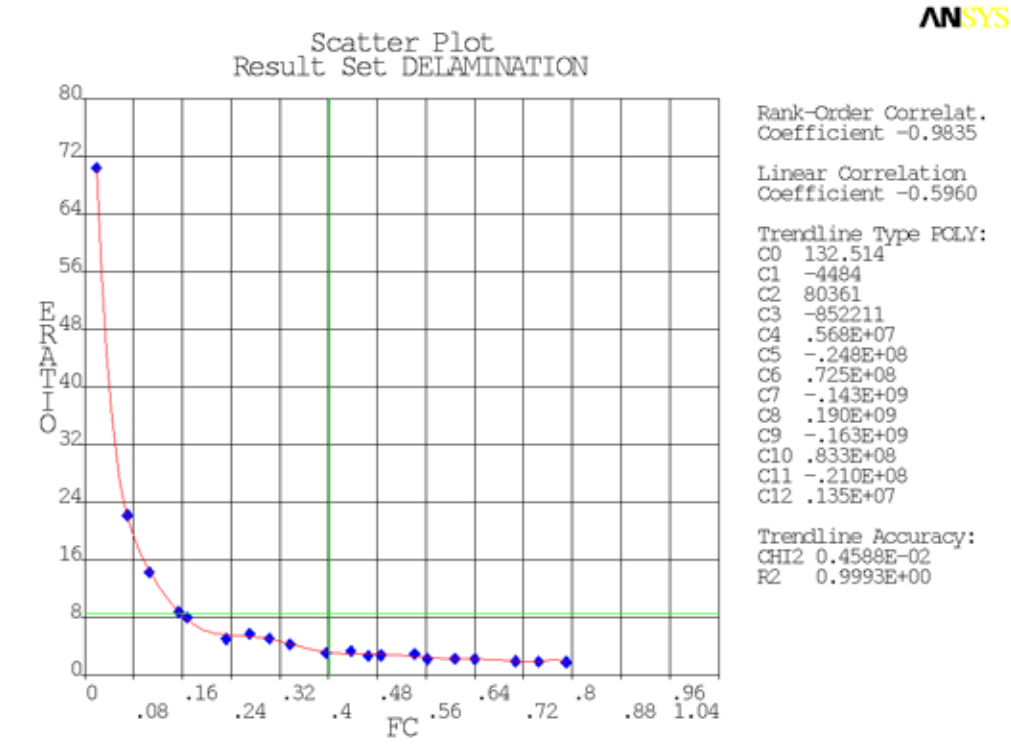

Figure 5.45 Scatter plot of ERATIO vs. friction coefficient: [0/45$_3$/d/45/0] end-notched flexure model

Table 5.13 Statistical characteristics of results: [0/45$_3$/d/45/0] end-notched flexure model

Variable	Distribution	Parameter 1	Parameter 2	*B*-Basis Value
G (kJ/m^2)	Weibull	0.10686	12.105	0.08021
DELPE (N-mm)	Weibull	2.67381	11.964	1.99998
DELU (N-mm)	Weibull	2.20525	31.132	1.97240
WFSUM (N-mm)	Weibull	0.67399	1.787	0.09647

The end-notched flexure test is repeated for the [0/45/-45$_2$/d/45/0] laminate with only the friction coefficient as the random input parameter. The statistics are listed in Table 5.14. The scatter plots are shown in Figures 5.46-5.49. For this case too, the same trends are observed. The total strain energy release rate is 54.53 J/m^2 when friction coefficient is 0.0 and is 86.02 J/m^2 when the friction coefficient is 0.72. It can be seen from Figure 5.49 that the ratio of change in elastic strain energy to the energy loss due to friction is 128.22 when there is frictionless contact between the surfaces and decreases to 1.63 when friction coefficient is 0.72. All the output parameters fit a Weibull distribution adequately. In Table 5.15, 'parameter 1' and 'parameter 2' represent the scale and shape parameters respectively.

Table 5.14 Statistics of the random output parameters: [0/45/-45$_2$/d/45/0] end-notched flexure model

Name	Mean	Standard Deviation	Minimum	Maximum
G (kJ/m^2)	6.8282E-02	9.0072E-03	5.4538E-02	8.6027E-02
DELU (N-mm)	1.503	3.0082E-02	1.453	1.551
WFSUM (N-mm)	0.4041	0.2546	1.2099E-02	0.8916
DELPE (N-mm)	1.707	0.2252	1.363	2.151
ERATIO	10.62	23.24	1.639	128.2

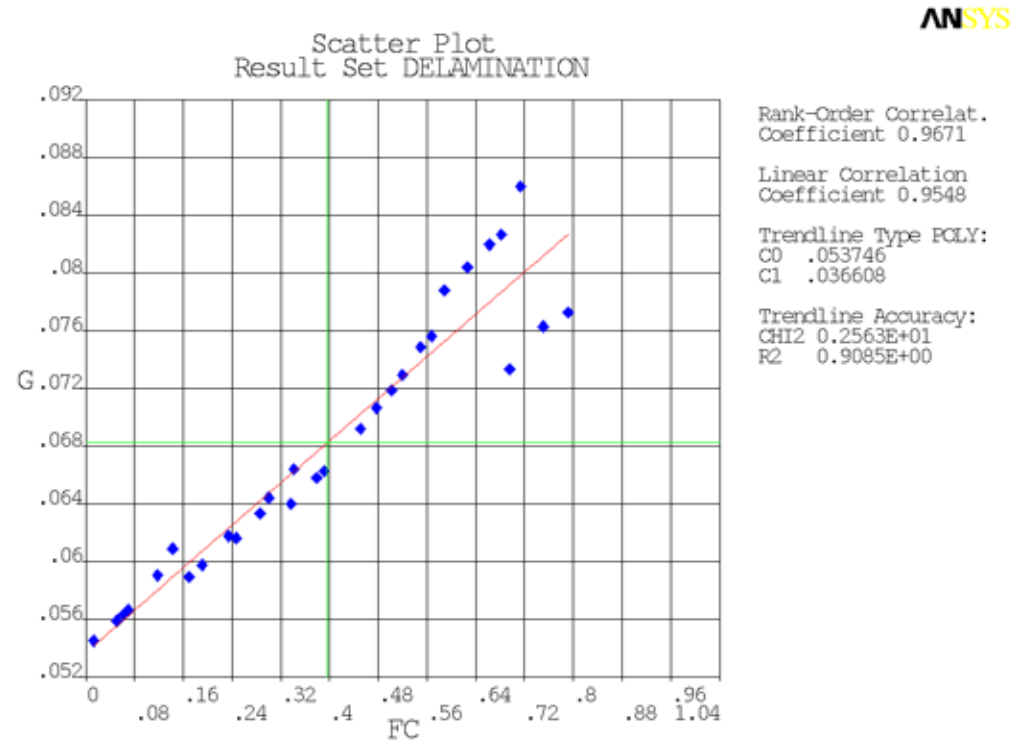

Figure 5.46 Scatter plot of G vs. friction coefficient: [0/45/-45$_2$/d/45/0] end-notched flexure model

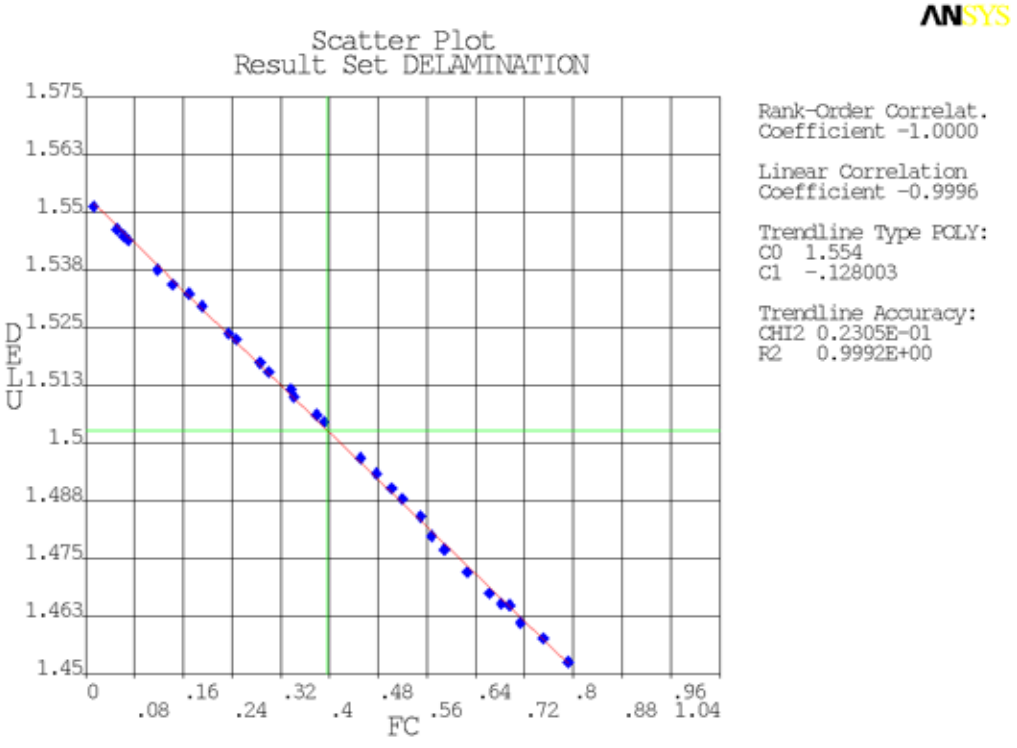

Figure 5.47 Scatter plot of DELU vs. friction coefficient: [0/45/-45$_2$/d/45/0] end-notched flexure model

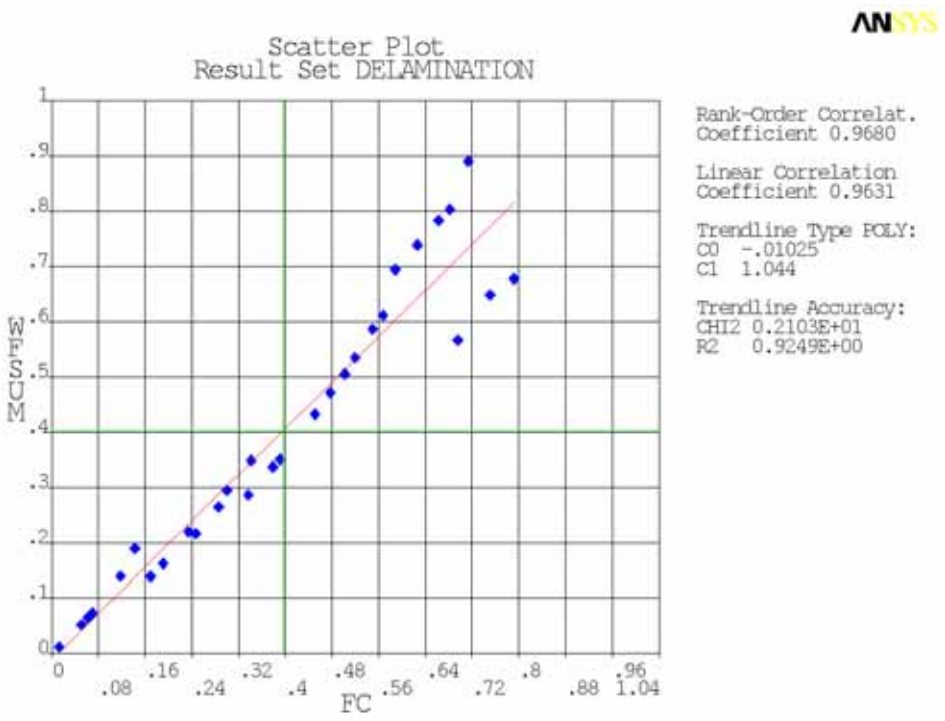

Figure 5.48 Scatter plot of WFSUM vs. friction coefficient: [0/45/-45$_2$/d/45/0] end-notched flexure model

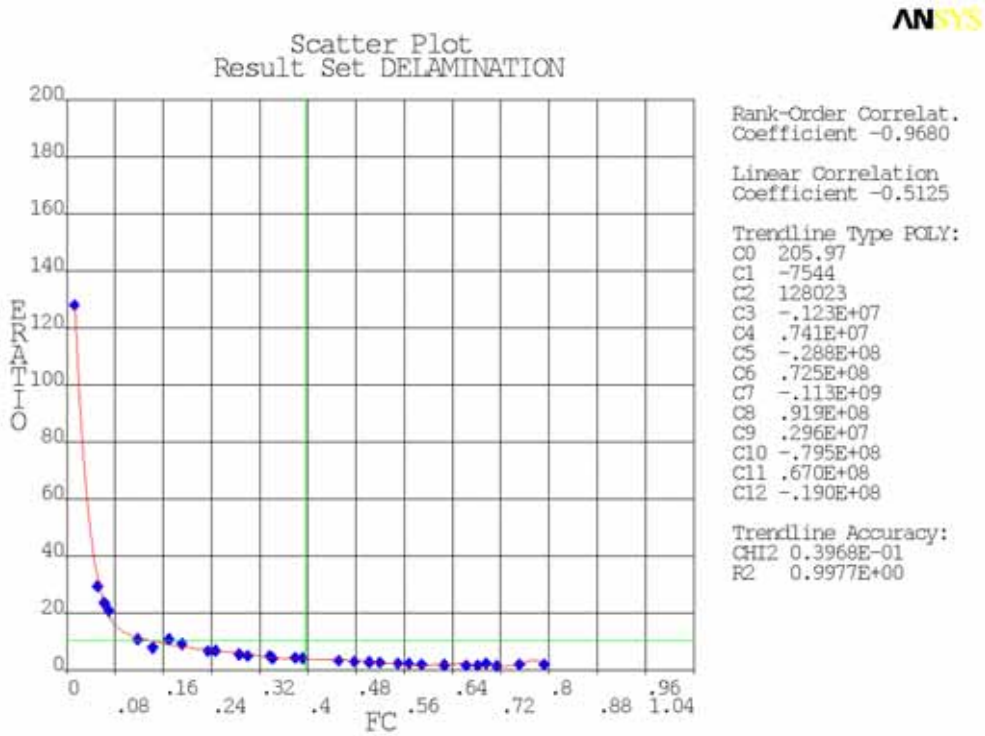

Figure 5.49 Scatter plot of ERATIO vs. friction coefficient: [0/45/-45$_2$/d/45/0] end-notched flexure model

Table 5.15 Statistical characteristics of results: [0/45/-45$_2$/d/45/0] end-notched flexure model

Variable	Distribution	Parameter 1	Parameter 2	*B*-Basis Value
G (kJ/m^2)	Weibull	0.07225	8.34929	0.04942
DELPE (N-mm)	Weibull	1.80583	8.33765	1.23467
DELU (N-mm)	Weibull	1.51657	57.85458	1.43570
WFSUM (N-mm)	Weibull	0.44544	1.53247	0.05628

The end-notched flexure model of the [90/-45/45/0]$_s$ laminate is analyzed next with all the material properties and friction coefficient as random input variables. In this case, the change in elastic strain energy is controlled by not only the friction coefficient but also by the longitudinal and transverse moduli. This is verified from the deviation of the sample points from the trendline fitted for DELU versus friction coefficient. The energy loss due to friction is not influenced by the scatter in the material property data and is a linear function of the friction coefficient. This is because only the contact stiffness for the first iteration of every simulation loop depends on the material properties and for subsequent iterations; the contact stiffness is automatically updated to reflect the changes in contact status by ANSYS software. Therefore, small changes in material properties do not affect the contact element's output. Except for the friction energy dissipation, which fit a normal distribution, all other parameters fit a Weibull distribution.

Table 5.16 Statistics of the random output parameters: $[90/-45/45/0]_s$ end-notched flexure model

Name	Mean	Standard Deviation	Minimum	Maximum
G ($x10^3$ kJ/m^2)	3.4089E-04	5.4832E-05	2.4125E-04	4.3046E-04
DELU (N-m)	6.4789E-03	1.7401E-04	6.1621E-03	6.9343E-03
WFSUM (N-m)	2.7184E-03	1.5293E-03	4.9516E-05	5.2292E-03
DELPE (N-m)	8.5222E-03	1.3708E-03	6.0313E-03	1.0762E-02
ERATIO	6.903	18.11	1.186	134.5

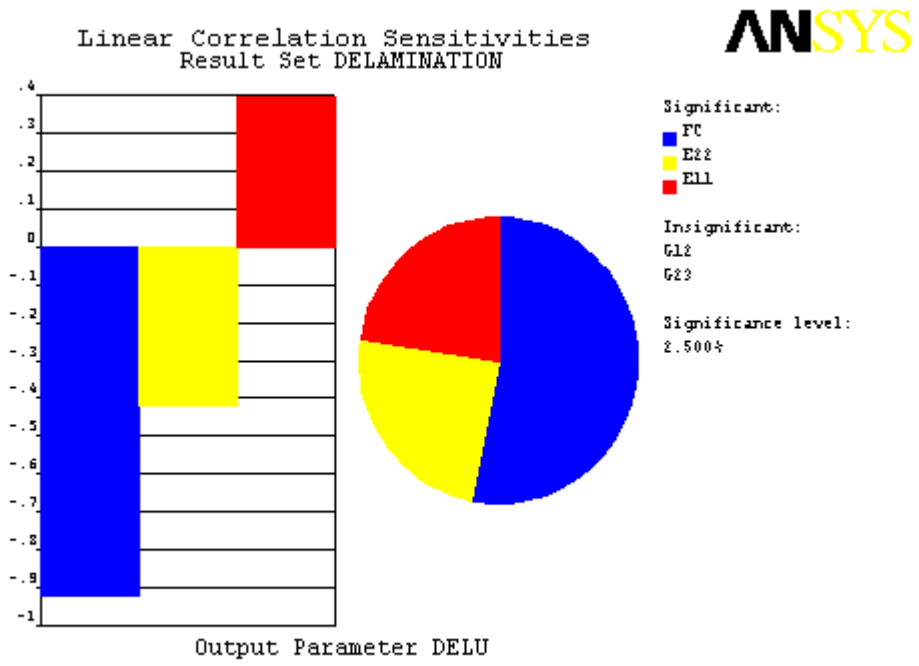

Figure 5.50 Sensitivity plot of DELU: $[90/-45/45/0]_s$ end-notched flexure model

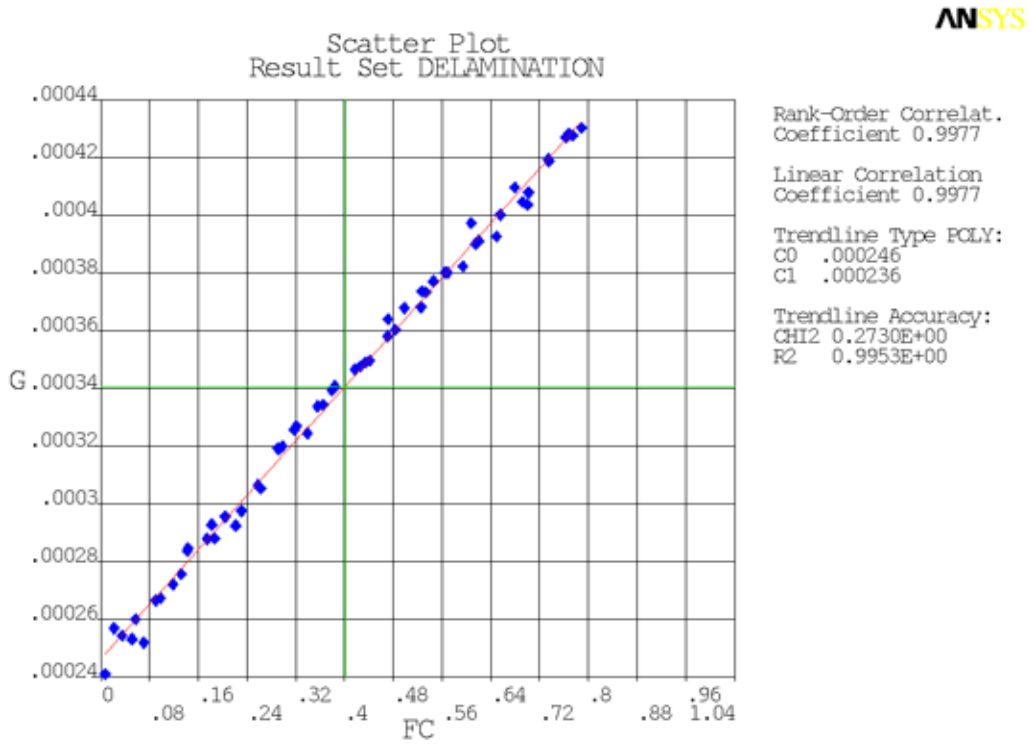

Figure 5.51 Scatter plot of G vs. friction coefficient: $[90/-45/45/0]_s$ end-notched flexure model

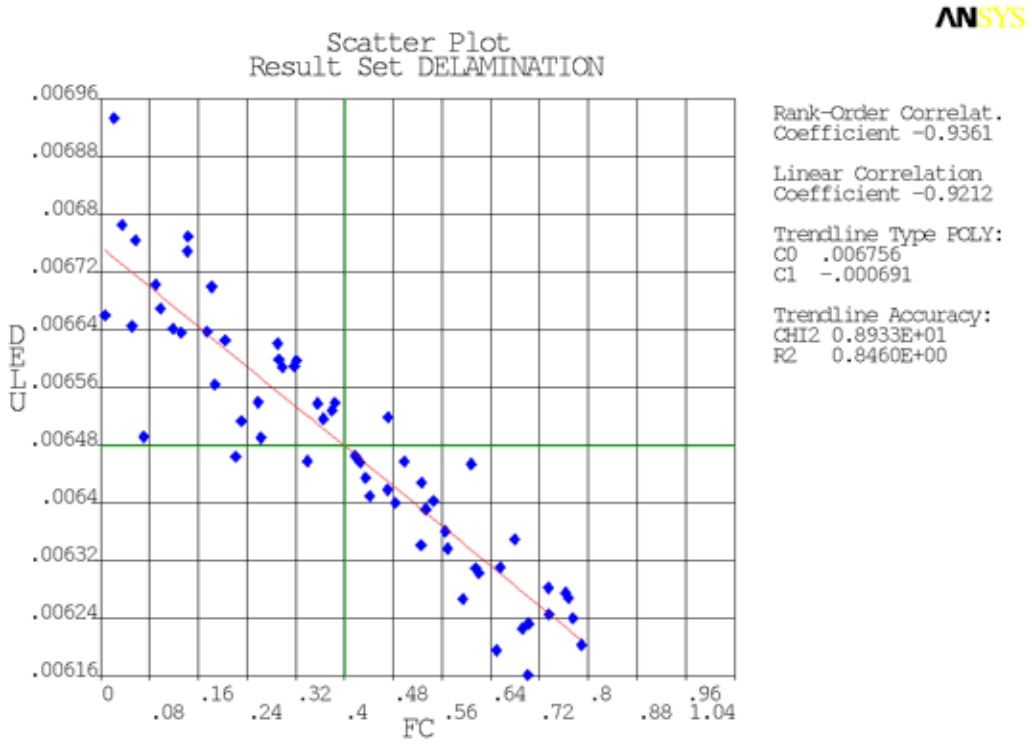

Figure 5.52 Scatter plot of DELU vs. friction coefficient: $[90/-45/45/0]_s$ end-notched flexure model

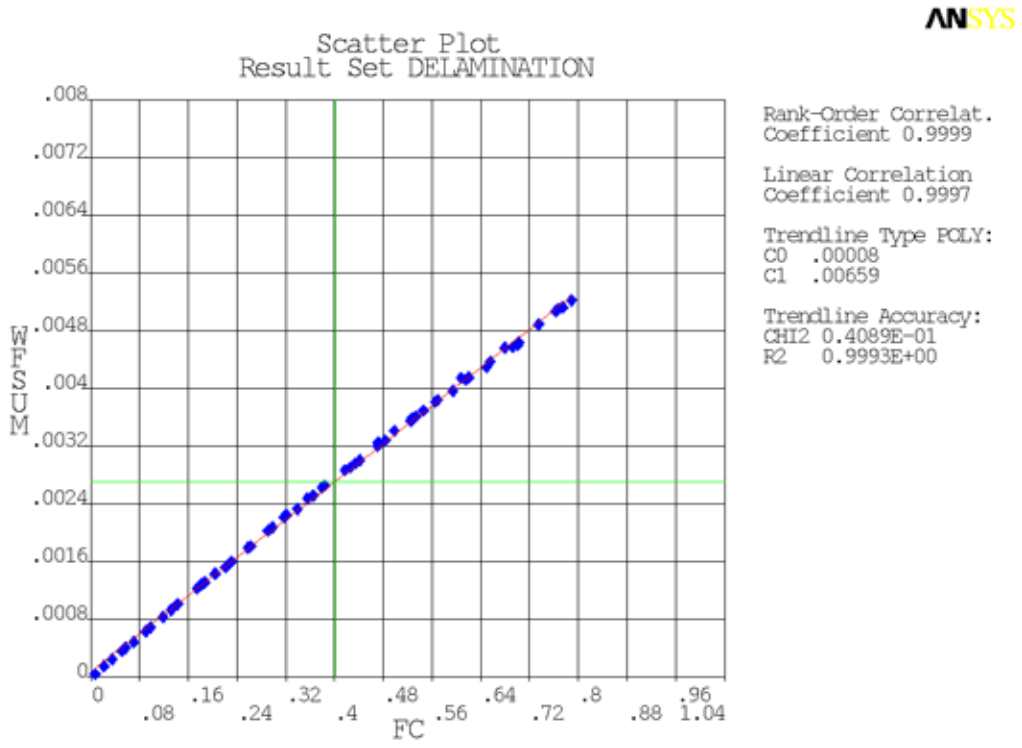

Figure 5.53 Scatter plot of WFSUM vs. friction coefficient: $[90/-45/45/0]_s$ end-notched flexure model

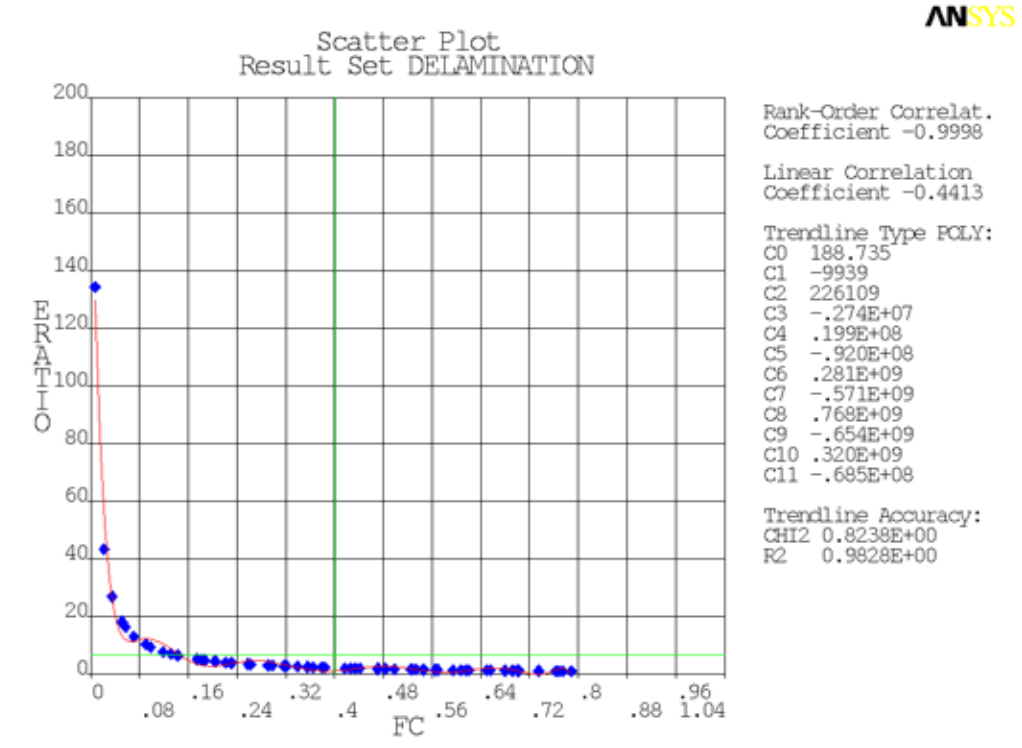

Figure 5.54 Scatter plot of ERATIO vs. friction coefficient: $[90/-45/45/0]_s$ end-notched flexure model

Table 5.17 Statistical characteristics of results: $[90/-45/45/0]_s$ end-notched flexure model

Variable	Distribution	Parameter 1	Parameter 2	*B*-Basis Value
G ($x10^3$ kJ/m^2)	Weibull	3.64077e-04	7.23825	2.458e-04
DELPE (N-m)	Weibull	0.00910	7.22347	0.00614
DELU (N-m)	Weibull	0.00656	37.97388	0.00609
WFSUM (N-m)	Normal	0.00271	0.00152	2.577e-04

For all the three end-notched flexure models considered, the coefficient of friction between the delaminated surfaces is varied between 0.0 and 0.8 so that the strain energy release rate values for any value of friction coefficient can be evaluated from these results. For the graphite/epoxy composite considered in this study, it has been shown that the friction coefficient between the delaminated surfaces varies from 0.35 to 0.40. Table 5.18 lists the total strain energy release rate, change in elastic strain energy and energy loss due to friction for the three laminate configurations for friction coefficients 0.35 and 0.40.

Table 5.18 Inference from results: End-notched flexure model

Laminate	Parameter	FC = 0.35	FC = 0.40
$[0/45_3/d/45/0]$	G (J/m^2)	101	103.3
	DELU (N-mm)	2.1855	2.1687
	WFSUM (N-mm)	0.5540	0.6261
$[0/45/-45_2/d/45/0]$	G (J/m^2)	66.6	68.4
	DELU (N-mm)	1.5092	1.5028
	WFSUM (N-mm)	0.3552	0.4074
$[90/-45/45/0]_s$	G (J/m^2)	328.6	340.4
	DELU (N-m)	0.00651	0.00647
	WFSUM (N-m)	0.0024	0.0027

5.5 Unidirectional Double Cantilever Beam Model

Since Monte Carlo simulations cannot be performed for each and every configuration of a double cantilever beam model, the best option would be to perform a regression analysis for building a response surface model to obtain approximate analytical solutions for energy release rates that include all the typical uncertainties encountered. To validate the use of the response surface method in the ANSYS Probabilistic Design System for evaluating the statistically-based energy release rates, a unidirectional double cantilever beam model is analyzed. The settings are given in Table 5.19.

Table 5.19 Probabilistic analysis specifications: Unidirectional double cantilever beam model

Probabilistic analysis technique	Response Surface Method
Sampling method	Central Composite Design
Number of samples	149
Design of Experiments Levels: Lower Bound Probability	0.5%
Design of Experiments Levels: Upper Bound Probability	99.5%

The random input variable definitions are the same as that given in Table 5.2 and except for fiber misalignment (THETA) and friction coefficient (FC), all other random input variables are assigned for the current analysis. The parameters that are varied are given in Table 5.20.

Table 5.20 Parameter definitions: Unidirectional double cantilever beam model

Parameter	Minimum	Maximum
Laminate Width (LAMWID)	25 mm	40 mm
Delamination Length (DELAMLEN)	25 mm	50 mm
Opening Load (FZPDS)	25.5 N	51.0 N

After the analysis is completed, a regression analysis is performed to determine the response surface of the maximum and average mode-I strain energy release rates based on the results obtained at the sampling points. The output for the maximum strain energy release rate (GIMAX) is given in Figures 5.55 and 5.56. In Figure 5.55 the setting used for the regression analysis and the scaling of the input variables are listed. For the automatic Box-Cox transformation a step length of $\lambda = 0.001$ is used. Figure 5.56 lists the regression equation which is used to evaluate GIMAX in transformed form. Then the original value is calculated by back transforming the value using the equation provided.

```
Regression Analysis of Output Parameter GIMAX
=============================================


Requested settings for the Regression Analysis
----------------------------------------------
Response Surf Set Label= GIMAX
Solution Set Label     = DELAMINATION
Simulation Method      = Response Surface with CCD
Num. Fitted Samples    = 149
Regression Model       = Quadratic with crossterms
Results Transformation = Automatic Box-Cox Transformation
Filtering Input Terms  = Forward Stepwise Regression
Filtering Confidence   = 0.950000


Scaling of the Input Variables
------------------------------
E11_scaled      =  4.35275e+000*E11      -  6.39245e+002
E22_scaled      =  6.52913e+000*E22      -  6.93394e+001
G12_scaled      =  6.52913e+000*G12      -  3.55838e+001
G23_scaled      =  6.52913e+000*G23      -  2.60512e+001
G13_scaled      =  6.52913e+000*G13      -  3.55838e+001
TPLY_scaled     =  3.26457e+002*TPLY     -  1.30583e+002
MRV_scaled      =  6.17738e-001*MRV      -  5.86851e+000
LAMWID_scaled   =  4.53008e-001*LAMWID   -  1.47228e+001
DELAMLEN_scaled =  2.71805e-001*DELAMLEN -  1.01927e+001
FZPDS_scaled    =  2.66475e-001*FZPDS    -  1.01927e+001
```

Figure 5.55 Settings used for the regression analysis: Unidirectional double cantilever beam model

```
Regression Equation
-------------------

GIMAX_trans = Sum of ( Coefficient*Term )

Num. Regression Terms  = 17

                                          Value of  Stand. Dev.   Prob.
Term                                     Coefficient    of Coeff. Coef.=0
Constant                                6.38385e+000  9.6910e-004 <0.0001
E11_scaled                             -4.36806e-003  5.1566e-004 <0.0001
E22_scaled                              1.06056e-003  5.1566e-004  0.0417
TPLY_scaled                            -6.30289e-002  5.1566e-004 <0.0001
MRV_scaled                              2.09344e-003  5.1566e-004 <0.0001
LAMWID_scaled                          -3.83255e-001  5.1566e-004 <0.0001
DELAMLEN_scaled                         5.50182e-001  5.1566e-004 <0.0001
FZPDS_scaled                            5.41437e-001  5.1566e-004 <0.0001
LAMWID_scaled * LAMWID_scaled           2.19416e-002  4.2093e-004 <0.0001
DELAMLEN_scaled * DELAMLEN_scaled      -1.07332e-002  4.2093e-004 <0.0001
FZPDS_scaled * FZPDS_scaled            -1.23537e-002  4.2093e-004 <0.0001
TPLY_scaled * LAMWID_scaled             2.36388e-003  5.5938e-004 <0.0001
TPLY_scaled * DELAMLEN_scaled          -3.43330e-003  5.5938e-004 <0.0001
TPLY_scaled * FZPDS_scaled             -3.39587e-003  5.5938e-004 <0.0001
LAMWID_scaled * DELAMLEN_scaled        -2.30514e-002  5.5938e-004 <0.0001
LAMWID_scaled * FZPDS_scaled           -2.05360e-002  5.5938e-004 <0.0001
DELAMLEN_scaled * FZPDS_scaled          2.96155e-002  5.5938e-004 <0.0001


Back-Transformation of the output parameter
-------------------------------------------
GIMAX = (0.274000*GIMAX_trans+1.0)^(1/0.274000)
```

Figure 5.56 Regression equation for GIMAX: Unidirectional double cantilever beam model

From this equation more Monte Carlo simulations are also generated by choosing specific values for the parameters. The effects of uncertainties on the output for that particular configuration are then studied. The values chosen for the laminate width, delamination length and opening load are 25 mm, 25 mm and 51 N respectively. For this configuration of the double cantilever beam model, beam theory predicts a strain energy release rate of 51.89 J/m^2. A MATLAB program is written to run 240 Monte Carlo simulations for this specific laminate configuration by varying the random input variables to generate maximum and average strain energy release rate values. An Anderson-Darling goodness-of-fit test is performed to fit the results to appropriate distributions and the corresponding B-basis values are calculated. The results are listed in Table 5.21. It

can be seen that, in the present case, the beam theory predictions and *B*-basis value calculated for GIMAX are almost equal. But this may not be true for all cases, say, for delaminated composites in which the interactions between the random input variables and the random output parameters are pronounced.

Table 5.21 Statistical characteristics of results: Unidirectional double cantilever beam model

Variable	Distribution	Mean	Standard deviation	*B*-Basis Value
GIMAX (J/m^2)	Normal	54.56	1.76	52.03
GIAVG (J/m^2)	Normal	53.24	1.64	50.88

6 CONCLUSIONS AND RECOMMENDATIONS

6.1 Contributions

- A parametrical model of a laminated composite plate with through-the-width delamination is implemented using the two-sublaminate method and shell elements based on first-order shear deformation theory.
- A MATLAB code is written to calculate improved transverse shear stiffness values and the matrices used for evaluating improved transverse shear forces and strains, for a given laminate configuration and the corresponding material properties and to export the data to a text file in a format that can be imported by the ANSYS pre-processor.
- Layer interpenetration between the sub-laminate arms and sliding friction along the delamination surfaces is accounted for, by using surface-to-surface contact elements based on the augmented Lagrange method.
- A first-order shear deformation theory based improved plate closure technique is implemented using the ANSYS Parametric Design Language in the post-processing phase for the calculation of total energy release rates and its mode components at various locations along the delamination front.
- Double cantilever beam and end-notched flexure models of delaminated composite plates with various lay-ups, geometry and material properties are analyzed.
- Monte Carlo simulations are performed by considering material properties, mesh density, friction coefficient, virtual crack closure length, ply thickness, fiber orientation and shear correction factors as uncertainties.
- Effects of uncertainties on the mixed-mode strain energy release rates along the delamination front are studied using sensitivity plots, scatter plots and contour plots.
- An Anderson-Darling goodness-of-fit test is performed to fit the maximum and average strain energy release rates for each of the mode components to a Weibull, normal, or log-normal distribution and to calculate statistically-based properties.

- Regression analysis is performed to build the response surface for a unidirectional double cantilever beam model. Monte Carlo simulations are generated from the regression equation to study the effects of uncertainties on the maximum and average strain energy release rates for a particular configuration.

6.2 Conclusions

- Even if the scatter in the material properties, ply thickness, and fiber misalignment are within allowable tolerances, they have a significant influence on the evaluated strain energy release rate of delaminated composites.
- For symmetric laminates with mid-plane delaminations under opening load, small variations in fiber orientation do not affect the mode-I strain energy release rate distribution. The same is not true for laminates with offset delaminations, in which all three-mode components are controlled by the variations to some extent.
- Ply thickness is a significant factor for all the models analyzed even though the standard deviation is just 1% of the mean value. For a variation of 0.004 mm in the ply thickness value of 0.4 mm, the average SERR varies by 6 J/m^2, 18 J/m^2, and 80 J/m^2, respectively, for the $[90/-45/45/0]_s$, $[0/45_3/d/45/0]$, and [0/45/-45/-45/d/45/0] laminates.
- Sliding friction between the delaminated surfaces must be taken into account for accurate evaluation of mode-II strain energy release rates in end-notched flexure tests.
- As friction coefficient increases, the contribution of change in elastic strain energy to the total energy release rate ($\Delta U/\Delta A$) decreases and the contribution of energy loss due to sliding friction ($W^f / \Delta A$) increases.
- For a mean friction coefficient of 0.375 with a standard deviation of ±0.025, the total strain energy release rate varies from 101-103.3 J/m^2, 66.6-68.4 J/m^2, and 328.6-340.4 J/m^2 for the $[0/45_3/d/45/0]$, [0/45/-45/-45/d/45/0], and $[90/-45/45/0]_s$ laminates, respectively.
- Friction effects are negligible for unidirectional end-notched flexure specimens and occur only adjacent the supports.

- The results clearly indicate that probabilistic design is necessary to reliably predict delamination growth in laminated composites.
- Since Monte Carlo simulations cannot be performed for each and every configuration of a double cantilever beam or end-notched flexure specimen, the best option would be to use the response surface method and perform a regression analysis to obtain closed form solutions for energy release rates that include all the typical uncertainties encountered.

6.3 Recommendations

- Mode-II, mode-III and mixed-mode strain energy release rates of unidirectional composites can be characterized by performing regression analysis on end-notched flexure, split cantilever beam and mixed-mode bending models, respectively.
- Delamination growth can be simulated using adaptive meshing technique or using interface elements.
- Curved crack fronts can be studied.

REFERENCES

Barbero, E.J., "*Introduction to Composite Materials Design*," Taylor and Francis, Philadelphia, 1999.

Bruno, D. and Greco, F., "Mixed Mode Delamination in Plates: A Refined Approach," *International Journal of Solids and Structures*, Vol. 38, 2001, pp. 9149-9177.

Bruno, D., Greco, F. and Lonetti, P., "A Coupled Interface-multilayer Approach for Mixed Mode Delamination and Contact Analysis in Laminated Composites," *International Journal of Solids and Structures*, Vol. 40, 2003, pp. 7245–7268.

Bruno, D., Greco, F. and Lonetti, P., "Computation of Energy Release Rate and Mode Separation in Delaminated Composite Plates by Using Plate and Interface Variables," *Mechanics of Advanced Materials and Structures*, Vol. 12, 2005, pp. 285-304.

Buchholz, F.G., Rikards, R. and Wang, H., "Computational Analysis of Interlaminar Fracture of Laminated Composites," *International Journal of Fracture*, Vol. 86, 1997, pp. 37–57.

Chamis, C.C., Singhal, S.N. and Minnetyan, L., "Probabilistic Simulation of Progressive Fracture in Bolted-Joint Composite Laminates," NASA Technical Memorandum 107107, *35th Structures, Structural Dynamics and Materials Conference*, 1994.

Composite Materials Handbook, "Vol. 1 Polymer Matrix Composites: Guidelines for Characterization of Structural Materials," MIL-HDBK-17-1F, 2002.

Crews Jr., J. H., Shivakumar, K. N. and Raju, I. S., "Effect of Anticlastic Curvature on G Distribution for DCB specimens," *Proceedings of the 30th AIAA/ASME/ASCE/AHS Structures, Structural Dynamics and Materials Conference*, Mobile, AL, 1989, pp. 1242–1249.

Davidson, B.D., "Prediction of Energy Release Rate for Edge Delamination Using a Crack Tip Element Approach," *Composite Materials: Fatigue and Fracture - Fifth Volume*, ASTM STP 1230, R.H. Martin, ed., American Society for Testing and Materials, 1995, pp. 155-175.

Davidson, B.D., "Analytical Determination of Mixed-Mode Energy Release Rates for Delamination Using a Crack Tip Element," *Key Engineering Materials Volumes 121-122: Fracture of Composites*, E.A. Armanios, ed., Transtec Publications, Ltd., Switzerland, 1996, pp. 161-180.

Davidson, B.D., "A Predictive Methodology for Delamination Growth in Laminated Composites; Part I: Theoretical Development and Preliminary Experimental Results," DOT/FAA/AR-97/87, April 1998.

Davidson, B.D., "A Predictive Methodology for Delamination Growth in Laminated Composites; Part II: Analysis, Applications, and Accuracy Assessment," DOT/FAA/AR-01/56, October 2001.

Davidson, B.D., Hu, H., and Schapery, R.A., "An Analytical Crack Tip Element for Layered Elastic Structures," *Journal of Applied Mechanics*, Vol. 62, 1995, pp. 294-305.

Davidson, B.D. and Krafchak, T.M., "Analysis of Instability-Related Delamination Growth Using a Crack Tip Element," *AIAA Journal*, Vol. 31, No. 11, 1993, pp. 2130-2136.

Davidson, B.D. and Yu, L., "Energy Release Rate Prediction in Stiffened-skin Structure Using a Three-Dimensional Crack Tip Element Analysis," *Journal of Composite Materials*, Vol. 39, No. 20, 2005, pp. 1819-1842.

Davidson, B.D., Yu, L. and Hu, H., "Determination of Energy Release Rate and Mode Mix in Three-Dimensional Layered Structures Using Plate Theory," *International*

Journal of Fracture, Vol. 105, No. 1, 2000, pp. 81-104.

Dirikolu, M.H., Aktas, A. and Birgoren, B., "Statistical Analysis of Fracture Strength of Composite Materials Using Weibull Distribution," *Turkish Journal of Engineering and Environmental Science*, Vol. 26, 2002, pp. 45-48.

Kruger, R., "Three Dimensional Finite Element Analysis of Multidirectional Composite DCB, SLB and ENF Specimens," ISD-Report No. 94/2, Institute for Statics and Dynamics of Aerospace Structures, University of Stuttgart, 1994.

Krueger, R., "Virtual Crack Closure Technique: History, Approach, and Applications," *Applied Mechanics Reviews*, Vol. 57, No. 2, 2004, pp. 109-143.

Krueger, R. and O'Brien, T.K., "A SHELL/3D Modeling Technique for the Analysis of Delaminated Composite Laminates," *Composites Part A: Applied Science and Manufacturing*, Vol. 32, No. 1, 2001, pp. 25-44.

Kruger, R., Rinderknecht, S. and Konig, M., "Two- and Three-Dimensional Finite Element Analyses of Crack Fronts in a Multidirectional Composite ENF Specimen," ISD-Report No. 97/1, Institute for Statics and Dynamics of Aerospace Structures, University of Stuttgart, 1997.

Qiao, P. and Wang, J., "Mechanics and Fracture of Crack Tip Deformable Bi-material Interface," *International Journal of Solids and Structures*, Vol. 41, 2004, pp. 7423–7444.

Rolfes, R. and Rohwer, K., "Improved Transverse Shear Stresses in Composite Finite Elements Based on First Order Shear Deformation Theory," *International Journal for Numerical Methods in Engineering*, Vol. 40, 1997, pp. 51-60.

Rolfes, R., Noor, A.K. and Rohwer, K., "Effective Calculation of Transverse Stresses in Composite Plates," 2000.

Sankar, B.V. and V. Sonik, "Pointwise Energy Release Rate in Delaminated Plates," *AIAA Journal*, Vol. 33, No. 7, 1995, pp. 1312-1318.

Schapery, R.A. and Davidson, B.D., "Prediction of Energy Release Rate for Mixed-Mode Delamination Using Classical Plate Theory," *Applied Mechanics Reviews*, Vol. 43, No. 5, 1990, pp. S281-S287.

Sun, C.T. and Qian, W., "A Treatment of Interfacial Cracks in the Presence of Friction," *International Journal of Fracture*, Vol. 94, 1998, pp. 371–382.

Suo, Z. and Hutchinson, J.W., "Interface Crack between Two Elastic Layers," *International Journal of Fracture*, Vol. 43, 1990, pp. 1-18.

Suo, Z. and Hutchinson, J.W., "Mixed Mode Cracking in Layered Materials," *Advances in Applied Mechanics*, Vol. 29, 1992, pp. 63-191.

Szekrényes, A., "Delamination of Composite Specimens," Ph. D. dissertation, Department of Applied Mechanics, Budapest University of Technology and Economics, 2005.

Wang, J. and Qiao, P., "Interface Crack between Two Shear Deformable Elastic Layers," *Journal of the Mechanics and Physics of Solids*, Vol. 52, 2004a, pp. 891 – 905.

Wang, J. and Qiao, P., "On the Energy Release Rate and Mode Mix of Delaminated Shear Deformable Composite Plates," *International Journal of Solids and Structures*, Vol. 41, 2004b, pp. 2757–2779.

Whitcomb, J.D. and Shivakumar, K.N., "Strain-energy Release Rate Analysis of Plates with Post-buckled Delaminations," *Journal of Composite Materials*, Vol. 23, 1989, pp. 714–734.

Yu, L. and Davidson, B.D., "A Three-Dimensional Crack Tip Element for Energy Release Rate Determination in Layered Elastic Structures," *Journal of Composite Materials*, Vol. 35, No. 6, 2001, pp. 457-488.

Zou, Z., Reid, S.R., Li, S. and Soden, P.D., "General Expressions for Energy-Release Rates for Delamination in Composite Laminates," *Proc. R. Soc. Lon. A*, Vol. 458, 2002, pp. 645-667.

Zou, Z., Reid, S. R., Soden, P. D. and Li, S., "Mode Separation of Energy Release Rate for Delamination in Composite Laminates Using Sublaminates," *International Journal of Solids and Structures*, Vol. 38, 2001, pp. 2597–2613.

Zureick, A.H., Bennett, R.M. and Ellingwood, B.R., "Statistical Characterization of Fiber-Reinforced Polymer Composite Material Properties for Structural Design," *Journal of Structural Engineering*, Vol. 132, No. 8, 2006, pp. 1320-1327.

BIBLIOGRAPHY

ABAQUS theory manual version 6.5-1.

ANSYS Release 9.0 documentation.

De Morais, A.B., De Moura, M.F., Marques, A.T. and De Castro, P.T., "Mode-I Interlaminar Fracture of Carbon/Epoxy Cross-ply Composites," *Composites Science and Technology*, Vol. 62, 2002, pp. 679-686.

De Morais, A.B., Rebelo, C.C., De Castro P.M.S.T., Marques, A.T. and Davies, P., "Interlaminar Fracture Studies in Portugal: Past, Present and Future", *Fatigue & Fracture of Engineering Materials & Structures*, Vol. 27, 2004, pp. 767-773.

Flanagan, G., "A General Sublaminate Analysis Method for Determining Strain Energy Release Rates in Composites," *American Institute of Aeronautics and Astronautics*, 1994, pp. 381-389.

Harvey, S., "Connecting Parts - A study of Continuous Mesh versus Bonded Contact versus Constraint Equations," Collaborative Solutions Inc., ANSYS Tip of the Week, 2000.

Hwang, S.F. and Huang, C.C., "Sliding Mode Interlaminar Fracture Toughness of Interply Hybrid Composite Materials," *Polymer Composites*, Vol. 19, No. 5, 1998, pp. 514-526.

Hwang, S.F. and Hu, C-L, "Tearing Mode Interlaminar Fracture Toughness of Composite Materials," *Polymer Composites*, Vol. 22, No. 1, 2001.

Imaoka, S., "Sheldon's ANSYS Tips and Tricks: Understanding Lagrange Multipliers," 2001.

Imaoka, S., “Tips and Tricks: Preventing Rigid-Body Motion in Contact Problems,” 2001.

Imaoka, S., “ANSYS.NET Tips and Tricks: CERIG vs. RBE3, RIGID184,” 2002.

Kim, I.G., Kim, I.S., Nobuhide-Uda and Kim, J.Y., “A Study on Determining Mode Components of Strain Energy Release Rate of Free-Edge Delaminations in Composite Laminates,” *The International Journal of Advanced Manufacturing Technology*, Vol. 20, 2002, pp. 138-143.

Kovar, D. and Thouless, M., “Simple Method for Determining Frictional Sliding Resistance and Frictional Energy Dissipation in Layered Ceramics,” *Journal of the American Ceramic Society*, Vol. 80, No. 3, 1997, pp. 673-679.

Long, M.W. and Narciso, J.D., “Probabilistic Design Methodology for Composite Aircraft Structures,” Technical Report DOT/FAA/AR-99/2, 1999.

Martin, R.H., “Interlaminar Fracture Characterization: A Current Review”, NASA Contractor Report 187573, 1991.

MATLAB Version 6.5 Documentation.

Merzbacher, M., Adden, S. and Horst, P., “Efficient Computation of Energy Release Rates for Delaminated Beam Structures,” *Deutscher Luft- und Raumfahrtkongress*, 2005.

O’Brien, T.K., “Towards a Damage Tolerance Philosophy for Composite Materials and Structures,” *Composite Materials: Testing and Design (Ninth Volume)*, ASTM STP 1059, S.P. Garbo, ed., American Society for Testing and Materials, 1990, pp. 7-33.

Shan, B. and Pelegri, A.A., “Assessment of the Fracture Behavior of an Asymmetrically Loaded Cantilever Composite Structure,” *Journal of Engineering Materials and Technology*, Vol. 125, 2003, pp. 353-360.

Sheinman, I. and Kardomateas, G.A., "Energy Release Rate and Stress Intensity Factors for Delaminated Composite Laminates," *International Journal of Solids and Structures*, Vol. 34, No. 4, 1997, pp. 451-459.

Warrior, N.A., Pickett, A.K. and Lourenco, N.S.F., "Mixed-Mode Delamination – Experimental and Numerical Studies," *Strain*, Vol. 39, 2003, pp. 153-159.

Yang, X., Nanni, A. and Dharani, L., "Effect of Fiber Misalignment on FRP Laminates and Strengthened Concrete Beams," *9th Int. Conf., Structural Faults and Repair*, London, UK, 2001.

Yum, Y-J and You, H., "Pure Mode I, II and Mixed Mode Interlaminar Fracture of Graphite/Epoxy Composite Materials," *Journal of Reinforced Plastics and Composites*, Vol. 20, No. 9, 2001.